Debond Buckling of Woven E-Glass/Balsa Sandwich Composites Exposed to One-Sided Heating

Nathan M. Cholewa

Thesis submitted to the faculty of the Virginia Polytechnic Institute and State University in partial fulfillment of the requirements for the degree of

Master of Science

In

Engineering Mechanics

Scott W. Case

Brian Y. Lattimer

Raffaella De Vita

January 20, 2015

Blacksburg, VA

Keywords: Buckling, Sandwich Composite, Intermediate-Scale, High-Temperature, Debond, Interfacial Fracture

Debond Buckling of Woven E-Glass/Balsa Sandwich Composites

Exposed to One-Sided Heating

Nathan M. Cholewa

ABSTRACT

An experimental investigation was undertaken to analyze the behavior of sandwich composite structures exposed to one-sided heating where a debond exists between the unexposed facesheet and core material. Sandwich composites of plain weave E-glass/epoxy facesheets and an end-grain balsa wood core manufactured using the Vacuum Assisted Resin Transfer Molding (VARTM) technique were the only materials analyzed. These were selected due to their current use in naval vessels and the heightened interest in the fire response properties of balsa wood and its utility as a core material. In order to better understand the interfacial behavior, Mode I Double Cantilever Beam (DCB) fracture tests were performed at ambient, 60°C, and 80°C to determine the influence of the decreased Mode I fracture toughness. While ambient testing showed that stable crack growth could be obtained, high temperature tests resulted in considerable damage occurring to the core at the crack-front preventing stable crack growth. This can be attributed to the significant decrease in the balsa core strength and material properties even for small increases in temperature. Additionally, Mode II Cracked Split Beam (CSB) tests were performed at ambient temperature to examine the sliding dominant crack-growth. Again, the occurrence of balsa core damage prevented stable crack-growth and an accurate measurement of Mode II fracture toughness was not obtained.

Intermediate-scale compression testing with one-sided heating at two heat flux levels was performed with a custom designed load frame on sandwich composite columns. This enabled the influence of the debond to be measured using a 3D-Digital Image Correlation (DIC) technique spatially linked with a thermographic camera. The DIC allowed for a detailed observation of debond growth and buckling prior to global failure of the test article. A behavior similar to that observed in the Mode I DCB fracture tests occurred: as the interfacial temperature increased, the amount of crack growth decreased. This crack growth was followed by a core failure at the crack-

front, triggering a global failure of the test article. This global failure for test articles containing a debond manifested itself primarily as an anti-symmetric post-buckling shape. Test articles with no debond exhibited the typical progression of the out-of-plane displacement profile for a fixed-fixed column. As the out-of-plane displacement increased, core failure ultimately occurred near the gripped region where the zero-slope condition is required, triggering global failure of the no debond test article. These tests highlight that the reduction in strength and material properties of the end-grain balsa wood core significantly outweigh the reduction in interfacial fracture toughness due to the increased temperatures.

Dedication

Dedicated to my mother Olivia for supporting me throughout my academic career and, always providing the best advice when needed. Also, to the rest of my family for accepting the perpetual student status that has been my adult life and never doubting that I would eventually finish.

Acknowledgements

I would like to thank the following people who made the completion of this work possible.

My committee members: Dr. Scott Case, Dr. Brian Lattimer, and Dr. Raffaella De Vita for their continued support, patience, and advice.

The entire research group: especially Dr. Patrick Summers, Christian Rippe, Dr. Yanyun Chen, and rest of Norris 102 officemates for brainstorming sessions, lively discussions, and experimental setup help. Special thanks to Yanyun Chen for not hiding your cookies well enough to prevent me from discovering them during late night testing.

To Mac McCord and Danny Reed, for always having an answer to my strange and often complicated experimental setup questions.

Dave Simmons and Darrell Link for an endless supply of nuts, bolts, metal, conversation, and advice. Without the ESM Machine Shop, my time here would have been far more difficult.

Beverly Williams for all your assistance over the years and your well received reminders of when the holidays are near through the numerous gifts of candy you have given me.

Melissa Nipper and Paul Siburt for assistance in purchasing items for myself and in dealing with the many problems I encountered.

Christina Rosa Castaner for providing Dr. Case's schedule whenever I needed it and also the numerous bandages whenever I injured myself.

All photos by author.

Table of Contents

List of Figures

List of Tables

Chapter 1: Introduction

With the increasing need for new naval ships to replace an aging fleet, new materials are being examined to meet the novel requirements of a modern navy. Past military activity necessitated the use of massive destroyers and aircraft carriers to engage enemies from relatively long distances. Today, smaller ships are needed to both attack targets close to shore and safely transport personnel and equipment. Modern vessels must possess greater maneuverability and operate at higher speeds than in the past. One way of achieving this performance improvement is by incorporating lightweight materials within the ship structure where steel or other metals had previously been used. Possible candidate materials are sandwich composites comprising stiff outer facesheets bonded to a compliant, low-density central core material.

A basic diagram of a sandwich composite identifying the facesheets and core of the combined structure is shown in Figure 1. Facesheets can be made of nearly anything ranging from a purely isotropic material such as aluminum, to a fully orthotropic composite material, such as carbon-fiber-reinforced polymer (CFRP). Both facesheets may be composed of the same material. Alternatively, each facesheet may be different, a design which is often necessary if the outer surface of naval ships are to incorporate electromagnetic shielding into their structure. Core materials can be composed of various materials such as foams, both polymer and metallic based, honeycombs, or end-grain balsa wood.

Fig. 1. Side view of sandwich composite construction. Facesheets do not have to be composed of the same material or thickness.

The primary benefits of a sandwich construction lie in the ability to attain exceptionally high flexural stiffness-to-weight ratios. Vinson [1] showed that a flexural stiffness 300 times greater than the monocoque construction can be obtained with a honeycomb core and identical isotropic

face sheets if $t_f/h_c = 1/20$. This results in very low lateral deformations and contributes to a higher buckling load and natural frequency of the structure. These benefits are highly desirable on a vessel that is subjected to complicated loading from both the weight of the components onboard the ship along with wave/wind loading on the hull. An additional benefit includes the ability to tailor the sandwich composite structure to the specific operational needs of the ship such as the electromagnetic and infrared shielding required in the DDG-1000 Zumwalt class destroyer [2]. Manufacturing advantages are also attained by making single large sections of a structure using the Vacuum Assisted Resin Transfer Method (VARTM) instead of welding together plates of metal to form a single section. This limits the need for post-machining to mitigate the effects of the distortion due to welding. In fact, the DDG-1000 is breaking ground by manufacturing some of the largest panels ever assembled (30.5 x 18.3 m) using the VARTM technique with resin transfer times on the order of 12 hours or more [2]. While the benefits of a sandwich construction compared to a monocoque one are numerous, a more complicated material system may lead to unique and more complicated forms of damage.

Sandwich composite damage may take many forms, from damage occurring in either the facesheet or core materials separately, to damage from composite behavior. In the facesheet, delamination can occur between the plies making up the laminate or the facesheet can succumb to a compressive or tensile failure. Since the common assumption with sandwich composites is that facesheets carry the entire axial load, this failure is independent on what material is used as the core. Core failures may take the form of either localized core crushing or a shear failure since the core acts similarly to the web of an I-beam and carries the transverse shear stresses of the structure. Wrinkling of the facesheet may often occur where the facesheet and core are still bonded together but a local wave-like deformation is observed in the facesheet. Finally, facesheet/core interface debonding can often be the result of poor manufacturing, localized impact, or exposure to extremely high temperatures.

It is this last failure mechanism that is so crucial to vessel survivability. External forces may result in numerous areas of local impact damage which do not necessarily result in structure breach. If the structure is breached, damage to the inside of the vessel may cause explosions and sustained

fires of long duration. This combination of high temperatures with locally debonded regions may lead to a reduced buckling collapse load and ultimately total failure. For the DDG-1000, the US Navy assembled a team to investigate a multitude of material combinations to various load/environment conditions [2]. This resulted in approximately 6000 test articles over ten years with the conclusion that out of all the core materials investigated (foam, honeycomb, and balsa wood) the end-grain balsa wood was the best combination of mechanical properties along with the ability to contain the spread of a fire without producing toxic gases.

The selection of end-grain balsa wood as the primary core material for the DDG-1000 superstructure may seem like an unlikely choice when compared to the large number of foam and honeycomb cores available. Upon closer examination, it is the natural cellular structure of the wood itself that gives it the advantage. Often foam or other artificial cores will develop a char layer similar to charred PVC core (Figure 2) that can grow in size and release toxic gases. When balsa wood is exposed to high temperatures, the wood is able to develop a small char layer on the exposed side of the core. This charred layer has nearly negligible mechanical properties, but thermally it is of great benefit to the remaining undamaged core and facesheet. Because the char acts as an insulating layer, further damage to the core is limited and the unexposed facesheet temperature is significantly lower than the fire-exposed facesheet.

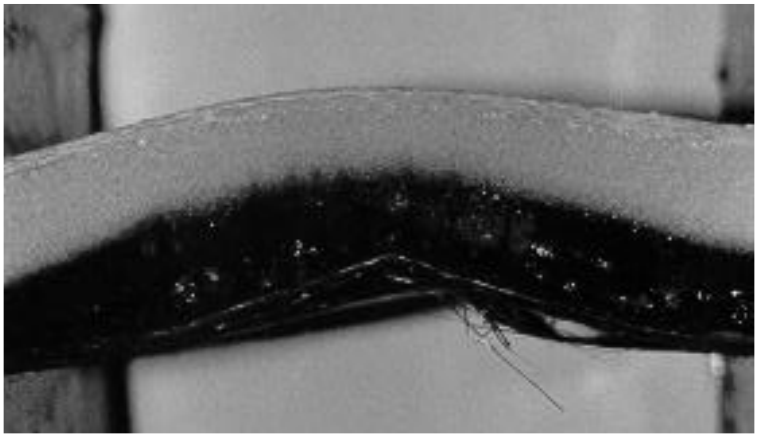

Fig. 2. Char layer in core during compression test performed by Mouritz *et al*. Mouritz, A.P., Gardiner, C., "Compression Properties of Fire-Damaged Polymer Sandwich Composites," *Compos. Part A Appl. Sci.*, vol. 33, 2002. Used with permission of Elsevier, 2014.

The buckling response of structures subjected to one-sided heating with localized debonding on the opposite side is complex because of two primary factors. First, the through-thickness temperature distribution may result in significantly reduced material properties on the fire exposed side of the sandwich composite, but due to the insulating balsa core the unexposed side may have minimal reduction in its properties. This transforms what was initially a symmetric sandwich composite into an asymmetric one. Secondly, the fracture toughness of the facesheet/core interface may be greatly reduced with increasing temperature, allowing what may be an initially small debonded region whose buckling load is greater than the critical load to grow into a larger debond until total failure of the structure occurs.

The focus of this work is to investigate the scenario of one-sided high-temperature exposure (simulating a fire condition) combined with a localized debond in a sandwich composite. A series of large-scale column tests (0.1 m x 0.75 m) were performed on a custom built load frame and heating system. A 3D Digital Image Correlation (DIC) system and a thermographic camera were used to measure spatially combined, full-field deformation and temperatures on the unexposed side. These measurements allow additional observational data on the growth of the debond region, if any, prior to buckling failure of the specimen. In addition to thermographic cameras recording facesheet surface temperatures, a second thermographic camera was used to observe exposed facesheet temperatures. To understand the role of the facesheet/core interface as the temperature is increased, Mode I and II fracture tests were attempted and fracture toughness and damage observations made.

Chapter 2: Literature Review

This literature review provides an overview of the work performed on sandwich composites with regards to Mode I (opening) and Mode II (sliding) fracture along with large-scale compressive testing. Various techniques have been used to characterize the interfacial fracture toughness of the facesheet/core interface. Along with a summary of small-scale fracture tests, large-scale testing was also reviewed with additional emphasis placed on any debond or high temperature experimental work. A summary of the more common sandwich composite fracture test techniques with additional detailed descriptions can be found in Carlsson and Kardomateas [3].

2.1 Sandwich Composite Fracture Testing

2.1.1 Mode I Fracture

Of the Mode I fracture techniques, the Double Cantliver Beam (DCB) specimen is the most common due to the overall simplicity of the test. The test requires only the bonding of piano hinges to the cracked end of the specimen; as a result, numerous researchers have used this technique to characterize the Mode I fracture toughness of facesheet/core interfaces. Prasad and Carlson [4] used the DCB test on sandwich composites with aluminum facesheets and both PVC and PMI cores. They showed that the core modulus has a substantial effect on whether crack kinking occurs and that adhesive type has a lesser influence. Shivakumar and Smith [4] used a slightly modified DCB specimen to investigate the fracture toughness of E-glass/epoxy facesheets with either a PVC or balsa core material. They modified the traditional DCB configuration by attaching a wire to the free end of the specimen in order to prevent overall rotation. For all PVC core samples, crack propagation did not occur on the interfacial plane but instead a small amount appeared in the core parallel to the facesheet/core interface. Later, Shivakumar [5] investigated several data reduction methods commonly used with the DCB test showing that the Modified Beam Theory (MBT) method produced results with the least amount of scatter. Girolamo *et al*. [6] investigated sandwich composites splice joints made with carbon/epoxy facesheets and an aluminum honeycomb core. Both Mode I and II along with a mixed-mode test were performed with Mode I utilizing the DCB method. Fracture toughness was calculated using a *J*-integral approach with crack length measured using a 3D-DIC system. Ramantani *et al*. [7] used an asymmetric DCB specimen with carbon/epoxy facesheets and Rohacell 71 core. A data reduction method based on beam theory

was used to incorporate the complex damage that can occur at the crack tip due to the bimaterial interface and obtain an accurate Mode I fracture toughness. Davidson *et al*. [8] modified the facesheet ply layup so that the upper and lower beams on either side of the crack had equivalent bending stiffness. This lessened the sample rotation observed in the asymmetric DCB test and led to a greater than 90% Mode I contribution to the fracture energy. All of the previously mentioned fracture tests were performed at room temperature. The work of Liechti and Marton [9] is the only fracture test to date and of any mode or test type to have been attempted at high temperatures. Using a DCB specimen with reinforcements on both facesheets, they obtained fracture toughness values for a sandwich composite with IM7/PETI-5 facesheets and a titanium honeycomb core. Only two temperatures were tested, 23°C and 180°C, with results showing that a slight decrease in the fracture toughness occurred at 180°C.

The Single Cantilever Beam (SCB) method is similar to the DCB test in that the upper beam has a piano hinge attached using an adhesive. The difference is that the lower beam is attached to a fixture to prevent any bending deformation in this half of the specimen. Cantwell and Davies [13,14] first used this technique to characterize the skin-core adhesion in a E-glass/epoxy facesheet with balsa core sandwich composite. Both Adams [12] and Weaver [13] investigated numerous Mode I test configurations and both concluded that the SCB configuration provided the most consistent results. However, since the bottom beam bending deformation is inhibited, the SCB test is truly a mixed-mode one that requires the use of the Virtual Crack Closure Technique (VCCT) to determine the individual energy release rate components. Variations of the SCB test have been made by Li and Carlson [14] and Viana and Carlsson [15] by allowing the fixture to rotate in order to better control the mode mixity.

2.1.2 Mixed-Mode Fracture

A modified DCB-Uneven Beam Moment (UBM) sandwich specimen was designed by Larsen *et al*. [16] to measure any mode-mixity fracture toughness value. By designing a test rig that allows a specified uneven bending moment (UBM) to be applied to each beam, any mode-mixity desired can be obtained. While having a single test setup that can do pure Mode I and II along with any ratio between the two is appealing in principle, the complexity and size of the fixture would make it practically impossible to contain within an oven for high temperature testing. Cantwell *et al*.

[17] used a mixed-mode Three-Point Bend Sandwich specimen (TPBS) to characterize the fracture toughness of an E-glass/epoxy balsa core sandwich composite. Using the Virtual Crack Closure Technique (VCCT) they were then able to determine the individual Mode I and II components of the energy release rate. Quispitupa *et al*. [18] used a Mixed-Mode Bending (MMB) fixture to test sandwich composites with DBLT-850 facesheets and PVC cores of various densities through a range of mode-mixities while again using the VCCT to determine the individual energy release rates.

2.1.3 Mode II Fracture

While there are numerous variants to test the Mode I fracture toughness, the same cannot be said for Mode II testing of the facesheet/core interface. The primary test is the Cracked Sandwich Beam (CSB) test first formulated by Carlsson [19] which requires nothing more than a three-point bend test fixture. This technique was modified slightly by Adams and Kessler [12] using a small wire to reduce frictional sliding of the two sides of the debond. Shipsha *et al*. [20] used a stiff insert to replace a part of the core just over the support on the debond side. This insert is used to transfer the shear load from the top facesheet to the lower one and once again, lessen the influence of the frictional sliding. To the author's knowledge, no high temperature CSB or any other Mode II tests have been attempted to date.

2.1.4 Large-Scale Testing

Large scale testing of sandwich composite columns with or without debonds have been performed by numerous investigators. Avery and Sankar [21] used a Nomex honeycomb core between plain weave carbon/epoxy facesheets to investigate the failure response when a width wise, centrally located debond was present. Specimen dimensions were 102 mm long and 50.8 mm wide with a single Teflon® strip used to form the debond. Because of the use of thin facesheets, no debond propagation was observed after the debond region locally buckled. La Saponara and Kardomateas [22] performed compression testing of sandwich columns consisting of 0.544 mm thick carbon/epoxy facesheets with a 12.7 mm Nomex honeycomb core and a single Teflon® sheet for the debond. Tests were conducted in displacement control and debond propagation was observed prior to global buckling of the sample. Vadakke and Carlsson [23] used 2 mm thick glass/vinyl ester facesheets bonded to a 50 mm thick PVC foam core. A single LVDT deflectometer was used to measure the out-of-plane displacement at the center of the debond region. Specimen length was

150 mm with a width of 37.5 mm and each end was fully clamped. Debond buckling and then propagation occurred until the debond extended all the way to the gripped area. High temperature testing of sandwich composites is limited and to date with limited work combining high temperature compressive loading with a one-sided heat exposure has been found. Mouritz and Gardiner [24] investigated the effect of fire-induced damage on edgewise compression of polymer sandwich composites with various core materials. Heat was applied using a cone calorimeter and compressive stiffness and strength were measured post-heating. Feih *et al*. [25] performed compression testing of sandwich composites with glass/vinyl ester facesheets and a balsa core. Heat was applied using a cone shaped heater and constant load levels applied with the goal of predicting the time-to-failure of the samples. Asaro *et al*. [26] and Lattimer et al. [27] tested large panel sandwich composites comprised of E-glass/vinylester facesheets and a balsa wood core subjected to a combined compressive and thermal loading in a custom designed load frame. While modest compressive loads were applied, these showed that the time and temperature dependence of the facesheet material with regards to property degradation mediate the failure response of the panel.

Chapter 3: Experimental Design

3.1 Introduction

A series of buckling tests were performed on samples exposed to one-sided heating to observe differences in the buckling response when debonds are present. These tests utilized a custom intermediate-scale load frame and heater panel assembly to obtain the desired load and temperature conditions. Prior to large scale testing, Mode I and II fracture testing was done to better understand the interfacial surface between the facesheet and core material. It was shown that significant core damage occurs preventing a pure interface crack from propagating. Because of the difficulty in obtaining high-temperature material property data, a micromechanics-based averaging approach was used taking advantage of prior experimental work to determine the nine orthotropic material constants.

3.2 Intermediate-Scale Load Frame

A custom load frame was designed and fabricated to perform tests on intermediate-scale test articles exposed to one-sided heating. The load frame is capable of providing a 355 kN tension/compression load at displacement rates ranging from 0.1 to 100 mm/min. Admissible sample sizes are 0.90 x 1.20 m for compression and 0.75 x 1.20 m in tension with custom grips designed for each test configuration. An overview of the primary components is shown in Figure 3 including the sliding heater panel assembly.

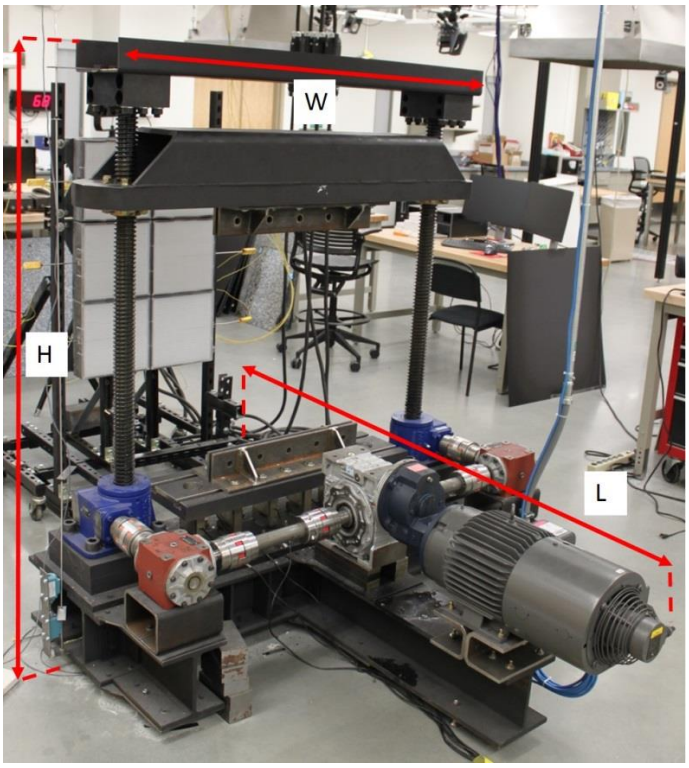

Fig. 3. Overview of custom load frame for intermediate scale test articles. Size is 1.83 x 1.64 x 1.65 m (H x W x L) with a total weight of 771 kgf. Heater panel assembly shown in the background.

The load frame base is constructed from two W8 x 48 I-beams between a 25.4 mm thick plate on top and a 6.35 mm plate on the bottom. Ribs were welded along each side of the individual I-beams in order to increase the stiffness of the base assembly and all parts of the load frame structure were machined from A36 steel (Figure 4). To allow for easy disassembly, if needed, grade 8 bolts were used throughout to attach all base parts to one another.

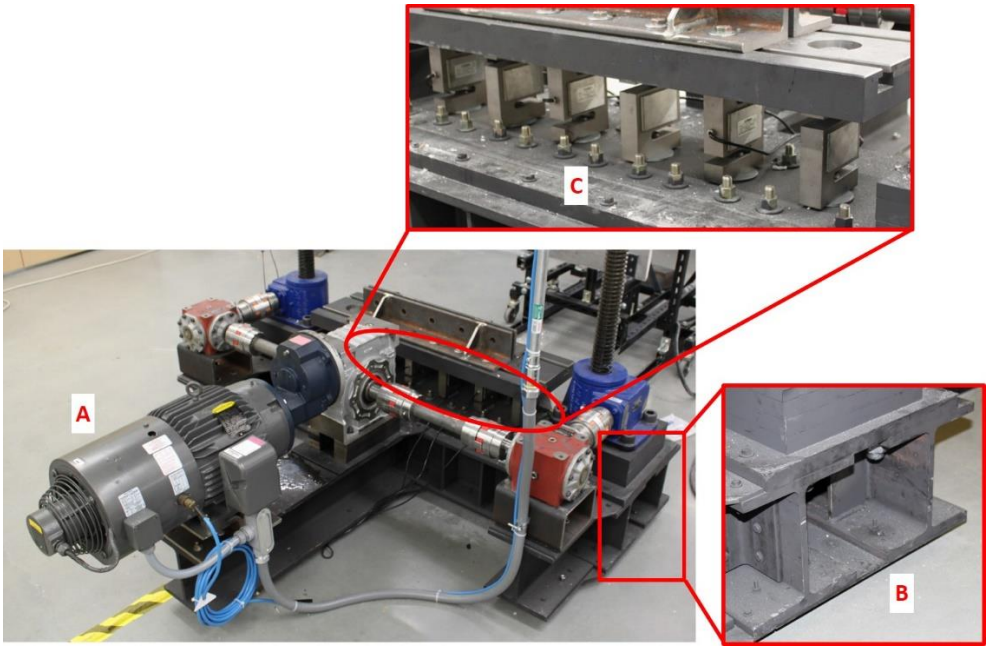

Fig. 4. Structural base of the custom intermediate scale load frame. (A) Baldor ZDM377OT motor, (B) two W8 x 48 A36 steel I beams with 25.4 and 6.35 mm upper and lower plates, (C) six Omega LCCA-15k load cells.

The upper crosshead was constructed from a 63.5 mm thick steel base with a machined 254 x 254 x 12.7 mm square tube welded to the upper side. This increases the bending stiffness to permit accurate measurements of the crosshead displacement at the sample surface contacting the grip. The crosshead assembly weighs 314 kgf and moves vertically along two 178 kN NOOK Industries screwjacks (20-MSJ-UR). The overall size of the frame is 1.83 x 1.64 x 1.65 m with a total weight of 771 kgf. The screwjack's motion was driven by a Baldor ZDM377OT motor connected to two 10:1 speed reducers that are then attached to two 1:1 miter gears (Figure 4). Control of the upper crosshead is via a custom LabView program routed through a Baldor VS1GV27-1B controller allowing for either load or displacement controlled tests. Loads are obtained from six Omega LCCA-15k load cells positioned below the lower crosshead and mounted to the 25.4 mm base plate. Each load cell has an operating range of 0 to 66.7 kN with an accuracy of 0.037% the full scale load.

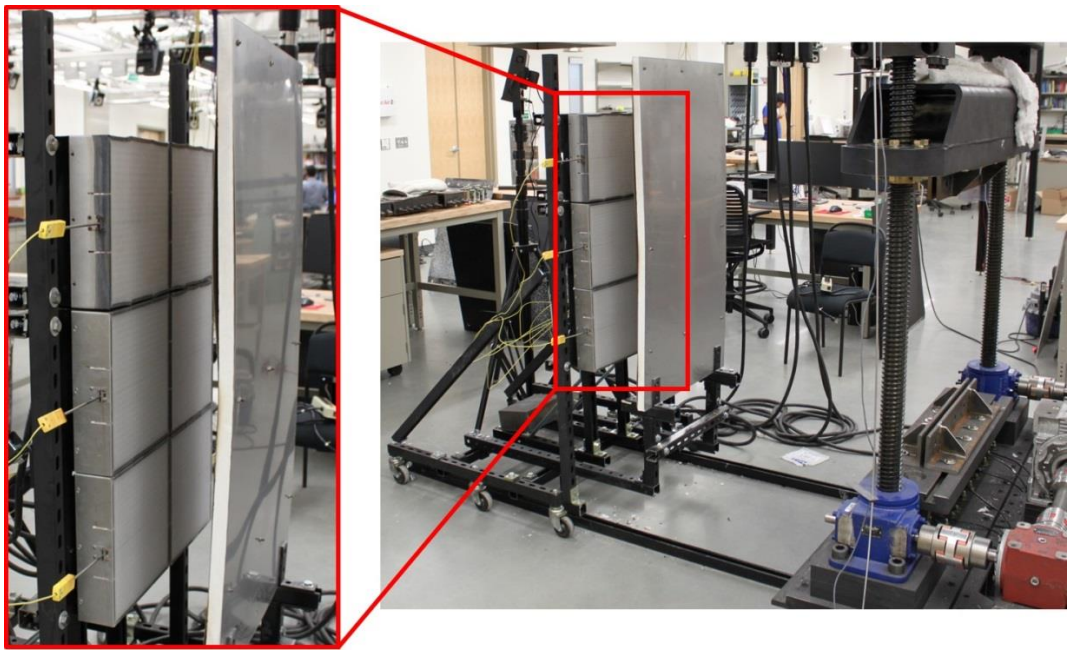

Fig. 5. Heater panel arrangement shown in 3 x 2 configuration. Fiberboard insulation shield used along with sliding tracks on ground to adjust the distance from sample surface for desired flux level.

Heat was applied by using a 3 x 2 configuration of quartz heater panels that can slide in the normal direction to the sample face as shown in Figure 5. The system is comprised of six Omega Quartz QH series square (300 x 300 mm) panels each capable of generating 9.3 W/cm^2 with a peak operating temperature of 977°C [28]. The overall maximum flux on the sample surface is 65 kW/m^2. This flux was measured experimentally by placing a thin stainless steel sheet in the load frame coated with a high-emissivity paint (ϵ = 0.98) on both sides and recording the temperature field (Figure 6a) on the unexposed surface using a FLIR SC655 thermographic camera. From this temperature field the flux at each discrete point (Figure 6b) can be calculated. Additional details of this technique can be found in Rippe and Lattimer [29].

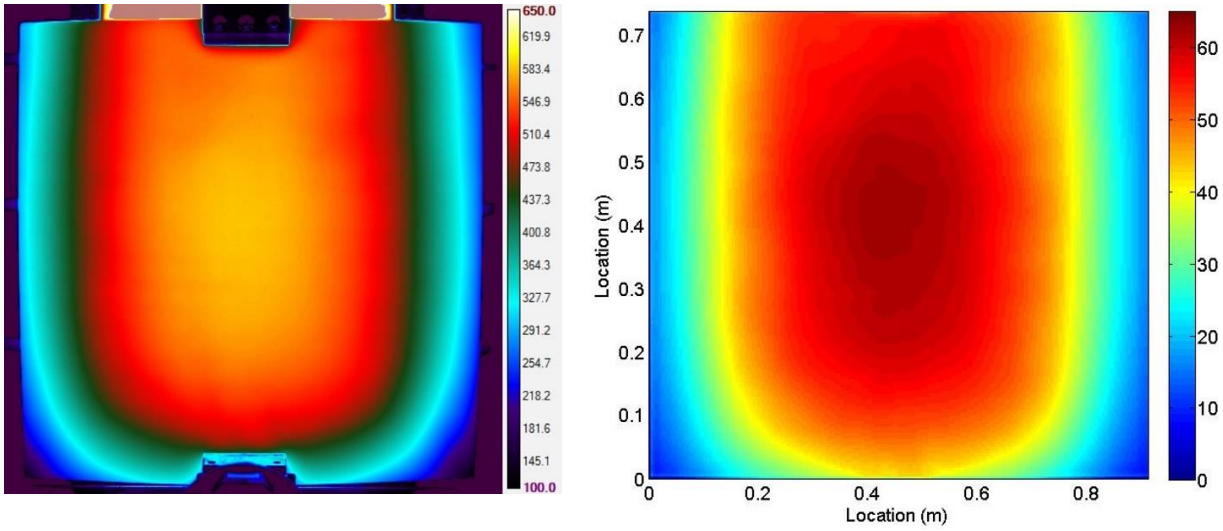

(a) (b)

Fig. 6. (a) Temperature profile obtained from thermographic camera, units in Celsius. (b) Corresponding maximum flux mapping on surface of plate from 2 x 3 heater panel arrangement, units in kW/m^2.

Each quartz-faced heater panel has an Inconel sheathed Type-K thermocouple placed in the thermowells at the center of the panel. The temperatures were measured for each panel in a single row and averaged together so that the row could be controlled using a WATLOW SD PID controller. This allows for the temperatures of any individual row to be controlled.

3.3 Sandwich Composite Manufacturing

The sandwich composite samples utilized in this study were manufactured using the Vacuum Assisted Resin Transfer Molding (VARTM) technique (Figure 7) without post-curing. The facesheet material was a Colan AR105 0.83 kg/m^2 woven roving plain weave E-glass fiber with a warp/weft ratio of 5:4 and an approximate single layer thickness of 0.635 mm. The core material was BALTEK SB.100 balsa wood in 6.35 and 12.7 mm nominal thicknesses. The resin used was Derakane 411-350 vinyl ester. The resin cure package used consisted of MEKP (1.5% by total weight), 2, 4-Pentedione (0.065% by total weight), and cobalt napthanate (0.2% by total weight). Prior to resin infusion, the sandwich composite layup was kept under 1 atm of vacuum for 24 hours to reduce any moisture present in the balsa core material.

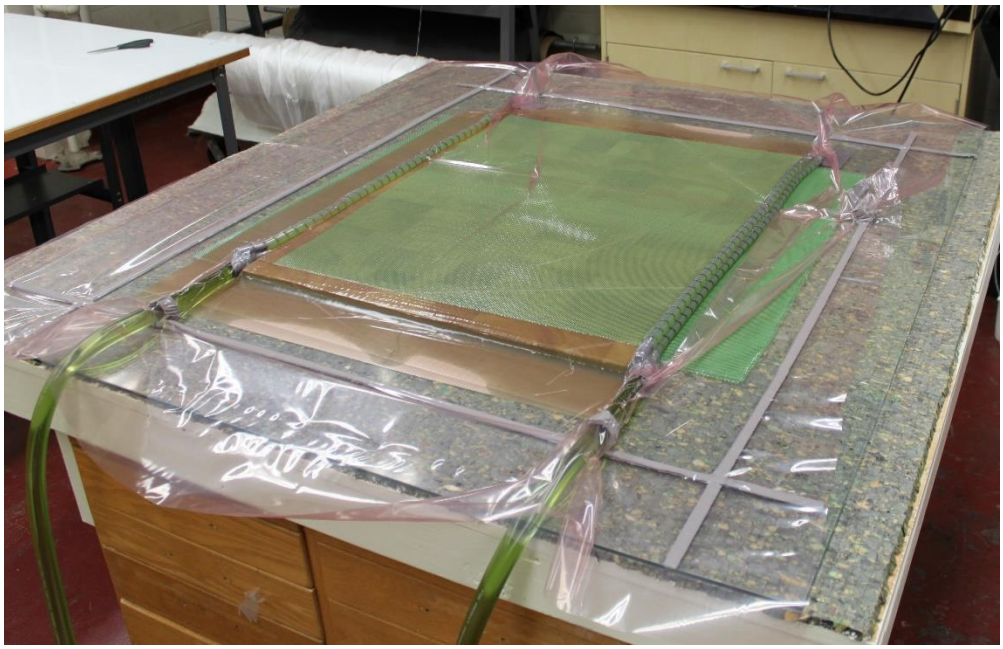

Fig. 7. Sandwich composite layup using VARTM after resin infusion.

3.4 Material Properties

In order to accurately model the sandwich composite response at high temperatures, material properties ranging from ambient to above the glass transition temperature, T_g, must be obtained. In addition to this, the woven E-glass facesheet is to be considered fully orthotropic such that all nine independent material properties can be used in a future finite element analysis. Determining these material properties as a function of temperature is challenging, as high temperature mechanical tests are more complicated to perform than tests at room temperature, especially when transverse properties are needed. One potential solution to this problem is to use the experimentally obtained temperature dependent in-plane properties combined with a micromechanics-based averaging approach to derive the remaining unknown properties.

With regard to the balsa core material, the inherent structure of the wood makes property determination a difficult task even at room temperature; high temperature measurements are even more challenging. Balsa core sheets are made up of smaller balsa core sections that have a cellular structure similar to what is seen in the cross section of a tree trunk. These smaller balsa sections

are then bonded together under pressure at high temperatures to create the final sheet material (Figure 8).

Fig. 8. Balsa core sheet shown with individual region highlighted. Note that each region can be described by a (r,θ,z) system and that the bonded surfaces are clearly visible between any two regions.

This means that each individual section would most appropriately be described as orthotropic in an (r, θ, z) system but due to the combination of many smaller sections, no natural orthotropic system is readily available. In this work the balsa core sheet will be assumed to be transversely isotropic and temperature dependent properties obtained by observing the in-plane and transverse strengths from experimental data taken at high temperatures.

3.4.1 E-Glass/Epoxy Properties

In-plane mechanical properties for a similar fiber/epoxy system were measured experimentally by Boyd [30] through a range of temperatures. The specific material tested was a Vetrotex 324 24 oz/yd (0.81 kg/m^2) E-glass woven roving and Derakane 510A-40 epoxy laminate manufactured using the VARTM method with additional post-curing. A summary of the experimental values is given in Table 1.

Table 1: In-Plane Temperature Dependent Material Properties, Boyd, S.E., "Compression Creep Rupture of an E-glass / Vinyl Ester Composite Subjected to Combined Mechanical and Fire Loading Conditions," Ph.D dissertation, Virginia Polytechnic Institute and State University, 2006. Used under fair use, 2015.

T (°C)	E_{xx} (GPa)	T (°C)	E_{yy} (GPa)	T (°C)	G_{xy} (GPa)
24.6	33.9	24.6	27.4	26.9	5.21
90.4	31.9	89.6	27.2	59.8	4.78
104.4	31.3	104.4	25.2	89.9	4.57
119.7	22.9	119.7	17.5	104.6	3.61
120.2	21.7			119.7	1.63
129.9	20.3			129.7	0.47
				139.8	0.14
				149.8	0.11
				159.8	0.16
				169.9	0.12
				177.1	0.11

In addition to these, the experimentally measured in-plane Poisson ratio, ν_{xy}, at room temperature is 0.14. It is assumed independent of temperature. These property values are then fit to a hyperbolic function (1) used originally by Gibson *et al.* [31] and later developed further by Feih *et al.* [32, 33].

$$P(t) = \frac{P_{c(0)} + P_{c(R)}}{2} - \frac{P_{c(0)} - P_{c(R)}}{2} tanh[k_m(T - T_k)] \quad (1)$$

where P can represent material properties such as elastic moduli (E_{xx}, E_{yy}, G_{xy}, etc), or strength values. Fitting an equation of the form (1) to the experimental values using a nonlinear curve-fitting routine *lsqcurvefit* in Matlab results in the following set of parameters shown in Table 2.

Table 2: Nonlinear Fit Parameters of Degradation Equation (1)

Property	$P_{c(0)}$	$P_{c(R)}$	k_m	T_k
E_{xx}	33.86	19.88	0.0997	112.2
E_{yy}	23.37	15.06	0.0973	112.5
G_{xy}	4.96	0.0695	0.0607	112.5

Using the parameters shown below results in the following temperature degradation curves for the in-plane moduli (Figure 9a-b).

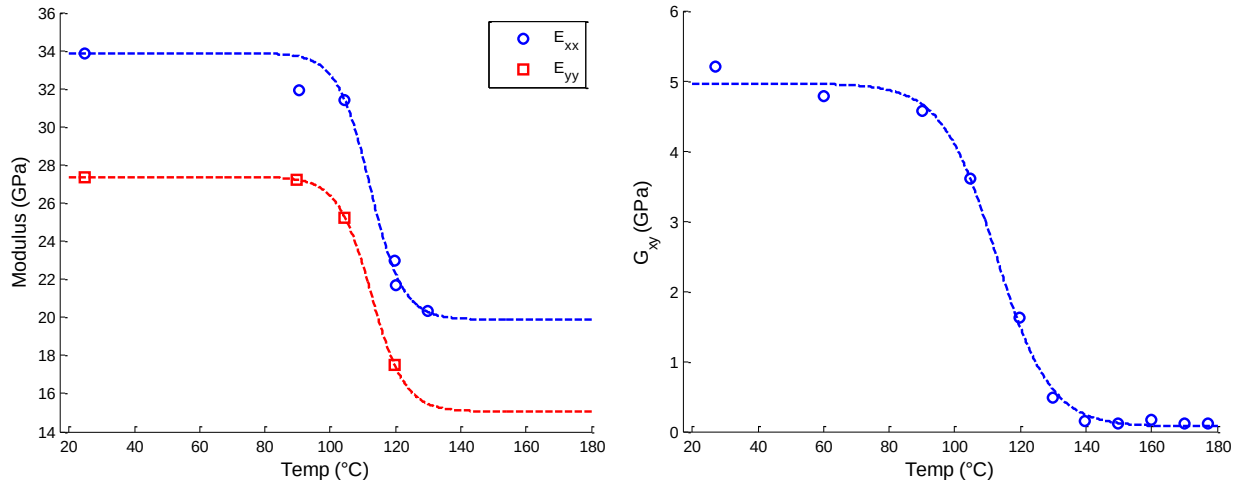

(a) (b)

Fig. 9. Temperature dependent material property curves (1) using nonlinear fitting parameters shown in Table 2.

3.4.1a Transverse Property Determination

The process of determining the remaining five orthotropic properties of the woven laminate employed a combination of micromechanics and averaging approaches. First, the warp and weft tows will be treated as individual laminae to determine their orthotropic properties. This will utilize room temperature experimental data from Table 1 to find their respective volume fractions. Then using the known warp/weft ratio of the fabric, an averaging approach will be used to determine the remaining woven laminate properties.

Using the room temperature in-plane elastic moduli (E_x, E_y) from Table 1 and the 5:4 warp/weft ratio, Equations (2) and (3) can be used to determine the volume fraction, V_f, of the warp and weft tows.

$$E_x = 0.55(E_1)_{warp} + 0.45(E_2)_{weft} \tag{2}$$

$$E_y = 0.55(E_1)_{weft} + 0.45(E_2)_{warp} \tag{3}$$

Using the standard rule of mixtures approach (4) for the E_1 terms and the improved mechanics of materials model (5) developed originally by Hopkins and Chamis [34] and then modified by Case [35] for the E_2 terms,

$$E_1 = E_f V_f + E_m(1 - V_f) \tag{4}$$

$$\frac{1}{E_2} = \frac{1 - \sqrt{V_f}}{E_m} + \frac{\sqrt{V_f}}{E_f\sqrt{V_f} + \left(1 - \sqrt{V_f}\right)E_m} \tag{5}$$

where E_f and E_m are the fiber and matrix elastic modulus respectively. This now gives a system of two equations that can be solved for the warp volume fraction, $\left(V_f\right)_{warp}$, and the weft volume fraction, $\left(V_f\right)_{weft}$.

With the properties of the E-glass fiber and Derakane matrix known, assuming both to be isotropic, and the volume fractions of the warp and weft tows found from (, 3), a concentric cylinders micromechanics model [36] can be used to find the nine orthotropic material constants for the warp and weft tows. A summary of the results up to this point is shown in Table 3.

Table 3: Orthotropic Properties for Warp and Weft Tows

	E-Glass Fiber [37]	**Derakane** [37]	**Warp Tow** ($V_f = 0.732$)	**Weft Tow** ($V_f = 0.473$)
E_{11} **(GPa)**	72.5	3.10	53.9	36.0
E_{22} **(GPa)**	72.5	3.10	17.8	8.87
E_{33} **(GPa)**	72.5	3.10	17.8	8.87
G_{23} **(GPa)**	30	1.15	6.86	3.24
G_{13} **(GPa)**	30	1.15	6.01	2.94
G_{12} **(GPa)**	30	1.15	6.01	2.94
ν_{23}	0.208	0.350	0.302	0.371
ν_{13}	0.208	0.350	0.239	0.273
ν_{12}	0.208	0.350	0.239	0.273

With the properties known for both the warp and weft tows, averaging equations (6-10) using the warp/weft ratio can be used for the remaining five properties of the woven laminate.

$$\frac{1}{E_z} = \frac{0.55}{(E_3)_{warp}} + \frac{0.45}{(E_3)_{weft}} \tag{6}$$

$$\nu_{xz} = 0.55(\nu_{13})_{warp} + 0.45(\nu_{23})_{weft} \tag{7}$$

$$\nu_{yz} = 0.45(\nu_{13})_{weft} + 0.55(\nu_{23})_{warp} \tag{8}$$

$$\frac{1}{G_{xz}} = \frac{0.55}{(G_{13})_{warp}} + \frac{0.45}{(G_{23})_{weft}} \tag{9}$$

$$\frac{1}{G_{yz}} = \frac{0.55}{(G_{23})_{warp}} + \frac{0.45}{(G_{13})_{weft}} \tag{10}$$

Using the warp and weft properties from Table 3 in Equations (6)-(10) along with the room temperature experimental values gives the complete set of orthotropic material parameters for the E-Glass/epoxy laminate shown in Table 4.

Table 4: Orthotropic Properties for E-Glass/Epoxy Woven Laminate

	E-Glass/Epoxy Laminate
$\boldsymbol{E_{xx}}$ **(GPa)**	33.9
$\boldsymbol{E_{yy}}$ **(GPa)**	27.4
$\boldsymbol{E_{zz}}$ **(GPa)**	12.3
$\boldsymbol{G_{yz}}$ **(GPa)**	4.31
$\boldsymbol{G_{xz}}$ **(GPa)**	4.35
$\boldsymbol{G_{xy}}$ **(GPa)**	5.21
$\boldsymbol{\nu_{yz}}$	0.281
$\boldsymbol{\nu_{xz}}$	0.297
$\boldsymbol{\nu_{xy}}$	0.140

High temperature properties for the remaining transverse moduli (E_{zz}, G_{xz}, G_{yz}) not measured by Boyd [30] will be determined by making three assumptions. First, the properties of the E-glass fiber are independent of temperature and thus remain constant. Second, only the moduli of the Derakane epoxy matrix (*E*, *G*) degrade as the temperature increases. Lastly, the material degradation curves can be represented by the same hyperbolic function shown in Equation (1).

Using the experimentally measured values for E_x from Table 1 in Equation () with the use of Equations (6)–(10) and the volume fractions of the warp and weft tows previously solved for (Table 3) enables one to solve for the temperature dependent elastic modulus of the matrix, E_m. The concentric cylinders model is again used to find the orthotropic properties of the warp/weft

tows and finally Equations (6)-(10) give the transverse temperature dependent properties of the woven laminate. These are shown below (Figure 10) overlaid on the experimentally fit curves from Figure 9.

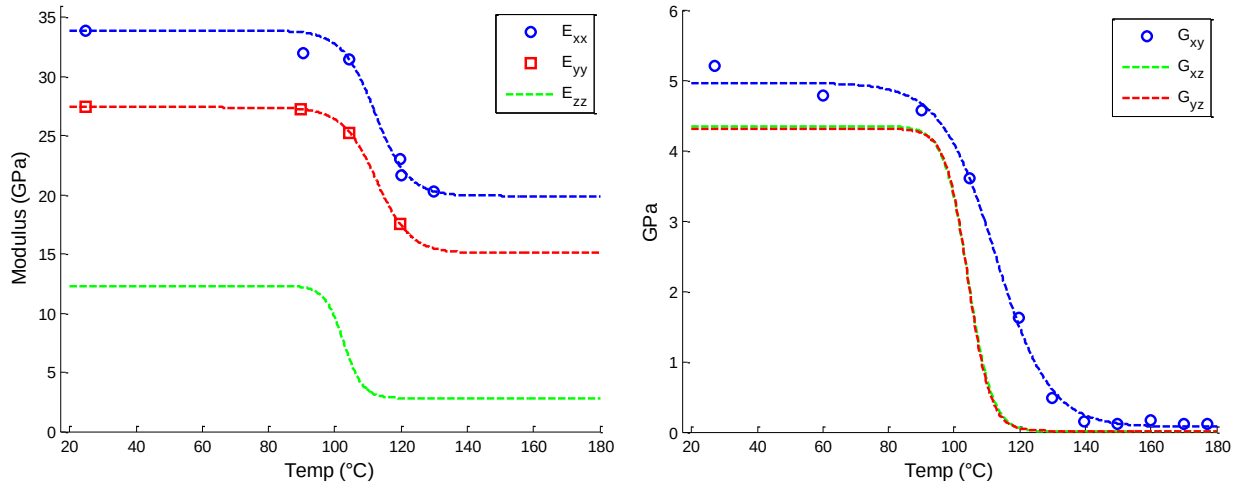

(a) (b)

Fig. 10. Estimates for the temperature dependent transverse moduli.

Relevant thermal properties to be used in the analysis are shown in Table 5 and are taken from Lattimer and Ouellette [38].

Table 5: Thermal Properties for Woven E-glass/Derakane 510A Epoxy Laminate

Coefficient of Thermal Expansion		
$\boldsymbol{\alpha_x}$ **(/°C)**		1.74 x 10^{-6}
$\boldsymbol{\alpha_y}$ **(/°C)**		2.14 x 10^{-6}
Thermal Analysis Parameters		
$\boldsymbol{\rho}$ **(kg/m^3)**	Density	1683
k (W/m-°C)	Thermal Conductivity	0.31
$\boldsymbol{C_p}$**(J/kg-°C)**	Specific Heat Capacity	1090
$\boldsymbol{\alpha}$ **(m^2/s)**	Thermal Diffusivity	1.4 x 10^{-7}

3.4.2 Balsa Core Properties

The core material used was BALTEK SB.100 balsa wood cut perpendicular to the grain. Properties of the balsa core material are compiled from a combination of sources due to a lack of single complete experimental dataset. The transverse elastic modulus, E_{33}, is taken from the material data sheet provided by BALTEK [39] while all other properties are derived by relations formulated by Tagarielli *et al*. [40]. In this work, relationships between the density of the balsa wood and its mechanical properties in Equations (11) and (12) are established and compared to experimental data,

$$E_{11} = E_{22} = 76\left(\frac{\rho}{\rho_o}\right)^3 \tag{11}$$

$$G_{13} = G_{23} = 80\left(\frac{\rho}{\rho_o}\right) \tag{12}$$

where the coefficients of each equation were obtained experimentally in Tagarielli *et al*. [40] and ρ_o is a reference density taken as 100 kg/m^3. A summary of the mechanical properties of the balsa core is given in Table 6.

Table 6: Transversely Orthotropic Properties for Balsa Core

	Balsa Core (BALTEK SB.100)
$\boldsymbol{E_{11} = E_{22}}$ **(MPa)**	272
$\boldsymbol{E_{33}}$ **(MPa)**	3570 (Tension)
$\boldsymbol{E_{33}}$ **(MPa)**	4005 (Compression)
$\boldsymbol{G_{13} = G_{23}}$ **(MPa)**	122.4
$\boldsymbol{G_{12}}$ **(MPa)**	113.3
$\boldsymbol{\nu_{13} = \upsilon_{23}}$	0.10
$\boldsymbol{\nu_{12}}$	0.20

There are two items of particular note in the above table: the Poisson's ratio values and the in-plane shear modulus. First, the values presented for the Poisson ratios in [40] were found to be

independent of the density of the balsa wood. Second, the in-plane shear modulus was calculated using the transversely isotropic material relation (13) between the in-plane properties.

$$\frac{E}{2G} = 1 + \nu \tag{13}$$

Temperature dependent material properties were obtained by first observing the degradation of the in-plane (radial) and transverse (axial) strengths (Figure 11) from experiments performed by Goodrich *et al*. [41]. These are then fit with piecewise linear functions and scaled using the room temperature properties (Figure 12) shown in Table 6. Relevant thermal properties shown in Table 7 obtained from Feih *et al*. [42].

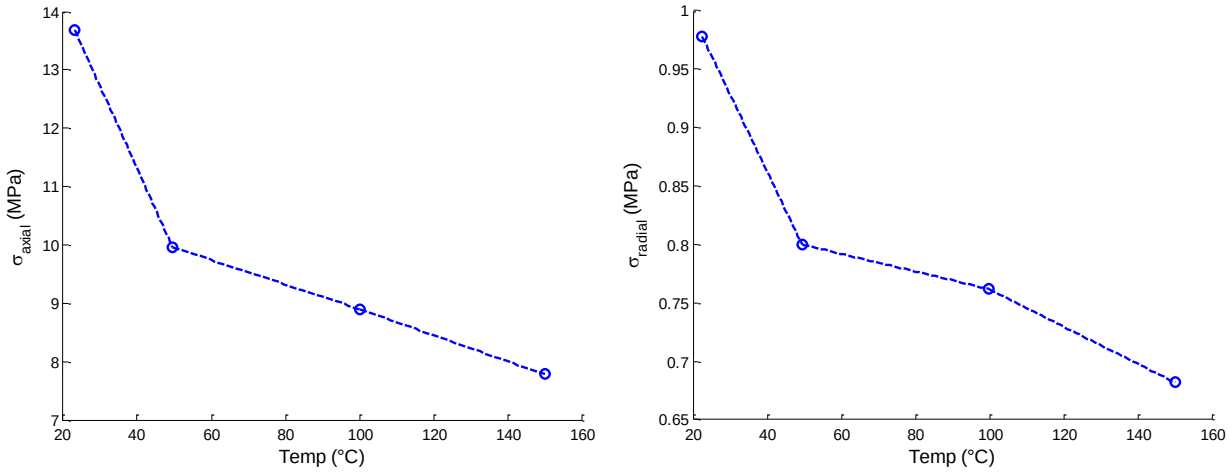

(a) (b)

Fig. 11. (a) Transverse (axial) compressive strength. (b) In-plane (radial) compressive strength.

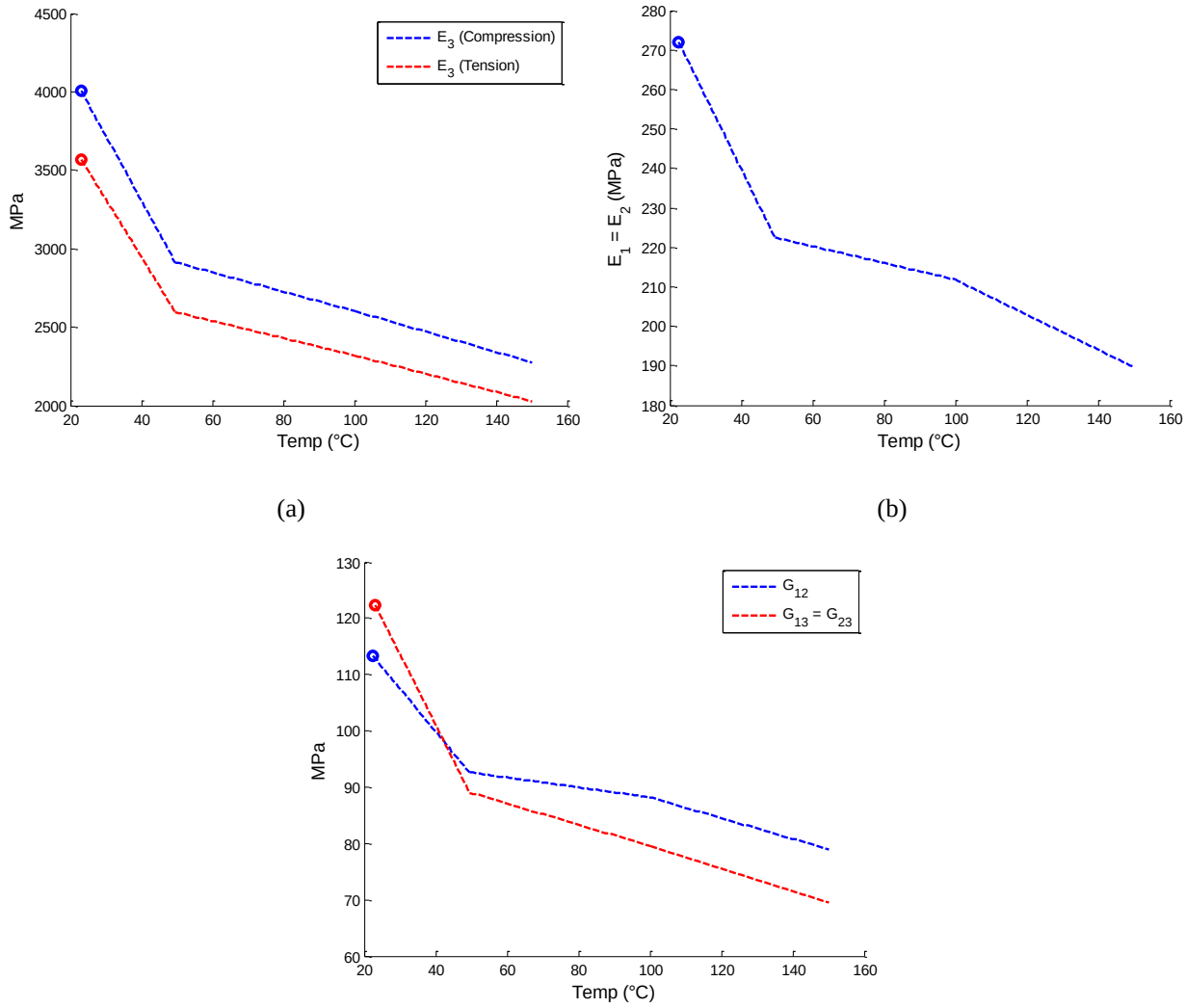

Fig. 12. Temperature dependent material properties for balsa core. (a) Transverse elastic modulus for tension and compression. (b) In-plane elastic modulus are equal due to transverse isotropy assumption. (c) In-plane and transverse shear moduli. Room temperature values from Table 6 shown in each plot.

Table 7: Thermal Properties for Balsa Core Material

Coefficient of Thermal Expansion[1]		
α (/K)		47.5 x 10^{-6}
Thermal Analysis Parameters[2]		
ρ (kg/m^3)	Density	153
k (W/m-K)	Thermal Conductivity	0.2
C_p(J/kg-K)	Specific Heat Capacity	1420+0.68(T)

1. CTE value obtained from Idemat 2003.
2. Assumes a moisture content of 8 wt%.

3.5 Fracture Tests

Mode I and II fracture tests were performed to determine fracture toughness and observe the balsa core damage with increasing temperature. Because the fracture interface lies between two different material types, the Mode I and II stresses are inherently coupled [43,44] together in a cyclic manner. This means that a pure Mode I stress state cannot be achieved and many of the standard experimental techniques and data reduction approaches used in fracture mechanics gain a greater level of complexity. Even so, investigators [13] have used the traditional fracture mechanics approaches to describe the interface fracture of sandwich composites with success and a similar path was followed in this work.

In order to obtain apparent Mode I and II fracture toughness values, the layup of the sandwich composite test articles were modified to ensure high mode-mixity values for the respective Mode I and II tests performed. These values are typically difficult to obtain since the interface between the core and facesheet is shifted away from the neutral axis of the sandwich composite, causing both peel and shear stresses to exist even for typically "pure" Mode I and II tests. By modifying each facesheet layup so that the neutral axis aligns with the interfacial plane, a nearly "pure" mode situation can be obtained. Such a condition was obtained by using a sandwich specimen that has approximately the same bending stiffness above and below the fracture interface (Figure 13).

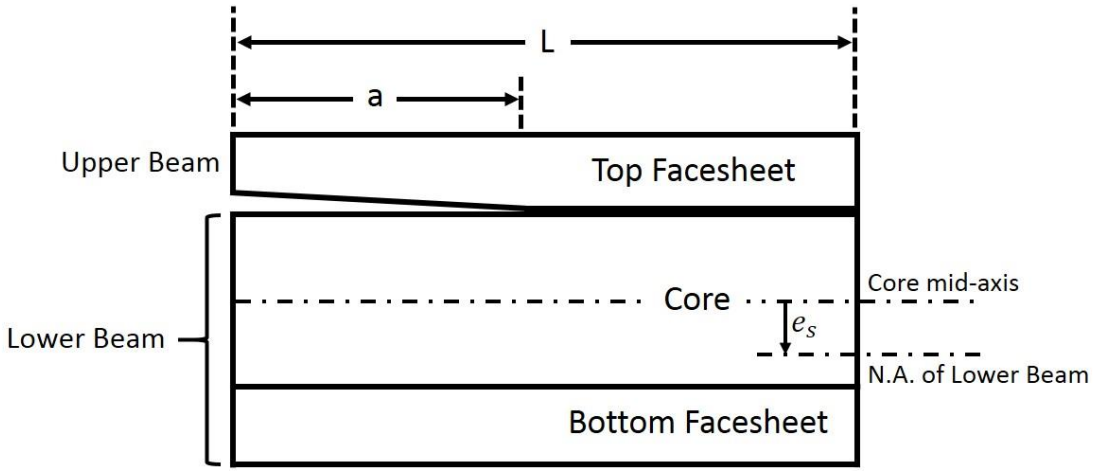

Fig. 13. Diagram of sandwich composite sample where modification of the top and bottom facesheet ply layups drive the neutral axis of the uncracked portion to coincide with the interfacial fracture plane.

This technique was used by Davidson *et al.* [8] to determine G_{Ic} and G_{IIc} values of an unspecified sandwich composite system. They were able to obtain Mode I contributions to the fracture energy greater than 90% (determined using FE analysis) while showing approximately constant values independent of fracture length for both Mode I and II tests.

Using the facesheet and core material properties given in Table 4 and Table 6, a mechanics of materials approach given in Equations (14) and (15) was used to calculate the bending stiffness of the upper and lower beams in Figure 13.

$$D_{up} = \frac{E_{f1} b h_{f1}^3}{12} \tag{14}$$

$$D_{low} = E_c b \left(\frac{h_c^3}{12} + h_c e_s^2 \right) + E_{f2} b \left[\frac{h_{f2}^3}{12} + h_{f2} \left(\frac{h_{f2} + h_c}{12} - e_s \right)^2 \right] \tag{15}$$

where E_{f1}, E_{f2}, and E_c are the in-plane modulus in the axial direction of the sample for the upper facesheet, lower facesheet, and core respectively. The neutral axis of the lower beam, e_s, is a function of the layup and thickness of the bottom facesheet while the thickness, b, remains

constant. Additionally, the change in properties as a function of temperature was taken into account in the bending stiffness calculation for temperatures of 60°C, 80°C and 100°C. An optimization routine was created to find the upper and lower facesheet ply layup that would minimize the difference between the two overall beam bending stiffnesses. The sandwich composite layup results are shown in Table 8 along with the percent difference in the bending stiffness between the upper and lower beams.

Table 8: Upper and Lower DCB Bending Stiffness

	Upper Beam		*Lower Beam*		
Temperature (°C)	**Layup**	**D_{up} (N-m)**	**Layup**	**D_{low} (N-m)**	**% Diff.**
RT ($\cong 25°C$)	$[0_6]$	158.7	$[Balsa, 90_6]$	180.0	13.4
60		158.5		169.1	6.59
80		158.5		168.1	6.06
100		153.4		163.8	6.80

3.5.1 Mode I Fracture Test Setup

Sandwich composite panels with facesheet ply layups shown in Table 8 were made using the previously described VARTM method. A 0.0635 x 25.4 mm piece of Kapton® film was placed on the upper surface of the balsa core prior to manufacturing so that an initial weakened interface could be created on the sought after interfacial plane. While this film material is meant to prevent the epoxy from bonding to the balsa core surface creating the initial debond, it was observed that a small amount of bonding did occur which necessitated the use of a steel wedge to create the actual debonded region (Figure 14).

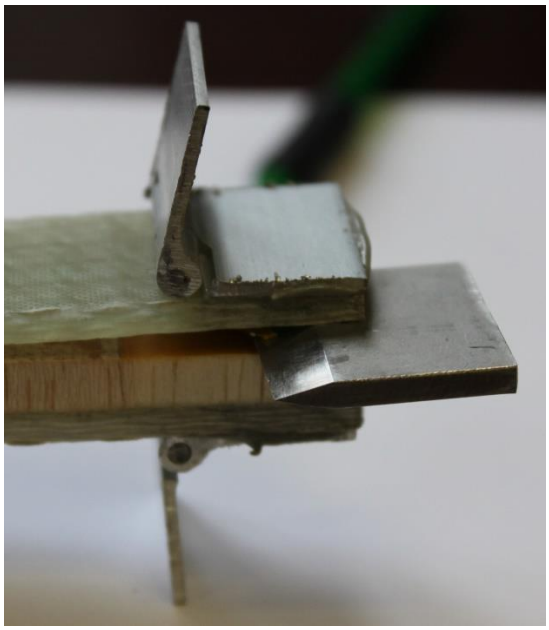

Fig. 14. DCB sample end with piano hinges bonded and steel wedge instrument for creating debond.

Afterwards, 25.4 x 210 mm samples were dry cut using a diamond saw and both facesheet surfaces were cleaned with acetone to remove any contaminants from the manufacturing and machining processes. Extruded-aluminum aerospace grade piano hinges were then bonded to the facesheets (Figure 14) using a LORD 320/322 epoxy adhesive and allowed to cure for 24 hours to create the DCB test specimen. Prior to the adhesive application, each facesheet surface and the corresponding hinge contact surface were roughened with a 120 grit sandpaper to aid in bonding. After adhesion of the piano hinges, one side of the sample was speckled using a matte black and white Rust-Oleum high temperature spray paint to aid in observation of crack growth.

All DCB tests were performed using an MTS 4204 load frame with an Instron 1 kN static load cell operated in displacement control at a rate of 1.25 mm/min. Heat was applied using an Instron 3116 Oven with the door unattached and an insulation board in its place held to the oven with ratchet straps on either side. All high temperature tests were maintained at the desired temperature for 15 min to ensure no temperature gradient existed within the sample. This insulation board had a small rectangular region cut out to permit viewing the sample throughout the entire test by a two camera optical DIC system. Additionally a FLIR SC655 thermographic camera was used to observe the temperature of the sample during the test. While some amount of heat was lost through the opening

in the insulation board, the oven was still able to maintain a consistent set-point temperature due to the low overall temperatures of the tests. A picture of the entire test setup is shown in Figure 15a-c.

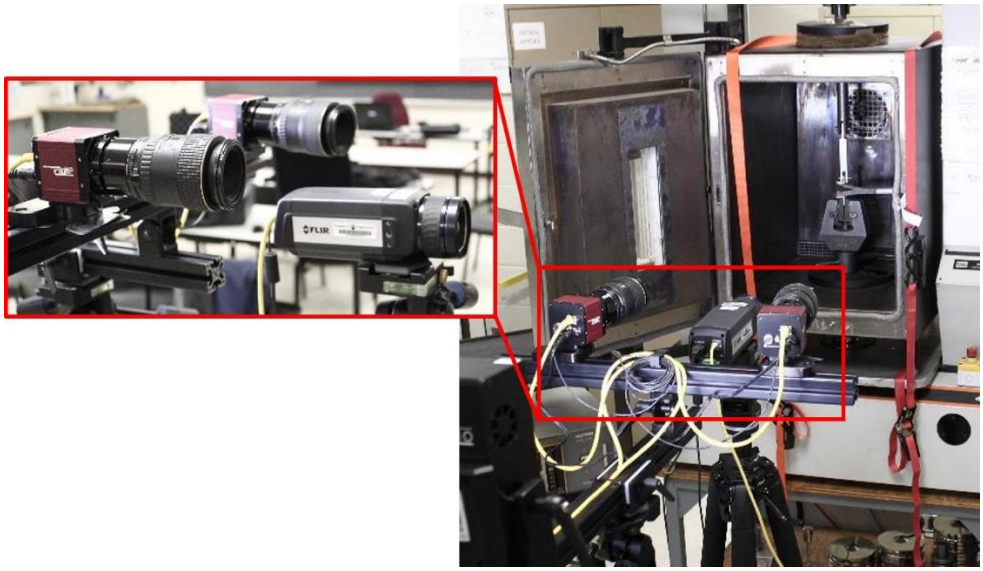

(a)

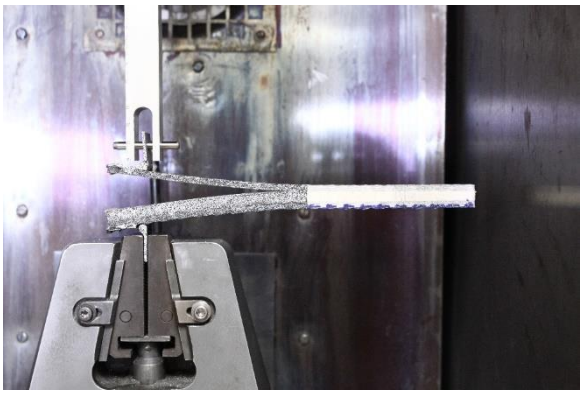

(b)

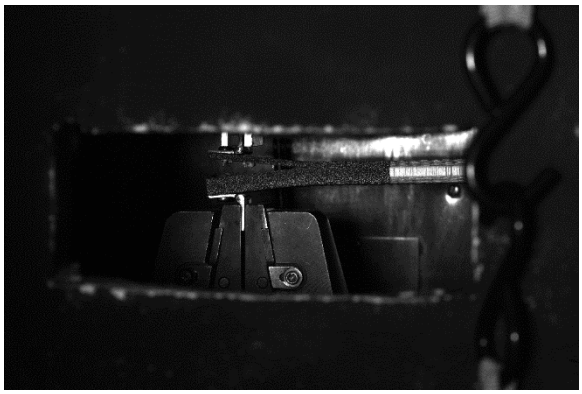

(c)

Fig. 15. Overview of DCB test setup. (a) Two 3D DIC cameras are used to track crack growth while a FLIR SC655 thermographic camera observes temperature. (b) Sample is pin loaded with a dowel pin inserted through the piano hinge. (c) View from one of the two DIC cameras showing cutout formed in insulation board.

While the adhesive is meant to be used at high temperatures, inadequate bonding occurred for all tests 60°C and higher. This led to either a total failure of the adhesive resulting in debonding from the surface, or softening that allowed the adhesive between the hinge and facesheet to deform under loading. Since the calculation of the strain energy release rate does not take into account the

strain energy of the deformed adhesive, this will lead to inaccurate results for the fracture toughness, G_{Ic}. In an effort to remedy this, two small 3/16" screws were used to attach the piano hinge to the DCB sample as shown in Figure 16. While this kept the hinge attached to the sample for all high temperature tests, there was some bending observed in the hinge which altered both the total strain energy of the entire system and the crack length during the test.

Fig. 16. Screws used to attach aluminum piano hinge to facesheet surface.

3.5.1a Data Reduction Method for G_{Ic}

The modified beam theory (MBT) method [45] will be used to determine the Mode I critical strain energy release rate. This method was found by Shivakumar and Chen [5] to produce the most consistent results while minimizing area and uncertainty. The techniques they investigated include the traditional Compliance Calibration (CC) method along with three alternatives: Modified Beam Theory (MBT), Modified Compliance Calibration (MCC), and the area method. The results showed comparable results were obtained using either MBT or MCC methods so long as the specimen length to debond length ratio was less than 0.53, after this specimen end effects introduced significant nonlinearity. The MBT method was determined to be superior though due to its overall simplicity to use and consistent results obtained.

The starting point for developing the MBT method [45] is the traditional beam theory expression shown in equation (16) as,

$$G_{Ic} = \frac{3P\delta}{2ba} \tag{16}$$

where P is the load, δ is the load point displacement, b is the sample width, and a, the delamination length. This expression formulation starts with the assumption that the ends of each beam in the DCB sample have a fixed boundary condition at the crack-tip. When sandwich composites are used in DCB tests it is often difficult to ensure that there is no crack-tip rotation occurring. This is due to each beam of the DCB most likely having unequal bending stiffness and that a bimaterial interface is occurring at the crack-tip where one of the adherends (core) is often much more compliant than the other (facesheet). These factors lead to the beam theory expression in Equation (16) overestimating the Mode I energy release rate due to the stiffening effect of the fixed boundary condition.

This problem is remedied in the MBT method by treating the debond length to be longer, $a + |\Delta|$, where Δ is determined experimentally. Then by generating a least square plot of the cube root of the compliance, $C^{1/3}$, as a function of the delamination length, the x-intercept of this plot (Figure 17) is the additional length required in the MBT energy release rate Equation (17).

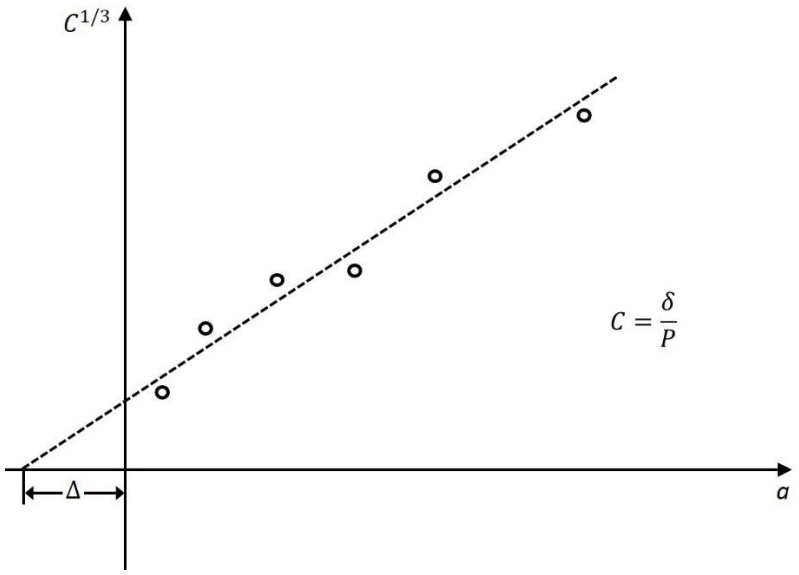

Fig. 17. Plot of the cube root of the compliance. Using a least squares method provides the correction added to the crack length in the MBT equation (17).

$$G_{Ic} = \frac{3P\delta}{2b(a + |\Delta|)} \tag{17}$$

3.5.2 Mode II Fracture Test Setup

Samples manufactured and prepared using the same process and dimensions described in the previous *Mode I Fracture Test Setup* (Table 8) were used for the Cracked Split Beam (CSB) test to determine a Mode II fracture toughness, G_{IIc}. The test setup consists of nothing more than what is required to perform a typical three-point bend test. Since a sliding dominant mode is sought after, friction between the debonded portion of the facesheet and core material could interfere with the results. To remedy this, a 24 gauge galvanized steel wire is placed between the facesheet and core in the debonded region just above the support point to minimize the frictional energy expended throughout the test. While this will introduce a slight opening displacement at the crack-tip increasing the Mode I component, as the crack increases in length this will reduce as shown in Adams *et al*. [12]. An overview of the test setup is shown in Figure 18.

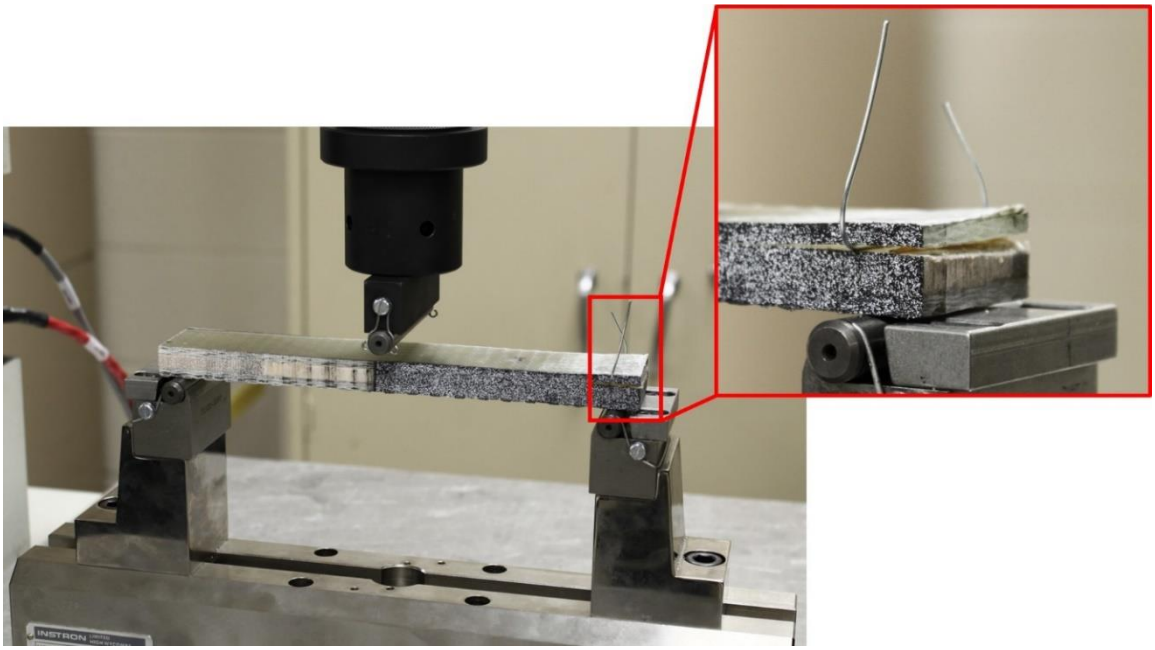

Fig. 18. Overview of the CSB test configuration including spacer wire in debond section above roller support.

All tests were performed on an MTS 4204 load frame with an Instron 5 kN static load cell in displacement control at 1.25 mm/min. Spacing between roller supports was kept fixed at 190 mm and the same two camera optical 3D-DIC system as in the Mode I DCB tests was used to observe crack growth. The test was stopped just prior to the crack reaching the loading point in the middle of the sample or if any crack kinking was observed. Due to size limitations of the fixture and oven, no high temperature tests were undertaken for the temperature dependent Mode II fracture toughness.

3.5.2a Data Reduction Method for G_{IIc}

While an ASTM standard exists for the determination of the Mode I energy release rate, no similar document has been developed for Mode II. This has led to numerous test configurations for the investigation of the sliding energy release rate. For this investigation the cracked split beam (CSB) test [19] will be used to determine Mode II properties. This is chosen due to the very simple test configuration, requiring only those items used in a typical three-point bend test and shown in Figure 19.

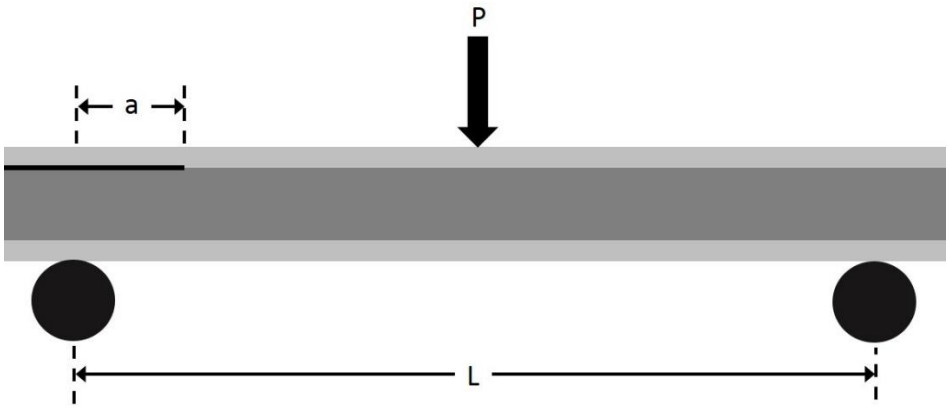

Fig. 19. The cracked split beam (CSB) test configuration. Note that the initial fracture length is taken from the support to the crack-tip. A wire will be placed between the facesheet and core above the support on the cracked side to minimize frictional forces that could develop.

One slight difference from a three-point bend test on non-cracked specimens is the use of a spacer wire to separate the debonded facesheet from the lower core/facesheet member. This acts to prevent the introduction of frictional forces from being developed and was used by Adams *et al*. [12] where a modified three-point test fixture was used to hold a tightened wire in place throughout the test. In their same work it was shown that near the support point on the crack side the total energy release rate was initially Mode I dominant, but as the crack progressed towards the center load point, the Mode II dominance increased as well.

For determination of the Mode II energy release rate, G_{IIc}, the compliance calibration method is used [46]. The starting point of this technique is the Irwin-Kies Equation (18),

$$G_{IIc} = \frac{P^2}{2b}\frac{dC}{da} \tag{18}$$

where P is the centrally applied load, b is the sample width, and C is the compliance which is a function of the crack length a. Using the experimental data, a cubic polynomial of the form in Equation (19) is fitted to the data where C_0 and C_1 can be found by plotting the compliance against the cube of the crack length.

$$C = C_0 + C_1 a^3 \tag{19}$$

Using Equation (19) in Equation (18) gives the following form in Equation (20) for the Mode II energy release rate.

$$G_{IIc} = \frac{3P^2C_1a^2}{2b} \tag{20}$$

3.6 Intermediate-Scale Test Articles

Sandwich composite column test articles were tested in the intermediate-scale load frame under two flux levels of one-sided heat exposure. All facesheets were made with the previously described Colan AR105 woven roving plain weave E-glass fiber and a Derakane 411-350 vinyl-ester. A total of three plies were used for each facesheet with a warp-aligned orientation for all tests and two thicknesses of BALTEK SB.100 end grain balsa core were used (6.35 mm and 12.7 mm). In all samples with the 6.35 mm balsa core, a debond was formed in the center of the sample by layering two sheets of 0.3 mil thick, 88.9 mm wide Kapton® HN film provided by CS Hyde Company. While this was found to work suitably to create the debond between the facesheet and core, the extremely small thickness proved difficult to cut into the desired size. A change was made for all samples using the 12.7 mm core thickness to use two layered sheets of a 1 mil by 88.9 mm wide Skived Polytetrafluoroethylene (PTFE) film (CS Hyde Company, Lake Villa, IL). Three nominal sample sizes were tested and shown below in Table 9, for specific sample dimensions consult Table A1 in the appendix. Note that the length of the gripped region on each end was 101.6 mm so the ungripped length used in all future buckling load calculations is also provided.

Table 9: Nominal Sample Dimensions for Intermediate-Scale Testing

Core Thickness (mm)	Total Thickness (mm)	Width (mm)	Overall Length (mm)	Ungripped Length (mm)
6.35	10	95	735	532
12.7	16		585	382

*All debond samples had an 88.9 mm wide debond located in the center of the sample.

3.6.1a One-Sided Heat Exposure Levels

Tests were performed at ambient (22°C) and two incident heat flux levels. Heat was applied by positioning the 3 x 2 quartz heater panels 0.56 m from the surface of the sample and setting the set-point temperature to either 670°C or 890°C. The incident heat flux from these heater panel

temperature settings was found by placing a 914 x 914 x 0.793 mm stainless steel sheet within the load frame (Figure 20) in the same plane as the samples exposed surface.

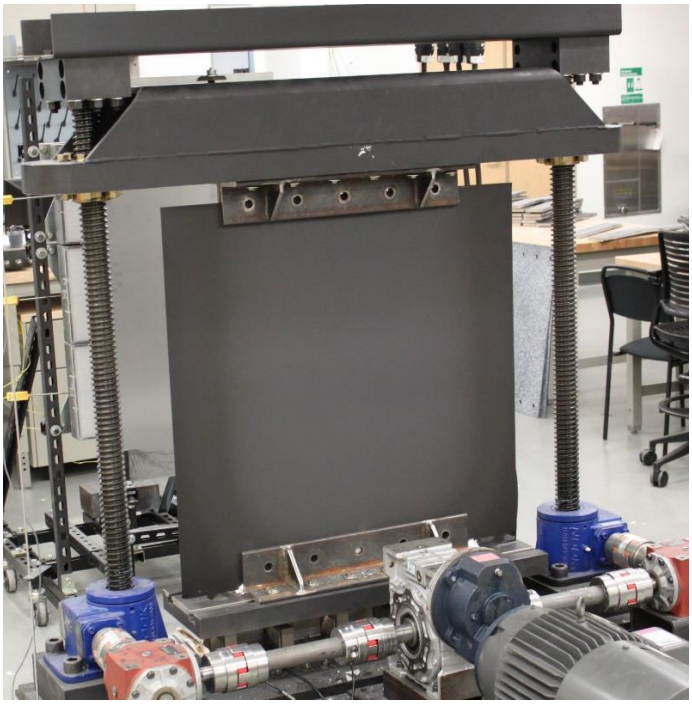

Fig. 20. Stainless steel sheet used for flux mapping.

A coating of Rust-Oleum matte black paint (ϵ = 0.95) was applied to both surfaces of the steel sheet so that a known surface emissivity [47] could be used. Next, by recording the temperatures on the unexposed side of the sheet using a FLIR SC655 thermographic camera, and assuming no through-thickness temperature variation, a flux mapping can be calculated using the technique described in Rippe and Lattimer [29]. The temperature measurements and corresponding flux mappings are shown in Figure 21 for both incident flux exposures.

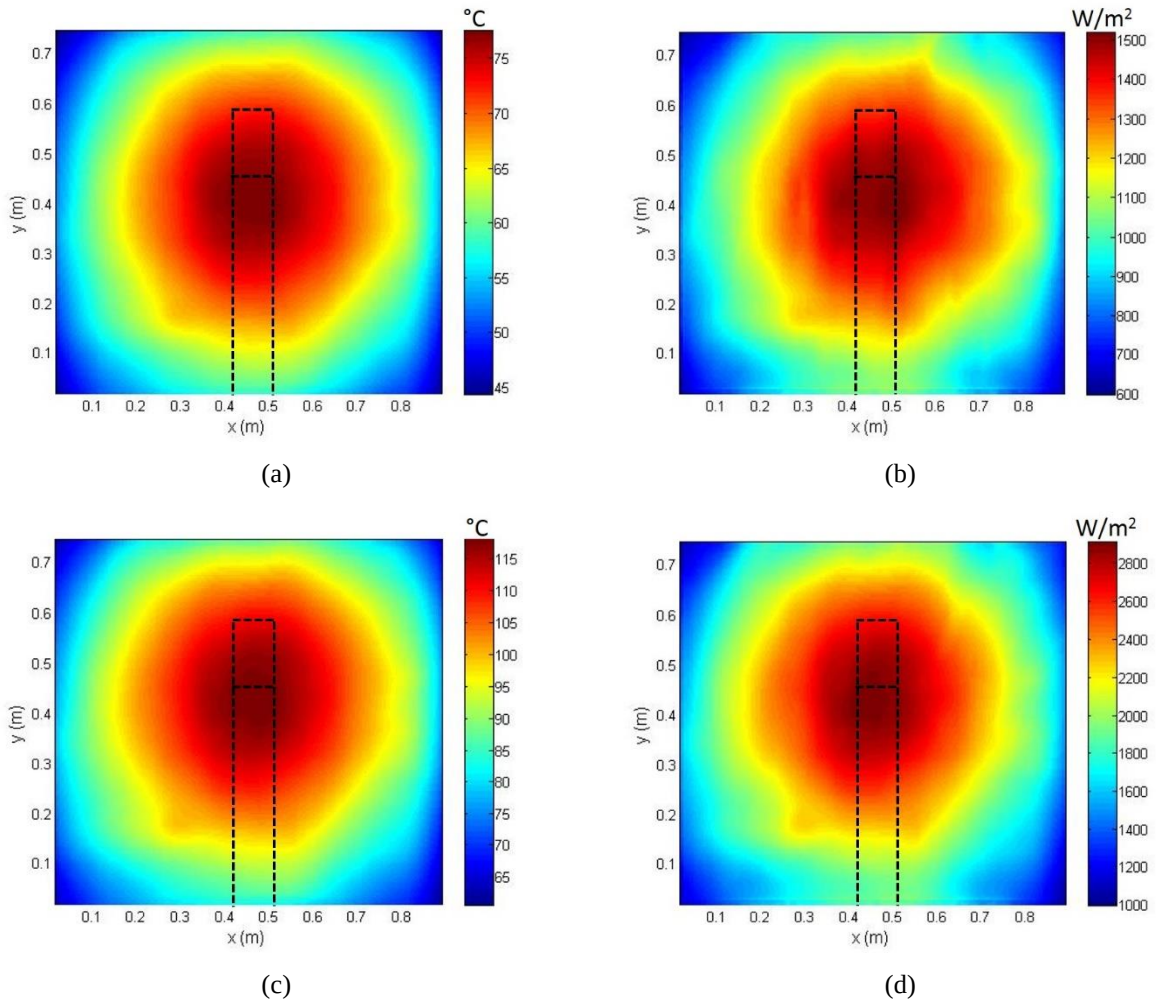

Fig. 21. Heat flux and temperature contours including an outline of where test articles are located. (a) Temperature mapping of low flux level, (b) heat flux mapping of low flux level, (c) temperature mapping of high flux level, and (d) heat flux mapping of high flux level.

In the previous figure the position where the sample resides has been marked off by the dashed lines for both sample lengths. A minimal variation along the sample width of the applied flux is observed but lengthwise there is a more pronounced variation. A summary of the test article center location and average heat flux over the exposed surface is shown in Table 10. For all further analysis and results, the heat flux values referenced will be the average incident heat flux over the exposed sample surface.

Table 10: Test Article Center Location and Average Surface Incident Flux Exposures

	Low Flux (kW/m^2)		High Flux (kW/m^2)	
Test Article	Center	Average	Center	Average
Short	1.37	1.33	2.42	2.49
Long	1.45	1.34	2.75	2.54

3.6.1b Compression Test Parameters

Initially, load control tests with a loading rate of 50 N/s were performed on all samples with a 6.35 mm core thickness (Table B1). After processing the results of this initial test series, it was observed that the buckling failure in a load control test occurred so rapidly that the influence of the debonded region could not be measured. To remedy this, all further tests on samples with the 12.7 mm thick core (Table B1) were tested in displacement control at a rate of 1.25 mm/min. This allowed the effect of the debond region during the compressive loading to be observed in a controlled manner. A general outline of the test procedure is given below and is the same for both displacement and load control.

1) Place sample between lower grips (Figure 22) and secure snugly without tightening bolts used to provide the gripping force.

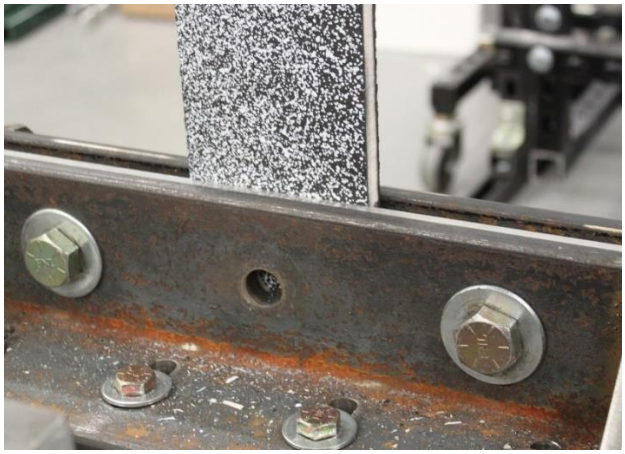

Fig. 22. Grip fixture with tightening bolts shown.

2) Record image of unexposed sample surface using 3D-DIC system. All further strains are calculated with respect to this initial ungripped/unloaded sample. Provides additional insight into the initial imperfections present (Figure 23)

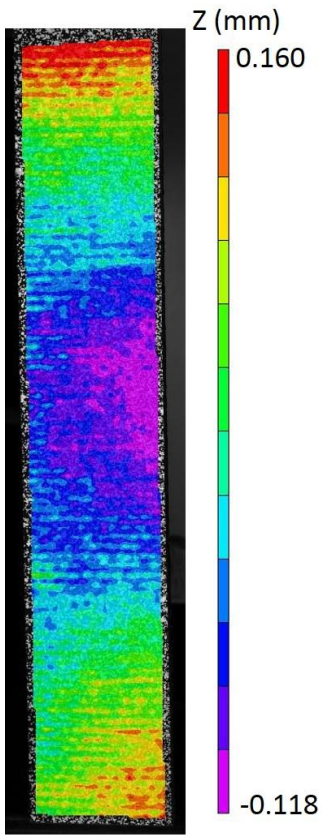

Fig. 23. Initial shape of ungripped and unloaded sample.

3) Fully grip lower region of sample by tightening ½-10 grade 9 bolts to 36 ft-lb.

4) Lower upper crosshead until a 100 N compressive load is applied to the sample.

5) Grip upper region of sample by tightening ½-10 grade 9 bolts to 36 ft-lb.

6) Return load to approximately 0 N.

7) Take second image using 3D-DIC of the fully gripped but unloaded sample.

8) Slide heater assembly into position with temperature setting corresponding to the desired incident flux on the sample surface.

9) Observe temperatures on the unexposed side and wait until steady-state is reached taking approximately 15-20 min.

10) Initiate all test measurement instruments to begin recording data.

11) Begin either the displacement control at 1.25 mm/min or load control at 50 N/s.

12) Stop test and all measurement instruments when sample experiences a sudden out-of-plane displacement and a sudden drop in the load.

3.6.1c Test Instrumentation

Due to the inhomogeneous nature of the balsa core material, single point measurements of deformation and temperature may not provide a complete description of the compressive failure response of the specimens. Instead displacement/strain full field data was obtained by use of a two CCD camera, 3D-DIC system (Correlated Solutions, Columbia, SC). Each DIC camera has a resolution of 4008 x 2672 with a maximum frames rate of 5 fps. This will enable the measurement of both the in-and out-of-plane displacements and subsequent strains on the unexposed facesheet surface. In addition to this, a FLIR SC655 thermographic camera (640 x 480, 7.5 – 13 μm) was used to observe the unexposed facesheet surface temperatures. This was spatially combined with the 3D-DIC system using the technique developed by Cholewa *et al*. [47] so that temperature data can be mapped with the corresponding deformation data at each point on the surface. Exposed facesheet surface temperatures were measured by use of a second FLIR SC655 thermographic camera located approximately 50° off the normal to the sample surface. An overview of the test setup showing the test instrumentation is given in Figure 24.

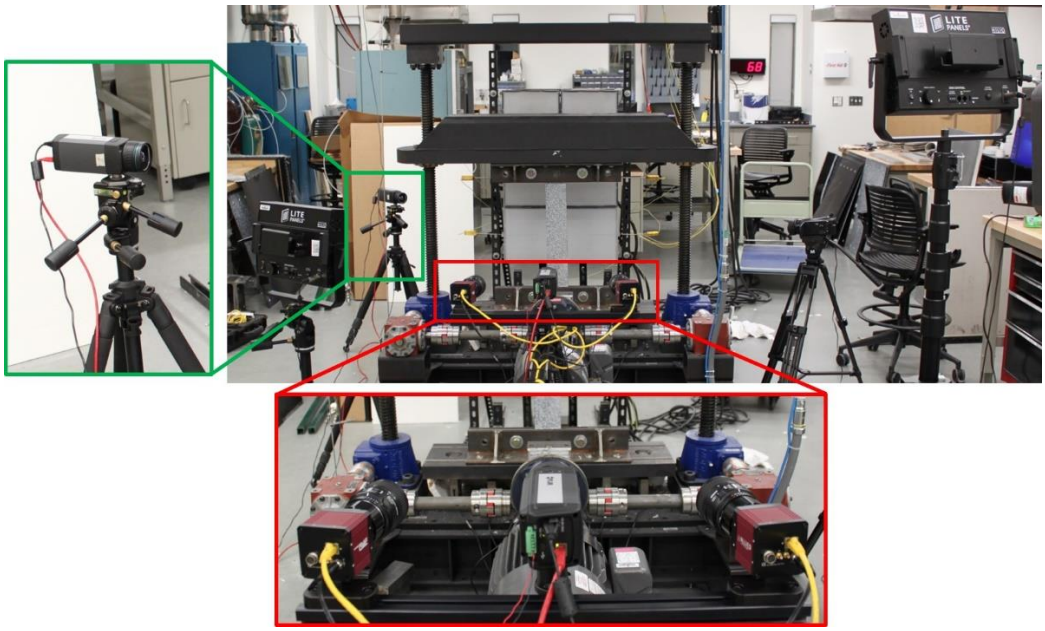

Fig. 24. Overview of the entire test setup. Red box highlights the FLIR SC655 thermographic camera (center) surrounded by the two Allied GE4000 CCD cameras used for the 3D-DIC. Green box shows the second FLIR SC655 camera recording temperatures on the exposed side of the test article.

All samples were speckled using a Rust-Oleum matte black paint base and Rust-Oleum matte white speckles previously used in Cholewa *et al*. [47] for high temperature testing of sandwich composites. Emissivity of this paint was characterized in Cholewa *et al*. [47] and shown to be approximately 0.95 at 100°C. All tests were recorded at 2.2 fps and post-processing was done in Vic3D-7 (Correlated Solutions) using a subset size of 29 pixels and step size of 7 pixels using a normalized squared differences correlation function. A description of the theoretical background of DIC and the definitions of the parameters and correlation functions can be found in [48–51].

Chapter 4: Results

4.1 Introduction

Mode I and II fracture tests were performed on the E-glass/epoxy, balsa wood core sandwich composite to analyze the debond process on the interface between the facesheet and core. These tests showed that damage to the balsa core often occurs before interfacial debonding. This becomes more likely as the interface temperature is increased. Column buckling tests with one face of the sandwich composite exposed to an incident flux were then performed to observe what effect the weakened interfacial toughness has on the buckling response. Measurements were taken using a thermographic camera linked with a two camera optical 3D-DIC system. This allowed a mapping of the unexposed side temperatures with the displacement/strain data from the DIC system.

In addition to the relatively small size scale of the Mode I and II fracture tests, large test articles were manufactured so that column buckling could be investigated. These samples varied in both length and core thickness along with some samples containing a thin film between the unexposed facesheet and balsa core to create an artificial debond. These test articles were tested at room temperature and two levels of a one-sided incident flux to simulate a fire on one side of a structure. Similar to the fracture tests performed, the role of the balsa core damage was pronounced and was often the triggering mechanism for a global buckling failure of the column. At higher flux levels resulting in higher facesheet temperatures, facesheet damage in the form of wrinkling was the primary damage mechanism which initiated the global failure of the column.

4.2 Mode I Fracture Toughness

Samples were tested at temperatures from ambient, 60°C, 80°C, and 100°C in the DCB setup shown in Figure 15 Dimensions for each sample were measured in five locations along the length prior to testing and given in Table B1. For all high temperature tests screws were used to connect the piano hinge to the facesheet surface to mitigate deformation of the hinge itself. While this was an improvement over the use of epoxy adhesive, slight bending of the hinge was observed. Room temperature tests exhibited stable crack growth along the interfacial plane with little to no crack-kinking or balsa core damage. High-temperature tests showed a somewhat stable crack growth but damage to the balsa core was observed and became worse as the temperature increased. This

damage manifested itself as either small segments of the core pulling out of the surrounding material or crack-kinking. If crack-kinking was observed the test was stopped and the sample removed. The MBT method was used to calculate the strain energy release rate for all Mode I DCB tests.

4.2.1 Ambient Temperature Results

Load-displacement curves (Figure 25a-b) for all room-temperature tests exhibit the typical stair step pattern seen with stable crack propagation. All cracks were allowed to grow until just prior to the crack/length ratio, *a/L*, of 0.5. This was shown in [5] to avoid nonlinear specimen end effects affecting the G_{Ic}.

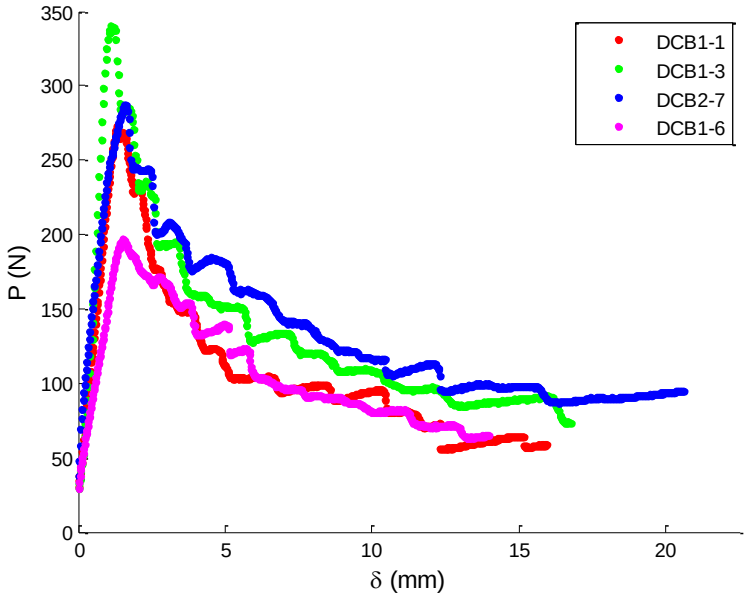

(a)

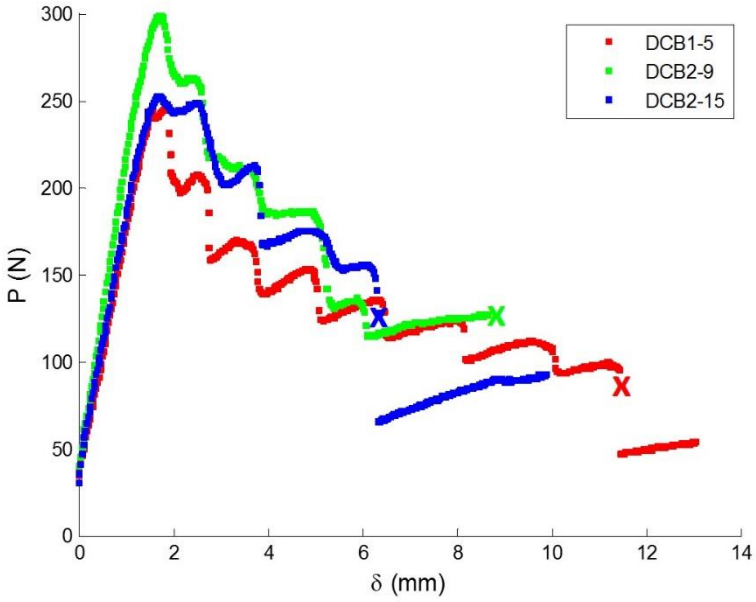

(b)

Fig. 25. Load-displacement curves for all room-temperature DCB tests. (a) Stable crack growth observed with no kinking. (b) Stable crack growth occurs until balsa core kinks marked with (X) on plot.

Note that points where kinking occurred have been identified in the previous plot (Figure 25b) and all data past these points were not used in the MBT G_{Ic} calculation, shown below in Equation (17) for reference.

$$G_{Ic} = \frac{3P\delta}{2b(a + |\Delta|)} \tag{17}$$

Small amounts of core damage were observed to occur primarily within two regions along the interface. First, the area adjacent to the Kapton® film insert exhibited a small region of balsa wood separation spanning the width of the sample, shown in Figure 26a. This appeared more often in the high temperature tests and the Mode II CSB tests. The second region was near the midpoint of the sample ($a/L \approx 0.5$) where either crack-kinking occurred, or a small amounts of core separation, as shown in Figure 26a-b. For the first case, results for Equation (17) are valid only after the damaged region fully separates from the surrounding core material. In the second case, small amounts of separation will affect the apparent G_{Ic} value while crack-kinking prohibits any valid data from being taken.

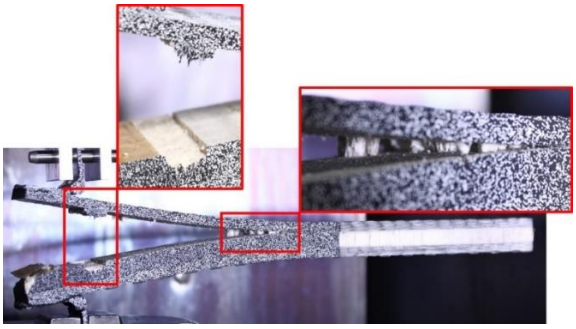

(a)

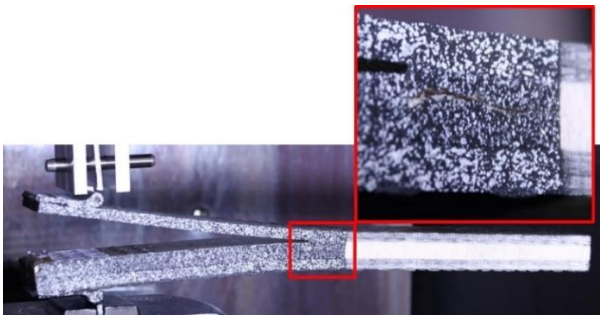

(b)

Fig. 26. Examples of balsa core damage present in DCB tests. (a) Separation of a small region of the balsa core occurred at the edge of the Kapton® film in addition to small pockets of the core separating near the mid-length of the sample. (b) Crack-kinking occurring predominantly towards mid-length of DCB sample.

Using the MBT Equation (17) described previously requires the cube root of the compliance, $C^{1/3}$, plotted against the crack length, a. An example of this is shown in Figure 27 for one of the room temperature tests and a least squares line fit to the data is used to find the x-intercept.

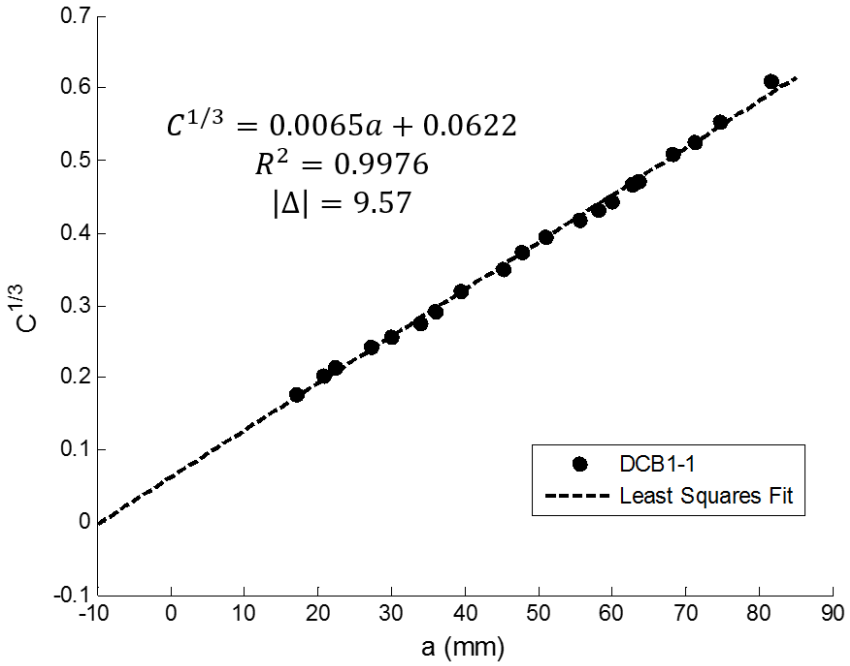

Fig. 27. Additional parameter in MBT equation (17), Δ, determined from the x-intercept of the above plot.

The Mode I fracture toughness can be solved as a function of crack length with results from all room temperature tests shown in Figure 28. Averaging over all values gives a Mode I fracture toughness of 858 ± 134 J/m^2.

A comparison of this to other works with similar material systems but different test, sample geometry, and data reduction methods show good agreement. Shivakumar and Smith [4] used a BALTEK D-grade end grain balsa core with glass/vinyl-ester facesheets for a DCB test similar to the one in this work. They obtained fracture toughness values of 693 ± 243 J/m^2 and 1008 ± 262 J/m^2 for core densities of 100 and 150 kg/m^3. In addition, they also mentioned significant crack-kinking occurring that coincided with the boundary between two segments of the balsa core. Cantwell and Davies [13, 14] used a single cantilever beam (SCB) test for the Mode I fracture toughness of a balsa core with a stitched quadriaxial E-glass/polyester facesheets. Using the compliance calibration (CC) method they obtained fracture toughness values of 360-500 J/m^2 and 1320 J/m^2 for balsa core densities of 100 and 175 kg/m^3 respectively.

One reason a difference may exist between the fracture toughness obtained in this work (858 ± 134 J/m^2) and by Shivakumar and Smith [4] (1008 ± 262 J/m^2) for a similar balsa core density is that no modification was made to their test samples neutral axis location. Because they used a symmetric sandwich composite test sample whose neutral axis does not coincide with the interfacial plane, significant peel and shear stresses can develop at the crack-front. This causes the total fracture toughness, G_c, to increase due to the introduction of a higher Mode II component, G_{II}. Because the present results were obtained using a geometry in which the neutral axis coincides with the interfacial plane, crack propagation occurs primarily due to the lower energy state Mode I component and not an interaction among the remaining sliding and tearing modes.

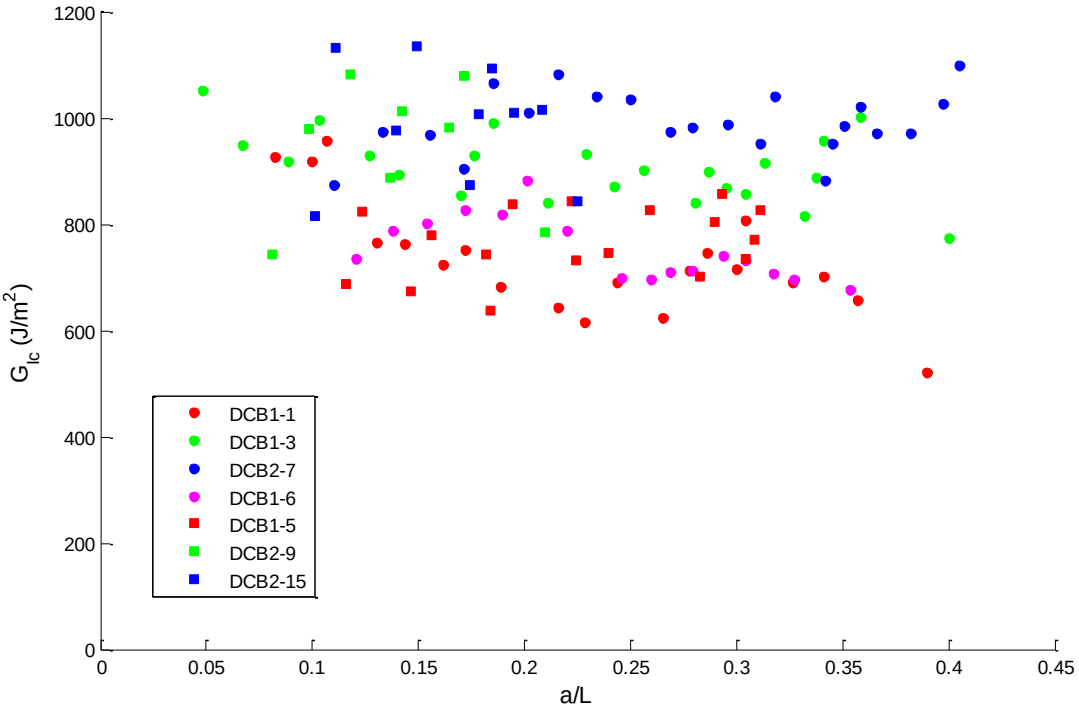

Fig. 28. Mode I energy release rate using MBT for room-temperature DCB tests. Average value is 858 J/m^2 with a standard deviation of 134 J/m^2.

4.2.2 Mode Mixity

To determine the mode mixity of the DCB test using a modified facesheet layup, the modified VCCT [52] was employed utilizing a commercial finite element package NX 8.5 along with the Nastran solver. The mesh around the crack-tip region consisted of eight-node solid elements (CHEXA8) while away from the crack-tip 4-node tetrahedral elements (CTETRA4) were used.

The mesh regions on either side of the interfacial surface have separate but coincident nodes. The FE mesh along with pertinent dimensions is shown in Figure 29a-c.

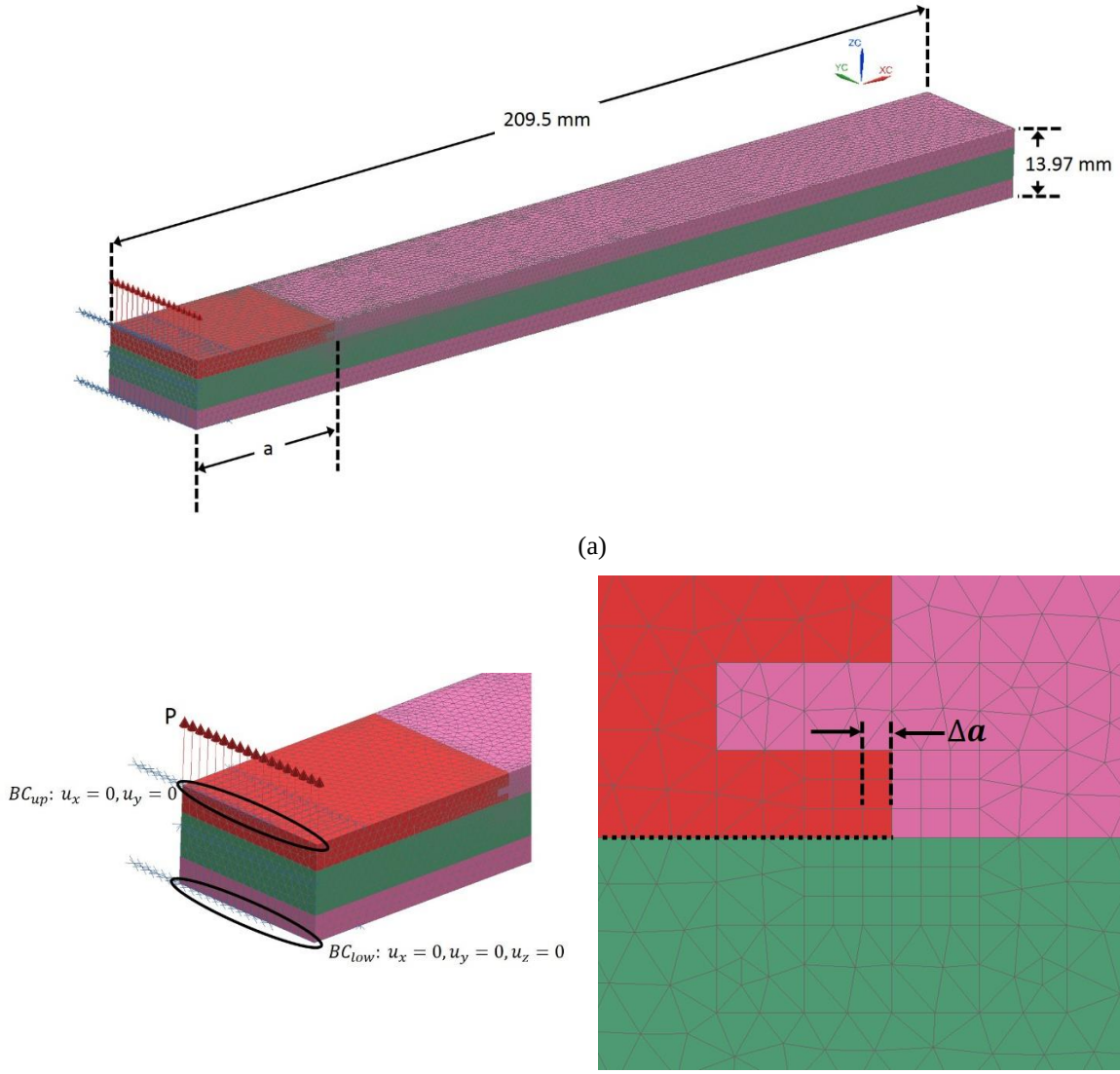

Fig. 29. (a) Overview of the FE mesh of the DCB sample with crack length a. (b) Location and type of boundary conditions and loading applied. (c) Crack defined as horizontal dotted line, crack closure length, Δa, centered about the crack-tip.

Since the system represented in the FE analysis is bimaterial along the interfacial plane, additional considerations must be taken into account to evaluate the G_I, G_{II}, and G_{III} components. These considerations are a result of the mathematical solutions [53] showing that the stresses in the vicinity of the crack-tip oscillate resulting in an undefined mixed mode ratio as the crack closure

length, Δa, goes to zero. It has been shown [52] that the use of larger values of $\Delta a/a$ yields an almost stationary total energy release rate component, G_T. The conclusion formed is that one must choose the element length, Δa, small enough to obtain a converged solution but large enough to avoid oscillating results.

An initial investigation was performed using an FE model with a 135 N load and a crack length, a, of 35 mm to determine the optimal ratio $\Delta a/a$. Crack closure lengths, Δa, were varied and the individual mode mixity and total energy release rate results shown in Table 11 along with a plot of G_T as a function of Δa in Figure 30.

Table 11: Determination of Optimal Crack Closure Element Length Ratio for 35 mm Crack

Δa (mm)	$\Delta a/a$	G_I/G_T (%)	G_{II}/G_T (%)	G_{III}/G_T (%)	G_T (J/m^2)
0.500	0.0143	86.2	12.4	1.42	823.6
0.400	**0.0114**	**85.2**	**13.4**	**1.36**	**847.5**
0.330	0.0094	84.0	14.6	1.36	856.7
0.250	0.0071	82.2	16.4	1.37	847.7
0.200	0.0057	80.5	18.1	1.37	853.8
0.143	0.0041	78.2	20.4	1.35	860.3
0.100	0.0028	75.4	23.2	1.36	866.2

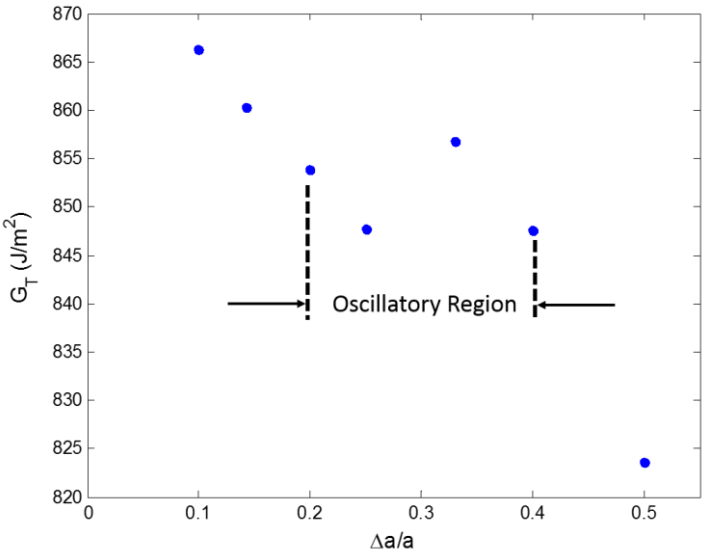

Fig. 30. Total energy release rate as a function of the crack closure length, Δa, for a crack length of 35 mm.

For all further FE analysis using the VCCT, a crack closure ratio of 0.01 was used for the elements surrounding the crack-tip. A summary of the three mode-mixity components given in Table 12 show that as the crack length increases the Mode I component increases from 80.3% to 85.2% while Mode II decreases from 18.9% to 13.0%. This shows that the modified facesheet layup method used creates a Mode I-dominant DCB specimen.

Table 12: DCB Mode Mixity

a (mm)	Δa (mm)	G_I/G_T (%)	G_{II}/G_T (%)	G_{III}/G_T (%)
10	0.1	80.3	18.9	0.80
20	0.2	82.7	16.2	1.11
30	0.3	84.3	14.4	1.24
40	0.4	85.0	13.5	1.42
50	0.5	85.4	13.1	1.54
60	0.6	85.2	13.0	1.80

4.2.3 High Temperature Results

Damage to the balsa core was present in each of the high temperature tests with increasing amounts of damage as the temperature increased. This damage takes the form of either small segments of

the core separating from the surrounding material or a crack-kink forming. Unlike the previous room temperature tests, the damage was not localized to any distinct regions of the interfacial plane and no sample came close to reaching the middle of the DCB sample. Facesheet wrinkling was observed on the surface of the upper beam during the 100°C test and may have been caused by the temperature degradation of the woven laminate combined with the compressive loading of the outer most ply. Load-displacement curves are shown in Figure 31 for all high temperature DCB tests.

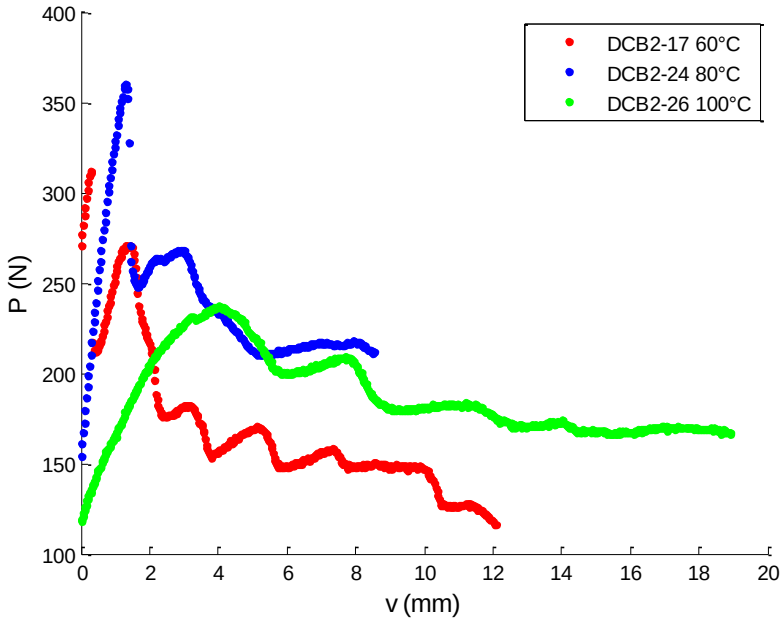

Fig. 31. Load-displacement curves for all high-temperature DCB tests.

Note in the above that the stair-step pattern seen in the room temperature tests is not as evident past 60°C and the curves themselves decrease at a smaller rate than at room temperature. In addition to this the linear portion prior to the max load was distorted due to the screws maintaining attachment until a sudden pull out of the core. The increased amount of non-kinking core damage along with wrinkling at 100°C adds to the amount of energy required to extend the crack a small increment. This shows itself as an increase in the apparent Mode I fracture toughness by Equation (17) as it is made up of both the energy to extend a crack by an incremental amount and the energy to create the core/facesheet damage. The Mode I fracture toughness for each temperature tested is shown in Figure 32 as a function of the crack length. Note how, unlike the room temperature data (Figure 28), the fracture toughness increases as the crack grows in length.

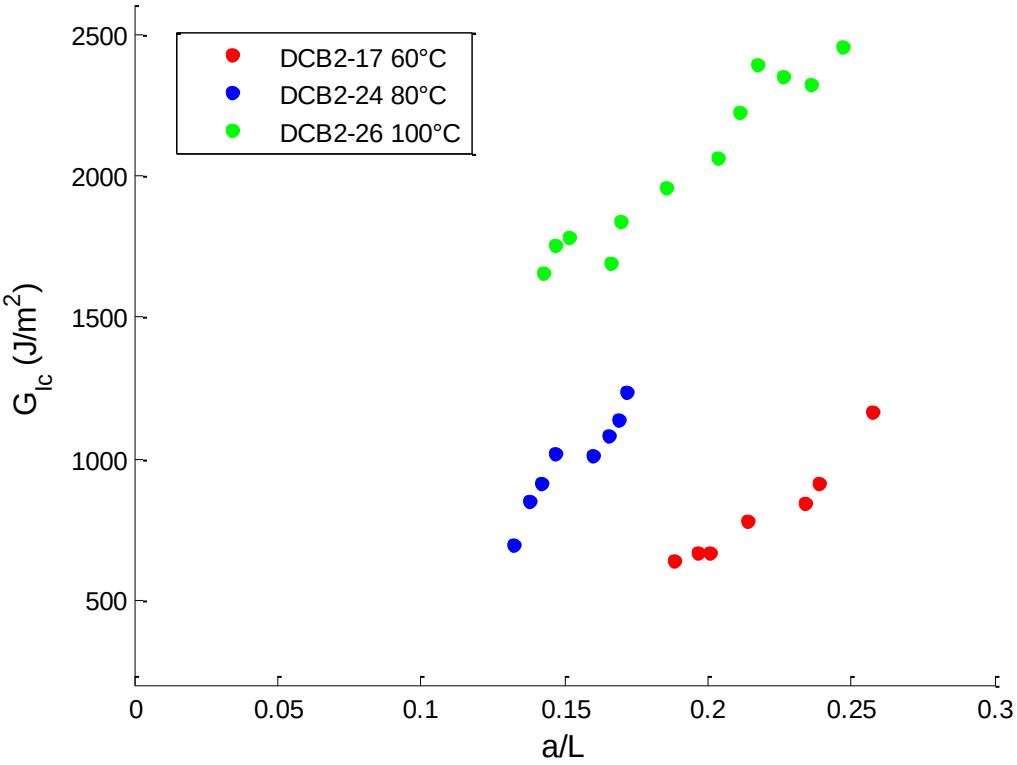

Fig. 32. Fracture toughness increases with increasing crack length, a, unlike what was observed in the room temperature tests.

This increase in fracture toughness can most likely be attributed to the damage occurring as the crack propagates along the interfacial plane. While it was shown in Table 12 that, as the crack extends the Mode I mixity also increases, the incorporation of the damage skews the results to extremely large values. Temperature dependent Mode I fracture toughness values reported will be the minimum values shown in Figure 32 for each temperature tested above ambient so as to avoid as much as possible the effects of the damage observed. These values are shown in Figure 33 along with images of the types of damage observed (Figure 34).

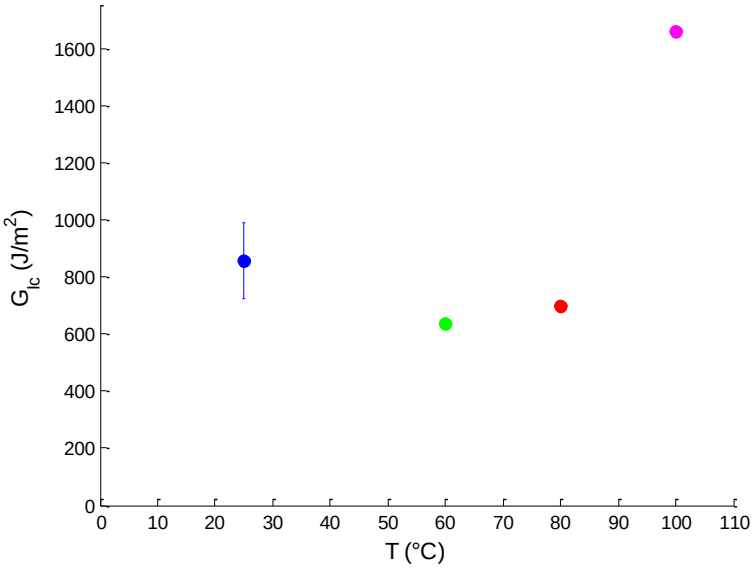

Fig. 33. Temperature dependent fracture toughness curves.

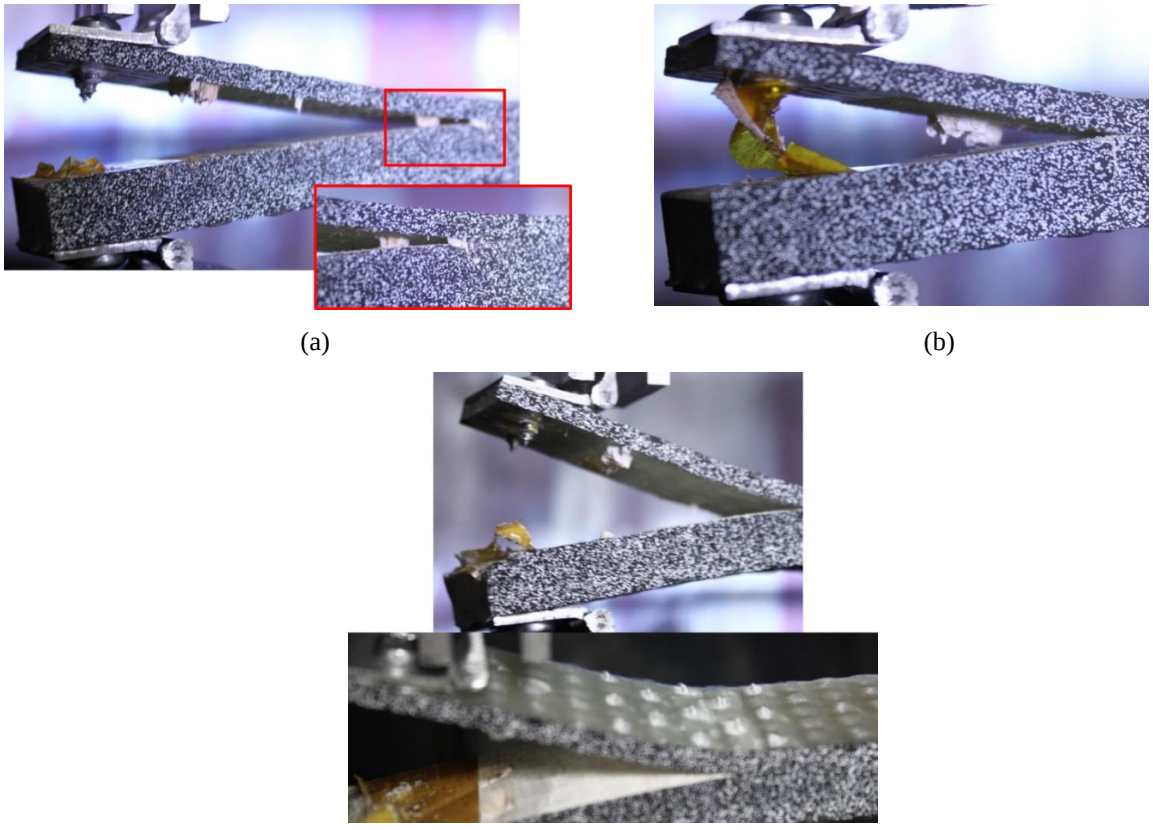

(a) (b)

(c)

Fig. 34. High temperature DCB test damage. (a-b) Core separation and kinking observed for the 60°C and 80°C tests. (c) Some core separation and face wrinkling observed for the 100°C DCB test.

While a comparison to other work would be valuable to see if the same degree of core damage was observed, to date no work can be found for high temperature fracture toughness of a sandwich composite with a balsa wood core. The only similar work by Liechti and Marton [9] used a titanium honeycomb core with IM7/PETI-5 faceplates but due to the specific core material used, kinking and core separation were not encountered in their tests.

4.3 Mode II Fracture Toughness

Sample dimensions for Mode II CSB tests are given in Table A1 and all tests had the debond region initially opened with a steel wedge (Figure 14). Similar to the DCB tests, significant core separation damage was observed located near the edge of the Kapton® film. This damage prevented the sliding motion between the upper and lower beam and thus increased the overall strain energy of the member. This can be seen in the load-displacement curves shown in Figure 35 where the curve begins a downward slope as expected with a propagating crack. As the separated core begins to slide into the surrounding material the curve inflects upwards as it takes a greater load to overcome this contact. This core damage is shown in Figure 36.

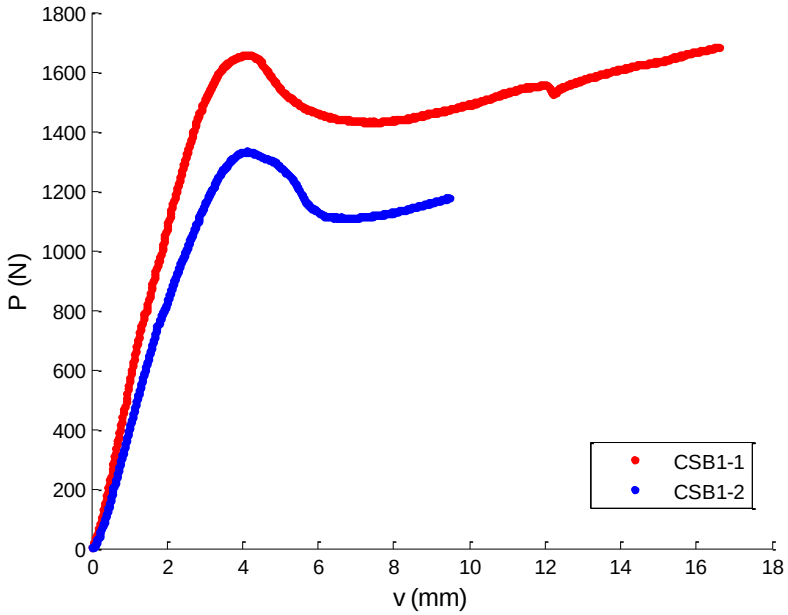

Fig. 35. Load-displacement curves for the CSB test. Increasing load due to core damage.

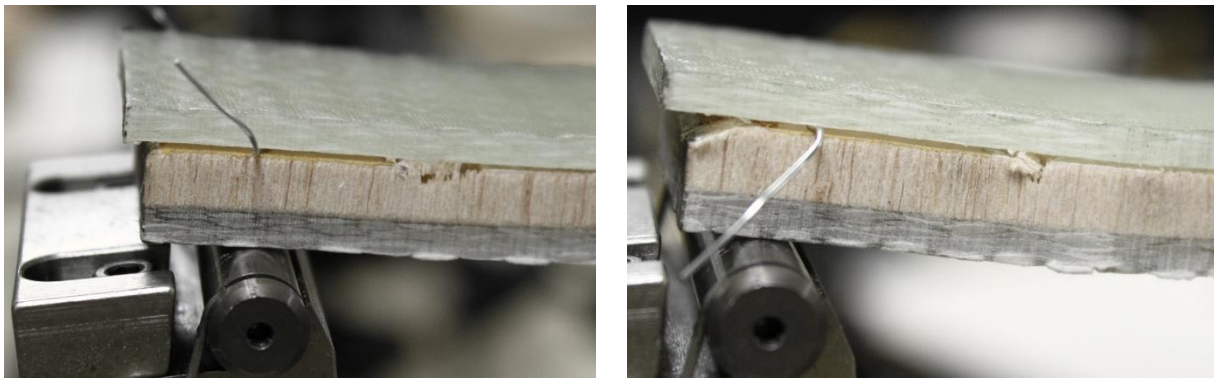

(a) (b)

Fig. 36. Core damage present in CSB tests, (a) CSB1-1, (b) CSB1-2.

This behavior was also evident when examining the Mode II fracture toughness, G_{IIc}, as a function of the crack length (Figure 37). The increase in the values shown is due to the contact force between the separated and surrounding region as the load is increased. This damage to the core prevents an accurate measurement of the Mode II fracture toughness from being obtained.

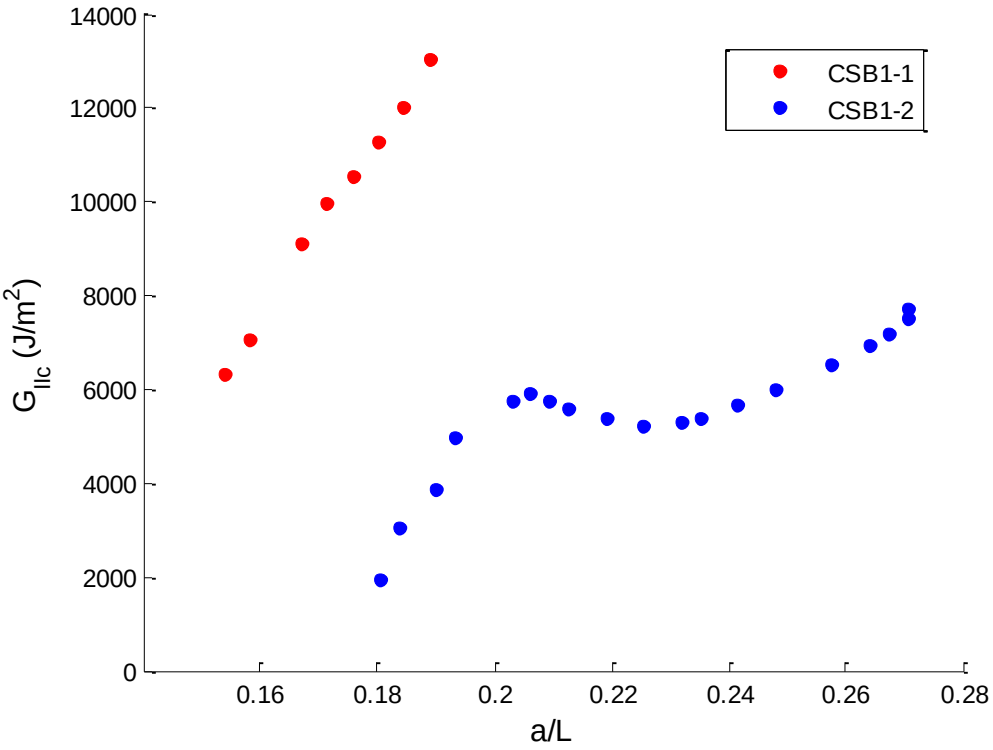

Fig. 37. Mode II fracture toughness of CSB samples. Increasing value due to core damage preventing sliding motion of the upper and lower beams in the debond region.

While small amounts of core damage did not have a large effect on the results of the ambient temperature Mode I DCB tests, due to the nature of the sliding motion in the Mode II CSB test accurate fracture toughness values could not be obtained. Previous work on the Mode II interfacial toughness is limited, Carlson [19] used a similar CSB test to determine the effects of the sample parameters (core thickness, crack length, etc.) on achieving a Mode II dominant crack growth. Using an E-glass facesheet material and balsa core with density equal to 151 kg/m^3 it was observed that using short crack lengths caused core shear failures to occur prior to crack extension similar to what was seen in the current work. A comparison value for the Mode II fracture toughness, G_{IIc}, cannot be made since Carlson [19] assumed a value in order to obtain the optimal parameters sought after. An additional note made in his work is that the balsa core material properties can vary significantly within a single sheet of the material and that these will have a large influence on the calculated fracture toughness.

4.4 Beam Buckling

4.4.1 Room Temperature Tests

Room temperature testing highlighted the influence of balsa core damage arresting crack propagation and triggering a global failure of the test article. The debonded samples first exhibited localized buckling in the debond region prior to the crack-front advancing. After this small advancement, core damage occurred at one side of the debond crack-front triggering a sudden failure of the test specimen. This failure exhibited an anti-symmetric shape profile similar to what was observed in Avery and Sankar [21]. Test articles with no debonding exhibited the usual fixed-fixed failure mode shape until core failure occurred near the gripped region where the sample tries to maintain the zero-slope condition. After this core failure, a sudden loss of load along with the sample rapidly deflecting outwards at the location of the core damage occurred.

4.4.1a Debond Buckling and Growth

Using the full-field measurement capabilities of a 3D-DIC allows the progression of debond buckling and then propagation to be observed. All debond test articles with a 12.7 mm thick core first exhibited an initial out-of-plane deflection in the debond region followed by a propagation of the crack-front. This propagation did not always occur symmetrically on both sides of the debond region but often in a greater amount on one side or the other. This caused the sample to exhibit an asymmetric overall shape with one side having a greater out-of-plane displacement than the other. By taking the vertical line profile (Figure 38) of each of the 12.7 mm core debonded samples, this progression from a purely debond buckling to a combination of buckling and propagation can be observed and is shown in Figure 39.

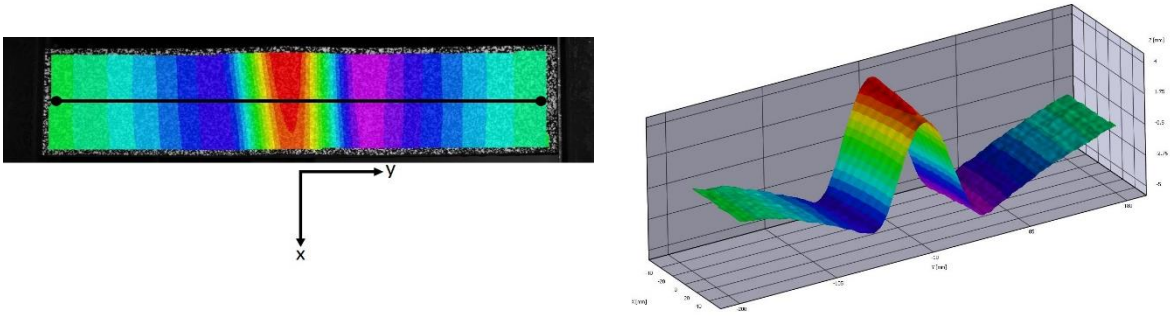

(a) (b)

Fig. 38. (a) Centerline used to obtain displacement profiles throughout loading. (b) 3D profile shape of same debond specimen.

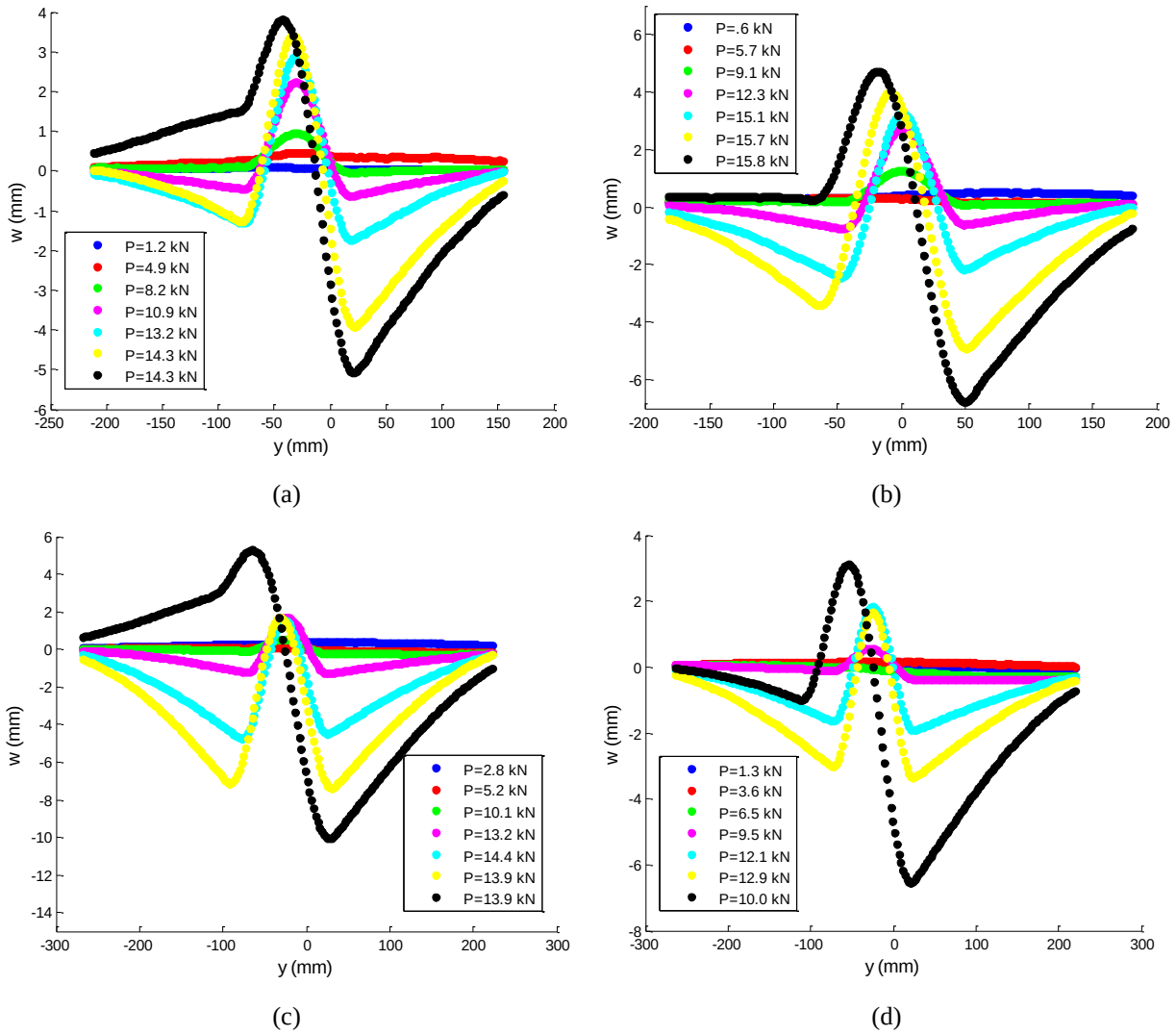

Fig. 39. Shape profiles of the 12.7 mm core samples throughout the room temperature debond buckling test. (a) Test article D4-3 (L = 585 mm), (b) D4-2 (L = 587 mm), (c) D6-2 (L = 705 mm), (d) D6-1 (L = 705 mm). Note that +y is the upper part of the sample and +w is towards the DIC cameras (and thus away from the heater panels).

Note in the previous figure the yellow and black profile lines are the moment just before and after global failure, respectively, and ”ND” refers to ”No Debond” while ”D” is ”Debond”’ as the sample naming convention. All ultimate failure loads are approximately equal due to the debond buckling load being independent of the length of the sample. The short length samples (Figure 39a-b) exhibited a slightly asymmetric out-of-plane deflection prior to failure while the long length samples (Figure 39c-d) were more symmetric just prior to failure. The asymmetry in the short length samples was most likely due to the debond propagating more on one side than the other.

This crack propagation can be viewed in greater detail if the debond region is isolated in each of the test articles shown in Figure 39. By choosing two instances from each test, one early in the test when the debond buckling is first noticed, and the other just prior to global failure, the extent of the debond propagation can be quantified. This is shown in Figure 40 where the debonds have been shifted so their peaks lie on the same vertical line. The amount of propagation, Δa, is also shown relative to the original 88.9 mm debond length created by the insertion of Kapton® or PTFE sheets.

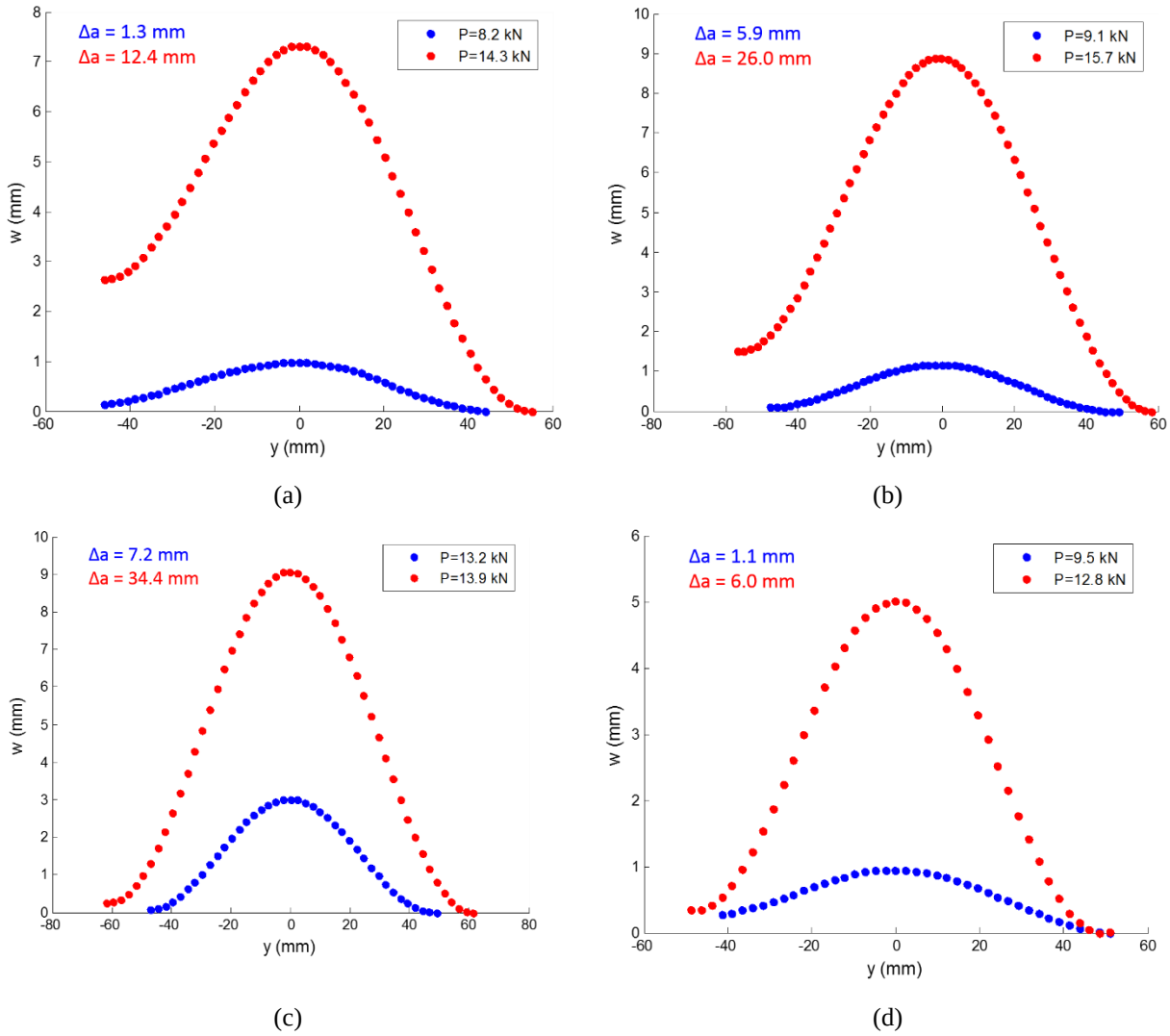

Fig. 40. Debond profiles showing propagation at two instances of the buckling test. (a) Test article D4-3 (L = 585 mm), (b) D4-2 (L = 587 mm), (c) D6-2 (L = 705 mm), (d) D6-1 (L = 705 mm).

After growth of the debond by an amount Δa, the core experiences a sudden failure at one of the crack-fronts of the debond region. This results in a sudden failure of the test article exhibiting the anti-symmetric shape shown in Figure 41.

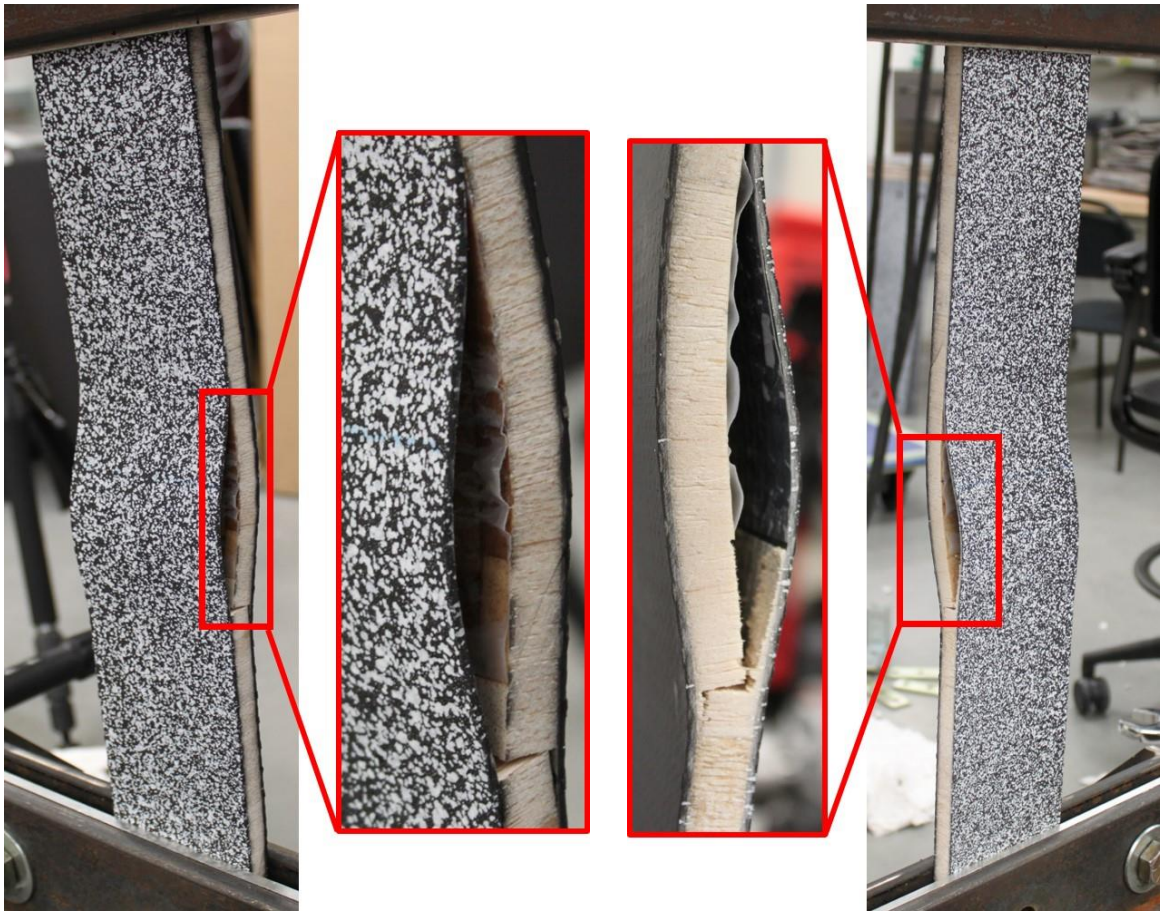

(a) (b)

Fig. 41. Balsa core damage at crack-front leads to asymmetric failure shape. (a) Test article D4-2 (L = 587 mm), (b) D6-2 (L = 705 mm).

While all test articles using a 12.7 mm thick core exhibited debond buckling and then some amount of propagation, this series of events was not observed to occur in any sample with a 6.35 mm thick core. Instead the test articles failed in a similar anti-symmetric shape as their thicker core counterparts (Figure 39) without the influence of the debond buckling and propagating. Several reasons exist as to why these thinner core samples did not have the same failure process as observed previously. The first is that the two Kapton® sheets used to create the debond may have allowed the epoxy to adhere to the surface more than the PTFE. If so, then there is no longer a true

debond between the facesheet and core but instead a weakened interface that may have required additional load to first separate before buckling could be observed. A second reason may be that a small amount of misalignment, either in the load or a sample imperfection, could have existed and its influence was magnified with the thinner core test articles. A summary of the out-of-plane displacement profiles is shown below in Figure 42 where again the yellow and black profiles are just before and after global failure respectively.

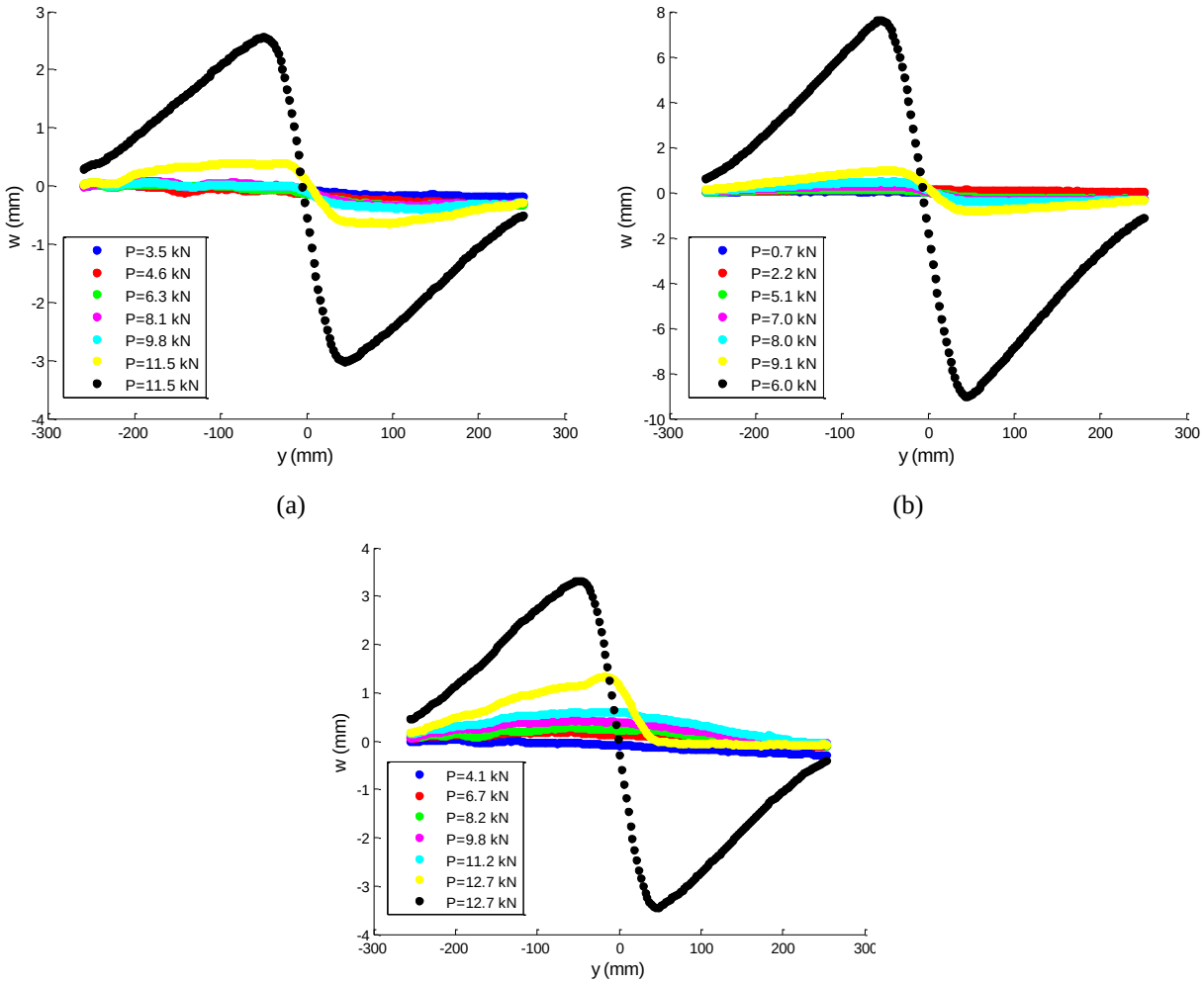

Fig. 42. Shape profiles of the 6.35 mm core samples throughout the room temperature debond buckling test. (a) Test article D1-2 (L = 740 mm), (b) D1-4 (L = 740 mm), (c) D2-2 (L = 736 mm). Note that +y is the upper part of the sample and +w is towards the DIC cameras (and thus away from the heater panels).

4.4.1b No Debond Global Failure

Test articles with no debond exhibited the typical fixed-fixed failure mode prior to total collapse regardless of core thickness. The total collapse was initiated by the core failure near the grips where the zero slope condition is required. At this point the failed region acts like a pivot and the sample experiences a sudden reduction of load combined with large out-of-plane displacements. The out-of-plane displacement shape profiles of both the 6.35 mm core (Figure 43) and 12.7 mm core (Figure 44) are shown below with the yellow and black profile lines as the moment just before and after global failure respectively.

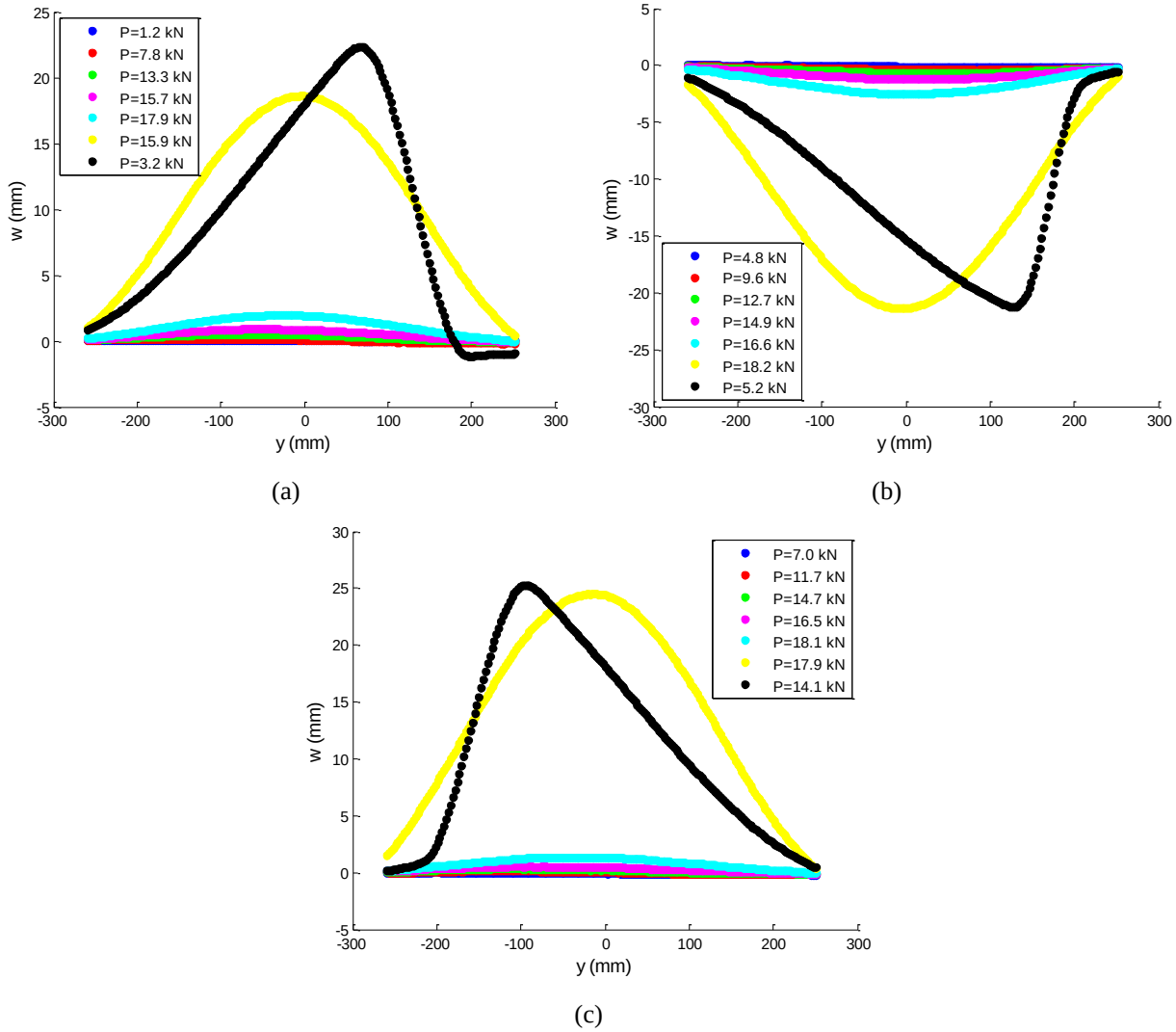

Fig. 43. Displacement profiles for 6.35 mm core thickness test articles with length of 740 mm and no debond. (a) Test article ND1-2, (b) ND1-3, (c) ND2-1. Note that +y is the upper part of the sample and +w is towards the DIC cameras (and thus away from the heater panels).

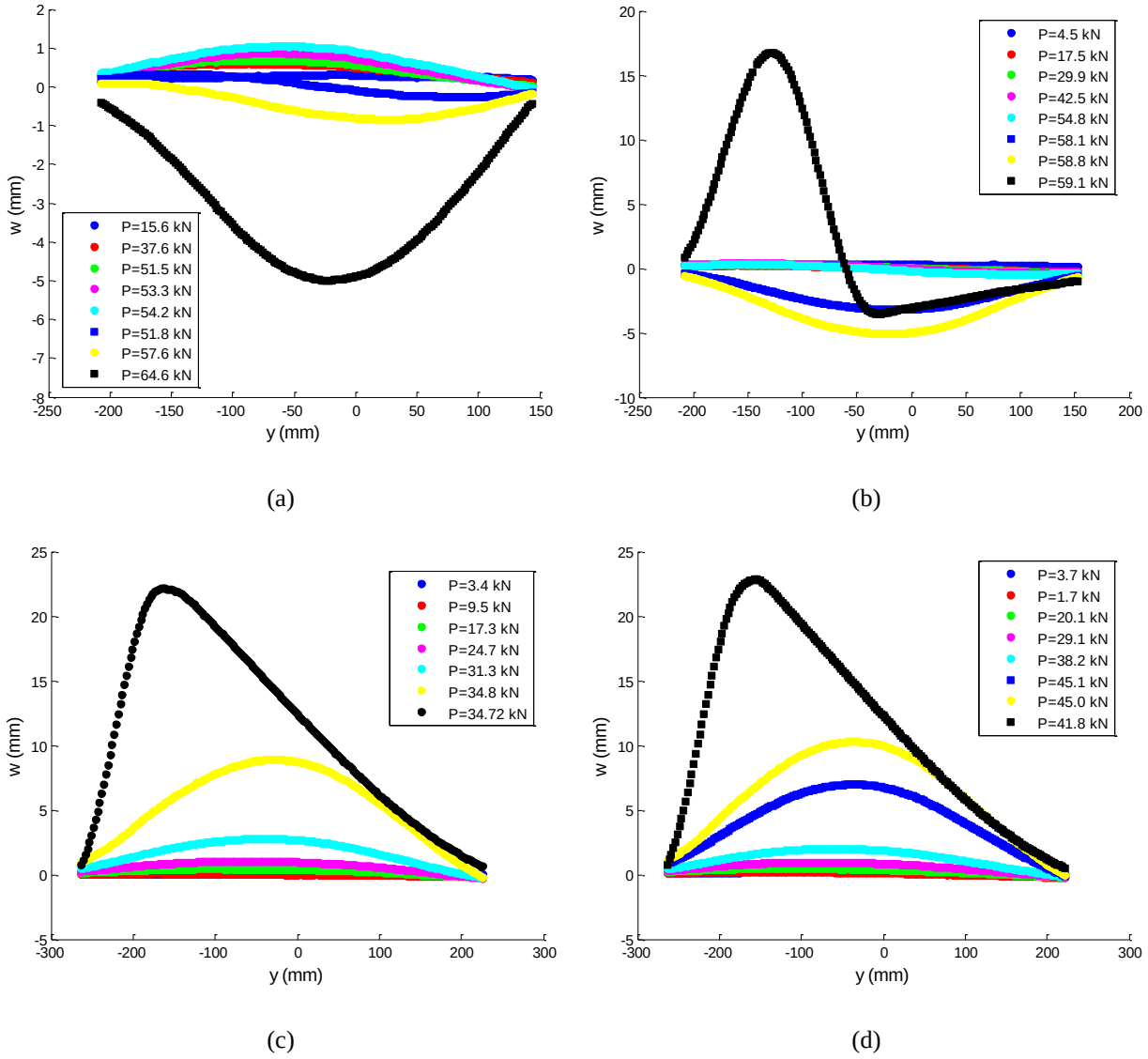

Fig. 44. Displacement profiles for 12.7 mm core thickness test articles with no debond. (a) Test article ND4-1 (L = 584 mm), (b) ND4-4 (L = 583 mm), (c) ND7-6 (L = 709 mm), (d) ND7-3 (L = 708 mm). Note that +y is the upper part of the sample and +w is towards the DIC cameras (and thus away from the heater panels).

During the testing of the short 12.7 mm core samples (Figure 44a-b), several abrupt noises could be heard throughout the test. However, no core damage or significant out-of-plane displacement was observed. This behavior is reflected in the load-displacement curves (Figure 45) for this series of tests where a sudden drop of the load is seen for test articles ND4-1 and ND4-4 after which the load increases.

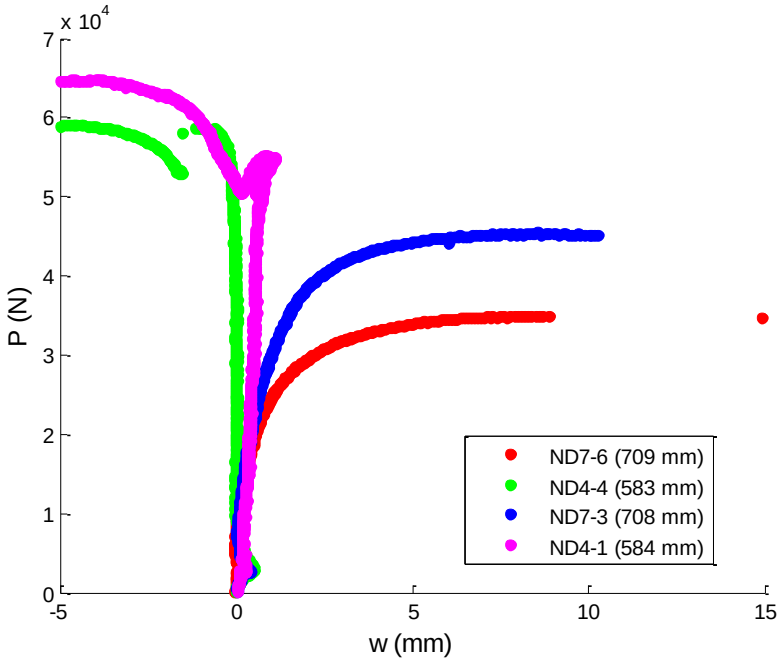

Fig. 45. Load-displacement curves for test articles with no debond present.

Since previous tests indicate that if the sounds had been a core failure then sudden global failure would be expected, the next possibilities are either a delamination between plies of the facesheets or localized debonding. Closer inspection of the DIC test results for ND4-1 and ND4-4 yielded no additional information as to the possible damage. This damage may have occurred on the exposed facesheet side and not viewable using the DIC measurements. For these short length test articles global failure occurred suddenly by a core failure near the gripped region leading to debonding of the facesheets from the core. The difference though from the longer length samples was that ND4-1 failed near both gripped regions at the same time (Figure 46a) and ND4-4 opened suddenly near the lower grip (Figure 46b) with a rapid debond of both facesheets until one side reached the lower grip, and the other was arrested by further core damage. All longer length test articles failed in the same manner (Figure 46c) with the core failure occurring near one of the gripped regions and then slight debonding on both sides of the core.

(a) (b) (c)

Fig. 46. Global failure modes observed for test articles with no debond. (a) ND4-1 (L = 584 mm), (b) ND4-4 (L = 582 mm), (c) ND7-6 (L = 709 mm).

4.4.2 Low Flux Tests

Test articles exposed to the lower flux level of 1.33 kW/m^2 experienced similar failure processes as the room temperature tests. Small differences were observed for both samples containing a debond and those that did not. Debond buckling and propagation, while still observed, occurred to a far lesser extent both in terms of out-of-plane displacement of the debond region, and length of crack propagation then was seen in the room temperature testing. The ultimate failure was still triggered by core failure at the crack-front leading to the same asymmetric shape profile as was seen in the room temperature results (Figure 41). Test articles with no debond also exhibited the same out-of-plane displacement profile as the compressive load was increased as the room temperature tests. Unlike what was observed at room temperature, core failure did not always occur near the gripped region but instead damage to the facesheets was also observed and triggered the ultimate failure of the sample. A detailed description of the aforementioned observations will be shown in the following sections.

4.4.2a Temperature Profiles

The combination of the spatially varying incident flux over the length of the test articles (Figure 21) and inhomogeneous nature of the balsa core material resulted in difficulties in obtaining a uniform temperature on either facesheet. This is shown in the temperature plots on the exposed side where even though each sample type was exposed to the same incident flux, variations in the thermal properties (primarily the conductivity) lead to different temperature surface profiles for each sample. A small subset of these exposed side temperatures is shown in Figure 47 to highlight the variability between test articles, the remaining temperature fields of all test articles are shown in Appendix C.

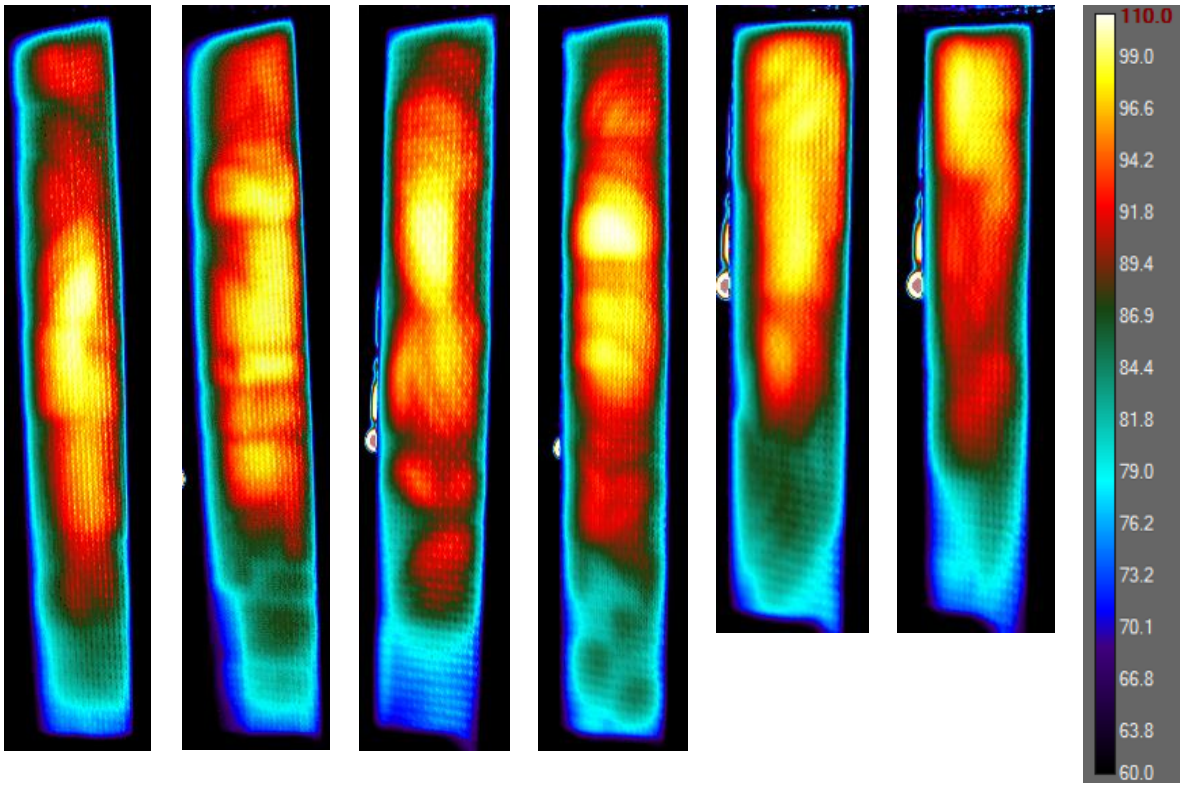

(a) (b) (c) (d) (e) (f)

Fig. 47. Temperature (°C) of exposed side from low incident heat flux exposure. (a) ND1-4 (L = 737 mm), (b) D1-1 (L = 740 mm), (c) ND7-1 (L = 705 mm), (d) D6-4 (L = 711 mm), (e) ND5-1 (L = 586 mm), (f) D3-4 (L = 584 mm).

This variability of facesheet temperatures was magnified on the unexposed side of the sandwich composite. Figure 48 shows that even though the variation of the flux across the width of the

sample was minimal (Figure 21), significant temperature differences are observed in both the length and widthwise directions.

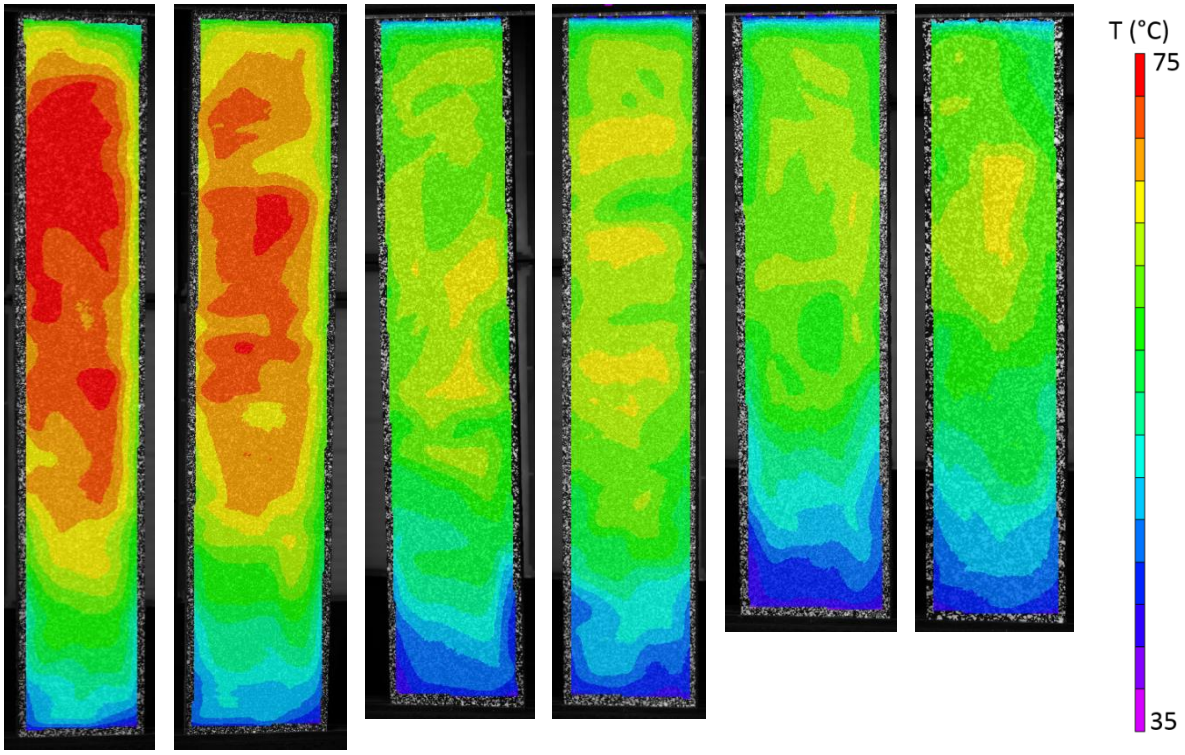

Fig. 48. Temperature (°C) of unexposed side from low incident heat flux exposure. (a) ND1-4 (L = 737 mm), (b) D1-1 (L = 740 mm), (c) ND7-1 (L = 705 mm), (d) D6-4 (L = 711 mm), (e) ND5-1 (L = 586 mm), (f) D3-4 (L = 584 mm).

By taking the vertical line profile of the temperatures similar to what was done for displacements (Figure 38) a measure of the change in temperature along the length of the sample is shown in Figure 49. This shows the significant drop in temperatures towards the lower gripped region from the reduced incident flux in this location.

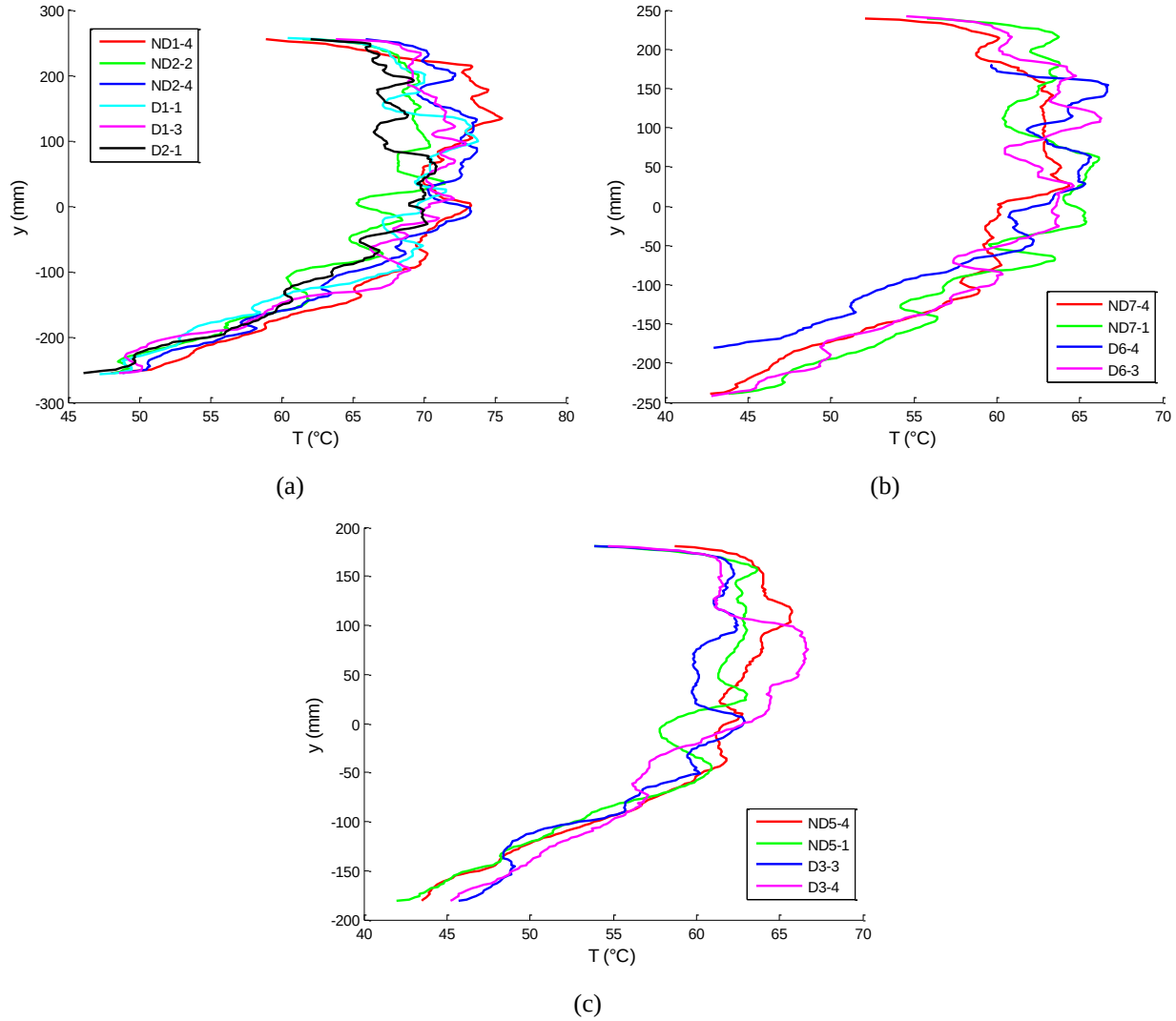

Fig. 49. Vertical temperature profile of low flux exposed test articles. (a) Core thickness of 6.35 mm, nominal length of 740 mm, (b) core thickness of 12.7 mm, nominal length of 705 mm, (c) core thickness of 12.7 mm, and nominal length of 585 mm.

4.4.2b Debond Buckling and Growth

All test articles with the 12.7 mm core thickness exhibited some amount of debond buckling and propagation. A behavior similar to the room temperature tests was observed in which this propagation did not occur equally on both crack-fronts of the debond and led to a non-symmetric shape profile immediately after failure. Core failure at one of the crack-fronts was observed, triggering a global failure of the sample in a similar manner to room temperature testing. By taking a vertical line profile, the progression from initial debond buckling to propagation and then ultimately, global failure triggered by the sudden core failure at one of the debond crack-fronts is

shown in Figure 50, where the yellow and black profile lines are the moment before and after global failure, respectively.

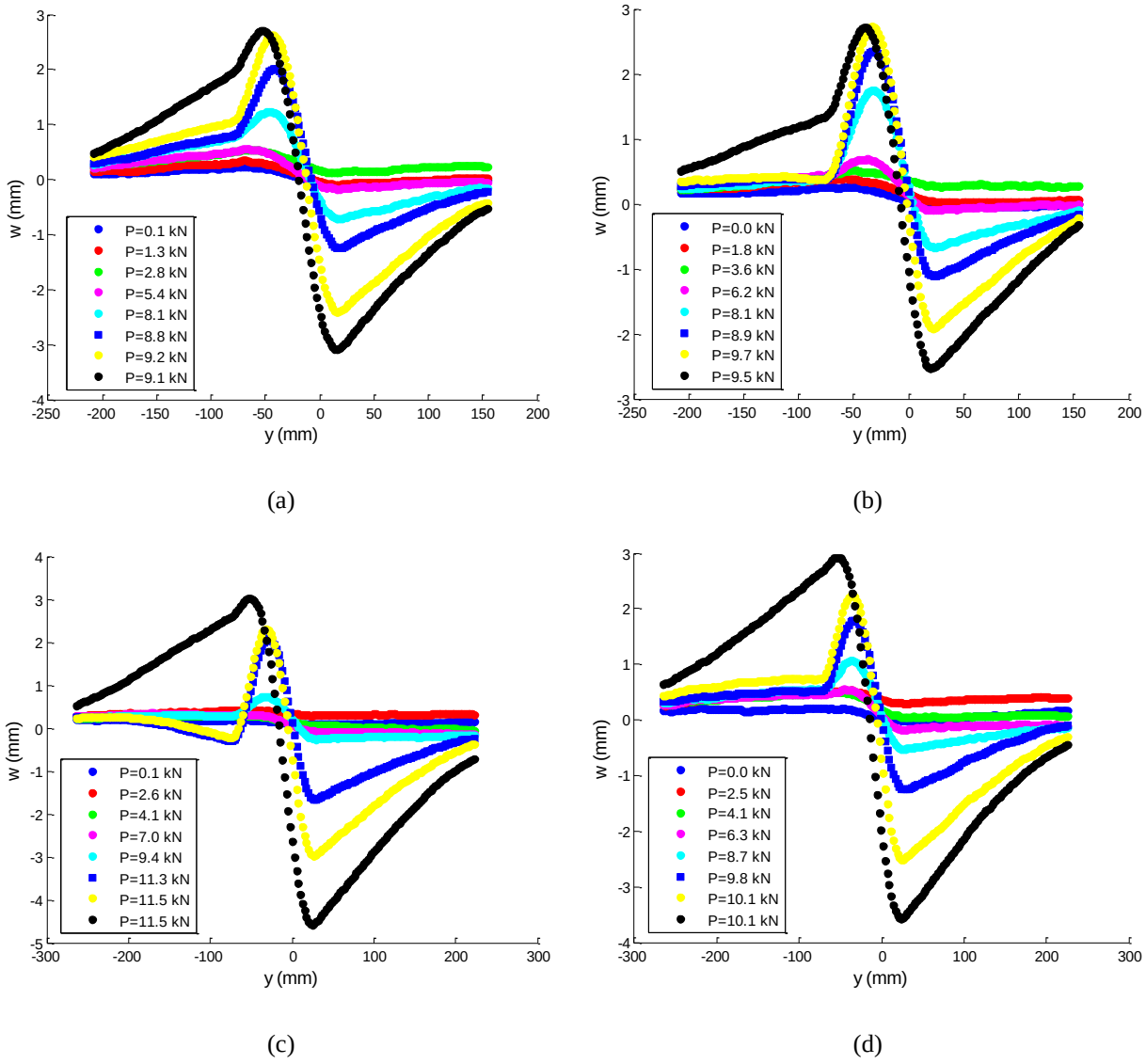

Fig. 50. Shape profiles of the 12.7 mm core samples throughout the low flux debond buckling test. (a) Test article D3-3 (L = 584 mm), (b) D3-4 (L = 584 mm), (c) D6-3 (L = 706 mm), (d) D6-4 (L = 711 mm). Note that +y is the upper part of the sample and +w is towards the DIC cameras (and thus away from the heater panels).

All test articles in the previous figure show a non-symmetrical shape profile about a vertical line through the center of the buckled debond just prior to failure (yellow line). While this was also observed for the shorter length room temperature tests (Figure 39a-b), the longer length samples exhibited greater symmetry prior to failure. A possible reason could be due to the increased

temperatures in the upper half of the test article (Figure 49) reducing the mechanical properties and shifting the neutral axis in this portion of the beam. This difference from the shift of the neutral axis between the higher and lower temperature regions of the test article could create a small moment to occur located near the central debond region and result in the asymmetric shape profiles observed. Since this behavior was also observed in the room temperature tests where the beam temperature was constant, additional factors may also be present to cause this asymmetry and their influence only magnified by the lengthwise (and through-thickness) temperature gradient of the sample.

Once again, isolating the debonds from two instances in the test articles shown in the previous figure allows the extent of propagation to be viewed more clearly (Figure 51). Each debond has been shifted so that their peak displacement in the debond region lies along the same vertical line. This allows a direct comparison to be made of the magnitude of the debond buckling displacement while also observing the amount of rotation present.

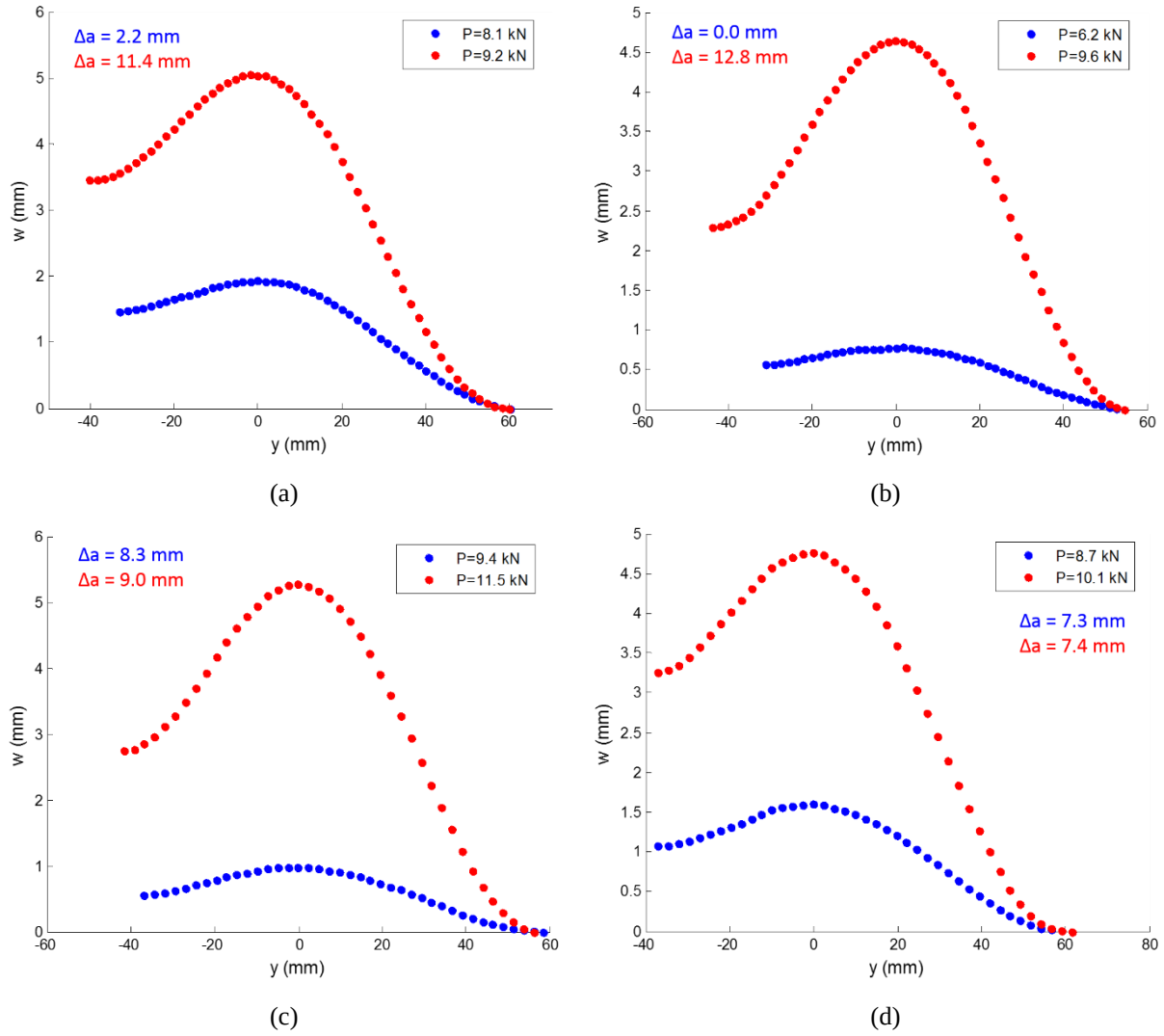

Fig. 51. Debond profiles showing propagation at two instances of the buckling test. (a) Test article D3-3 (L = 584 mm), (b) D3-4 (L = 584 mm), (c) D6-3 (L = 706 mm), (d) D6-4 (L = 711 mm).

Two differences between the previously shown low flux debonds (Figure 51) and the room temperature ones (Figure 40) are now evident. The first difference is the overall magnitude of the displacement in the debond region is smaller for the low flux test articles when compared to the room temperature samples. This could be due to the approximate 30% reduction in strength (Fig. **11**) at 65°C of the balsa core material leading to a core failure at the crack-front at a lower load level. This results in a reduction of the peak debond displacement simply because the core failure happens at reduced loading. Peak displacements for the low flux debond buckling just prior to global failure (red points in Figure 51) are approximately 3 mm while room temperature results

(red points in Figure 40) are between 5 – 9 mm. The second difference is that the peaks in the low flux buckled debond regions (Figure 51) are shifted towards the lower half of the beam while room temperature results show a more symmetric profile. The possible causes for this phenomenon are more complicated. Temperature differences between the upper and lower sections of the facesheet debond region, through-thickness temperature variations of the balsa core, and misalignment are just some of the reasons that could explain the debond shape (red data points) shown in Figure 51.

After a small amount of crack propagation, core failure occurs at one of the crack-fronts and triggers the global failure of the test article. The final shape of the sample is similar to the anti-symmetric shape observed in the room temperature tests and shown in Figure 52.

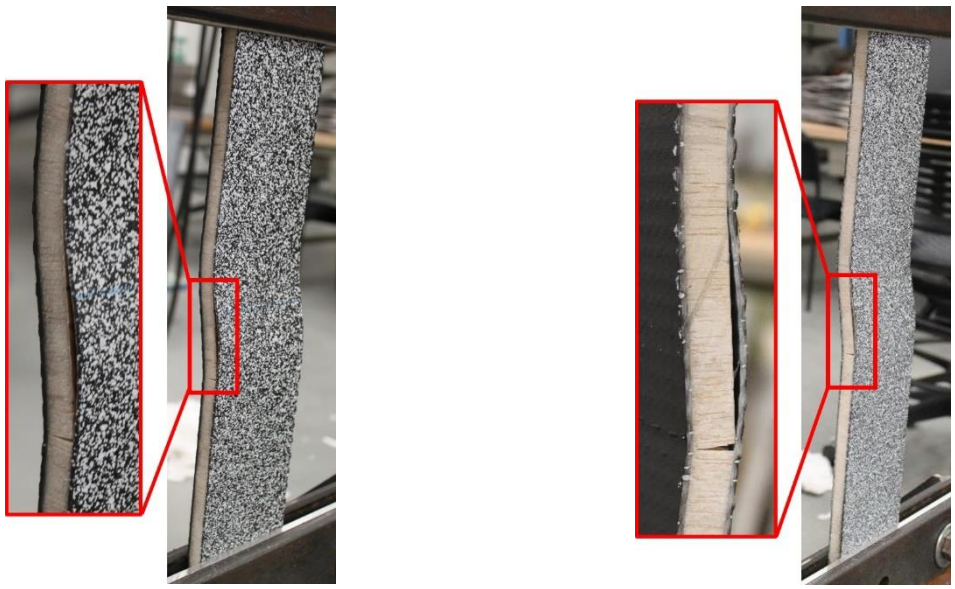

(a) (b)

Fig. 52. Balsa core damage at crack-front leads to asymmetric failure shape. (a) Test article D3-3 (L = 584 mm), (b) D6-3 (L = 706 mm).

All test articles with a 6.35 mm thick core had no signs of debond buckling or propagation prior to global failure. The post-failure shape was the same anti-symmetric profile as observed for all debond tests mentioned so far. Pictures taken post-test show that while debond buckling was not observed, a debond was present and global failure was initiated by a core failure at the crack-front as shown in Figure 53.

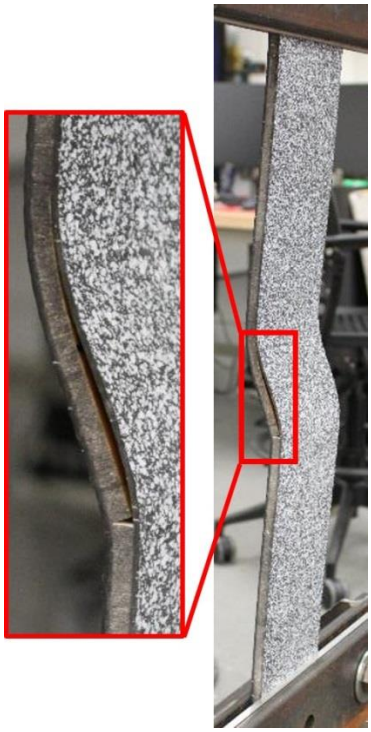

Fig. 53. Post-buckling failure of sample D3-3 with a 6.35 mm thick core.

A summary of the out-of-plane displacement profiles is shown below in Figure 54 where again the yellow and black profiles are just before and after global failure, respectively.

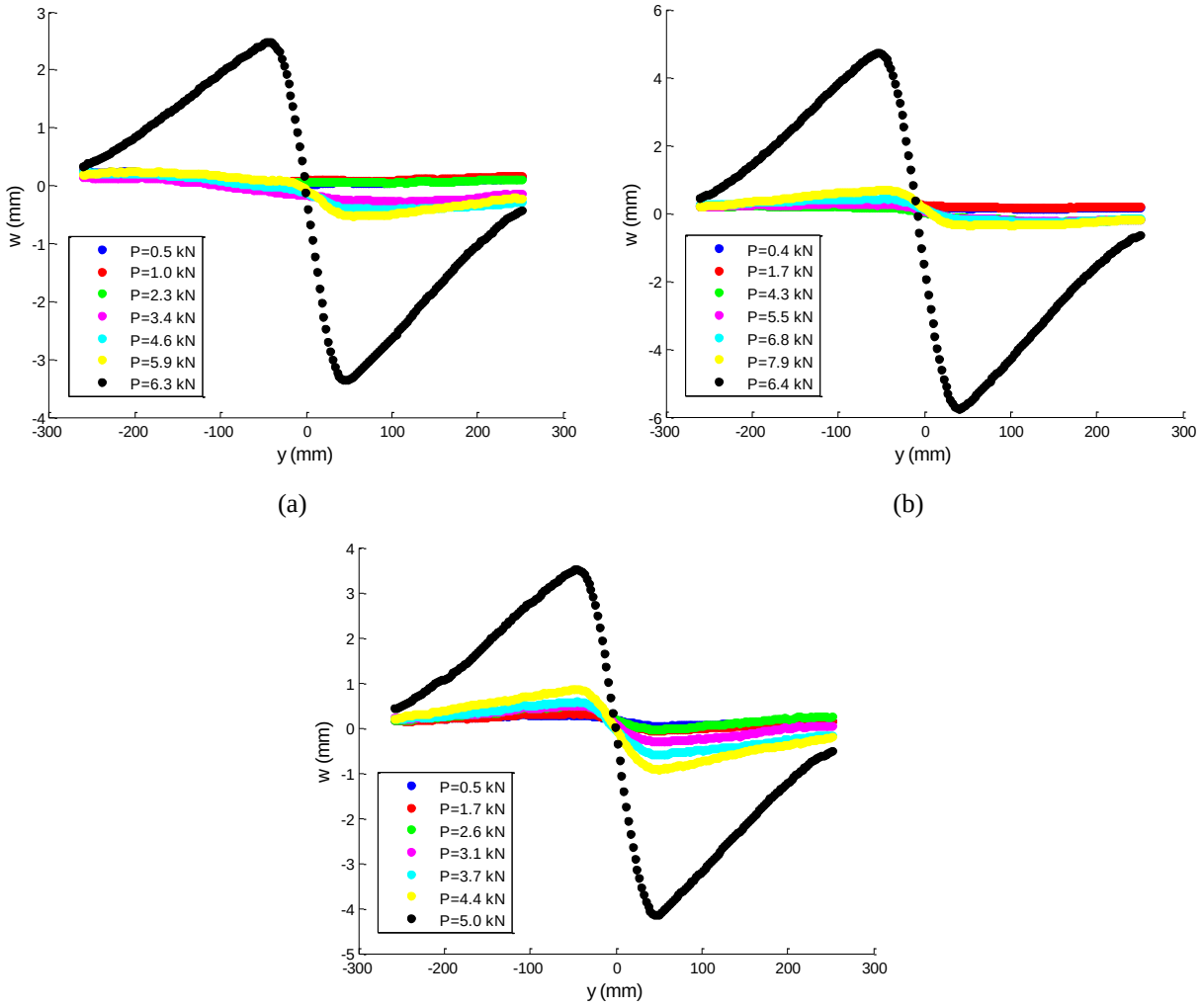

Fig. 54. Shape profiles of the 6.35 mm core samples throughout the low flux debond buckling test. (a) Test article D1-1 (L = 740 mm), (b) D2-1 (L = 737 mm), (c) D1-3 (L = 741 mm). Note that +y is the upper part of the sample and +w is towards the DIC cameras (and thus away from the heater panels).

4.4.2c No Debond Global Failure

Test articles with no debond and a 12.7 mm core thickness exposed to an average incident flux of 1.3 kW/m^2 exhibited similar initial out-of-plane response as room temperature tests in Figure 44. The initiation of global failure differed though with damage to the exposed facesheets being observed along with core damage near the gripped region. This behavior can be attributed to the higher bending stiffness of the thicker core samples increasing the critical buckling load. Since it is typically assumed that the facesheets carry the majority of the axial load, and the reduction of material properties due to the high temperatures, damage to the facesheets is now a possible

initiator of global failure. This damage took the form of either facesheet wrinkling or a compressive failure and may have occurred either just prior to buckling or from the post-buckling response. The out-of-plane displacement shape profiles of the 12.7 mm core (Figure 55) are shown below with the yellow and black profile lines as the moment just before and after global failure respectively.

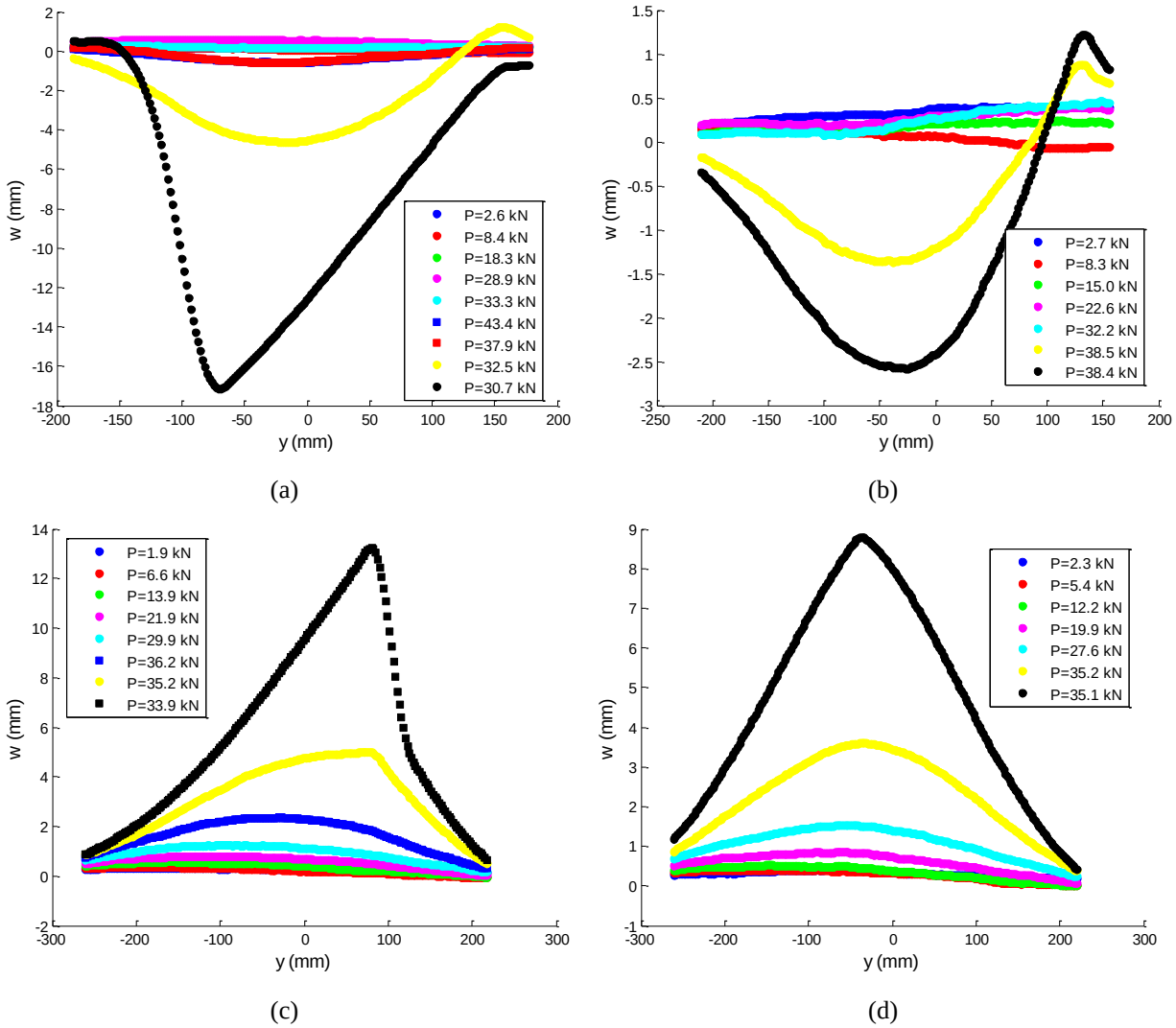

Fig. 55. Displacement profiles for 12.7 mm core thickness test articles. (a) Test article ND5-1 (L = 585 mm), (b) ND5-4 (L = 587 mm), (c) ND7-1 (L = 705 mm), (d) ND7-4 (L = 703 mm). Note that +y is the upper part of the sample and +w is towards the DIC cameras (and thus away from the heater panels).

The influence of the facesheet damage can be seen in the displacement profiles for the shorter length test article ND5-4 (Figure 55b) and longer length ND7-1 (Figure 55c). In the first, a compressive failure of both facesheets (Figure 56a) was observed in the upper portion of the beam

near the gripped region. This could be due to this location experiencing the highest temperatures on the sample and having the most reduced exposed side facesheet material properties. In the second, facesheet wrinkling is observed where the core failure occurs near the upper gripped region, although this most likely occurred after the core failure and subsequent debond as shown in Figure 56.

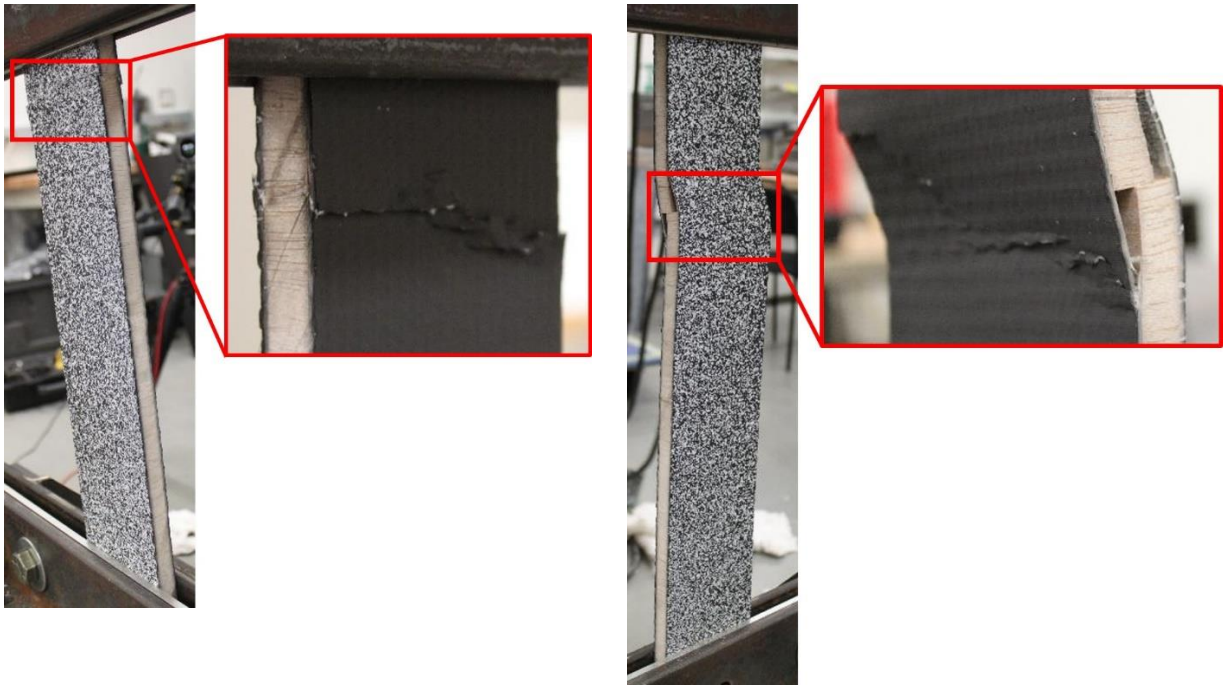

(a) (b)

Fig. 56. Facesheet damage observed for the low flux buckling tests on test articles with no debond. (a) ND5-4 (L = 587 mm), (b) ND7-1 (L = 705 mm).

All test articles with the 6.35 mm thick core did not have the same facesheet damage occur as their thicker counterparts. Instead the sample buckled out-of-plane symmetrically (Figure 57) before a core failure occurred near the gripped region. This can be seen in the following Figure 57 where the yellow line is the out-of-plane displacement just prior to core failure. The extent of the core damage was the least visible of all tests performed so far and no visible debonding was observed as shown in Figure 58.

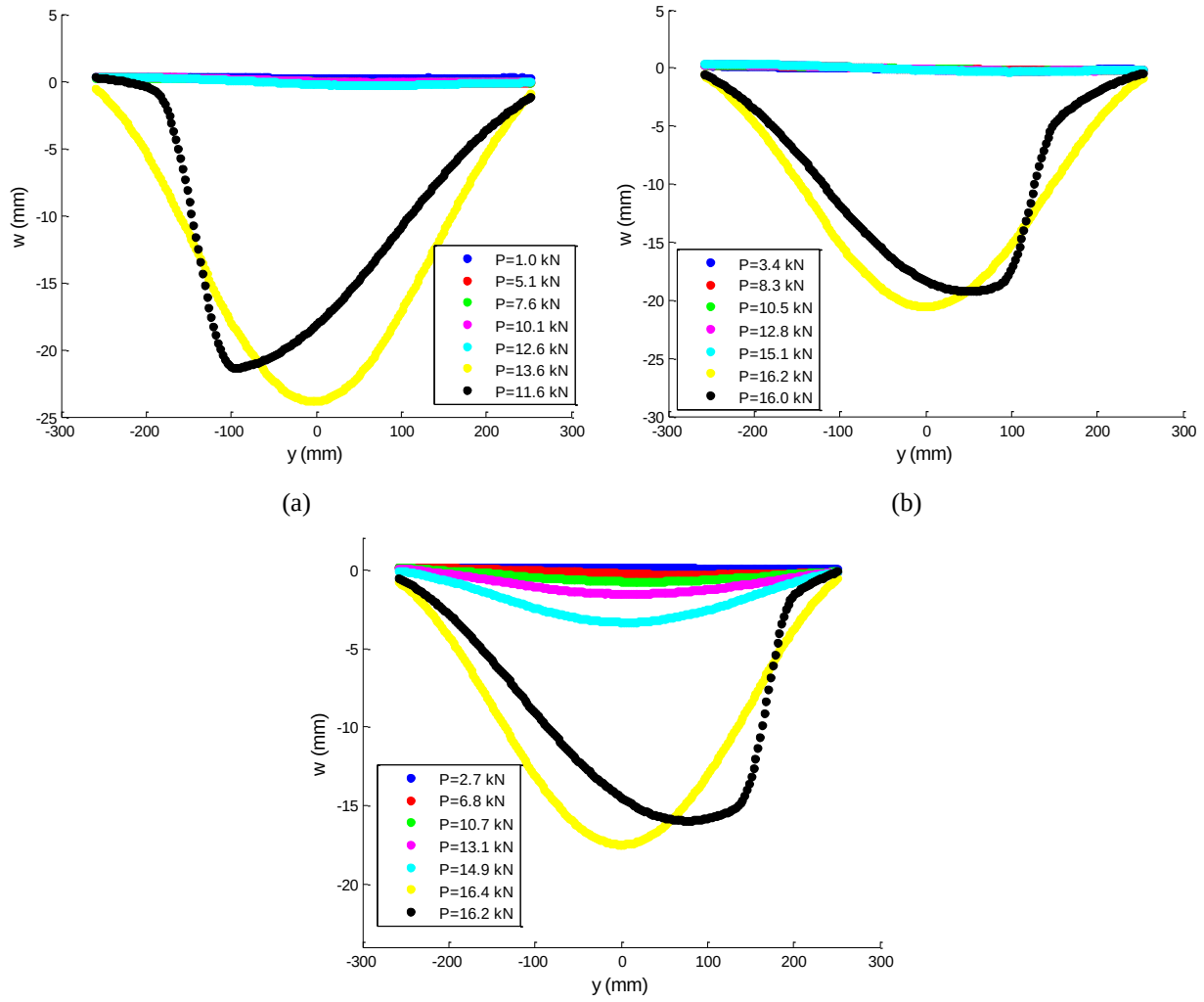

Fig. 57. Displacement profiles for 6.35 mm core thickness test articles with length of 740 mm. (a) Test article ND1-4, (b) ND2-2, (c) ND2-4. Note that +y is the upper part of the sample and +w is towards the DIC cameras (and thus away from the heater panels).

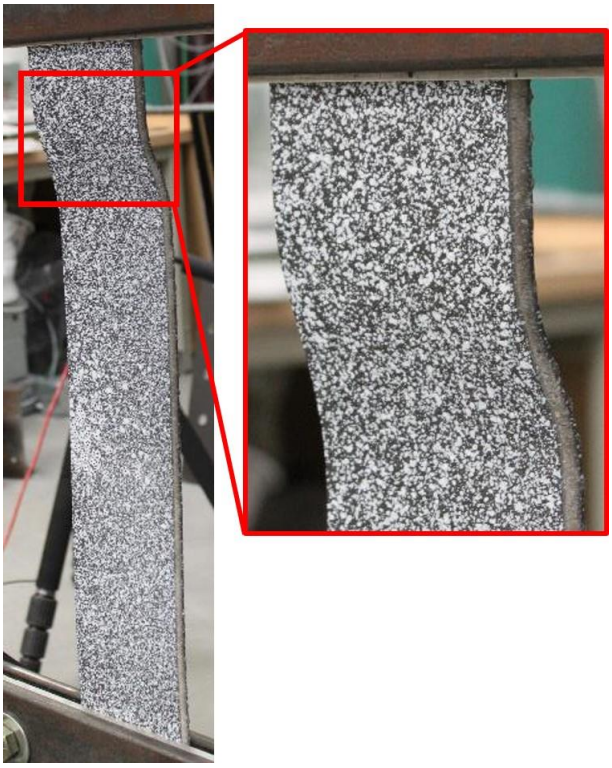

Fig. 58. Post-buckled shape of sample ND2-4 with a 6.35 mm core thickness.

4.4.3 High Flux Tests

Test articles exposed to the higher heat flux of 2.5 kW/m^2 experienced a vastly different failure response than the low flux test articles. Damage to the exposed facesheet in terms of a wrinkling deformation was observed on the majority of samples containing no debond. Whether this occurred prior to the significant out-of-plane displacements from the buckling response, or as a result of these deformations, is unknown due to the minimal time between wrinkling and a global failure of the test article. Shorter length samples whose core thickness was 12.7 mm experienced both a core failure near the gripped region along with wrinkling while longer length samples had no visible core damage and just a centrally located wrinkle on the exposed facesheet. Test articles containing a debond differed from the low flux exposure tests in that debond buckling and propagation were almost nonexistent. Instead their failure was more similar to the previous response of the thinner (6.35 mm) core samples where the sample transitioned into an anti-symmetric post-buckling shape with no debond buckling observed.

4.4.3a Temperature Profiles

Similar to the low exposure tests, high flux exposures at approximately 2.5 kW/m^2 induced a spatially varying temperature profile on both the exposed and unexposed sides of the sandwich composite test article. Again this is due to the inhomogeneous thermal properties of the balsa core panel having both a varying thermal conductivity within each individual balsa core section, and between the varying sections that make up the panel. A small subset of these exposed side temperatures is shown in Figure 59 to highlight the variability between test articles, the remaining temperature fields of all test articles are shown in Appendix D.

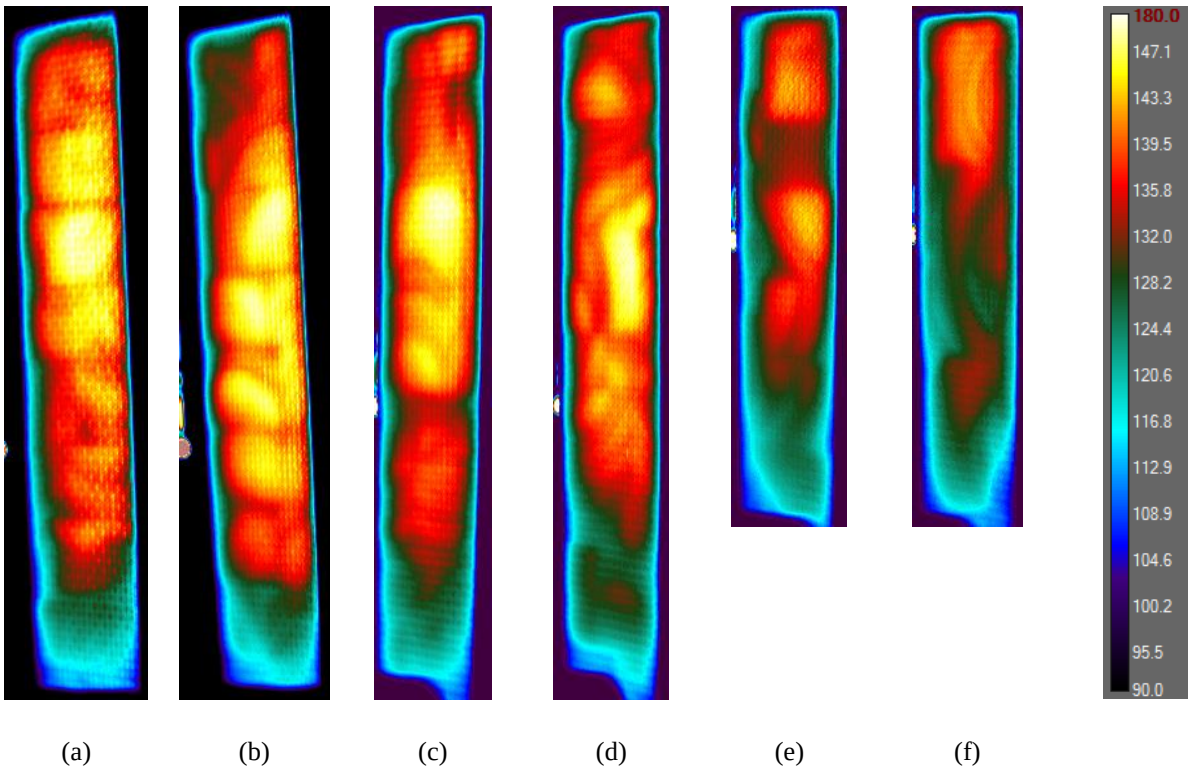

Fig. 59. Temperature (°C) of exposed side from high incident heat flux exposure. (a) ND2-3 (L = 738 mm), (b) D2-4 (L = 733 mm), (c) ND7-5 (L = 701 mm), (d) D6-5 (L = 706 mm), (e) ND5-3 (L = 590 mm), (f) D3-2 (L = 582 mm).

The unexposed side temperature profiles show a similar variation of temperature in the length and widthwise directions to the low flux profiles (Figure 48). This temperature variation is easily observed in Figure 60 even though the incident flux levels on the exposed facesheet (Figure 21) show minimal widthwise variation. As expected, temperatures on the lower regions of the 12.7

mm core thickness test articles (Figure 60c-d) are significantly lower than similar length but thinner core thickness test articles (Figure 60a-b).

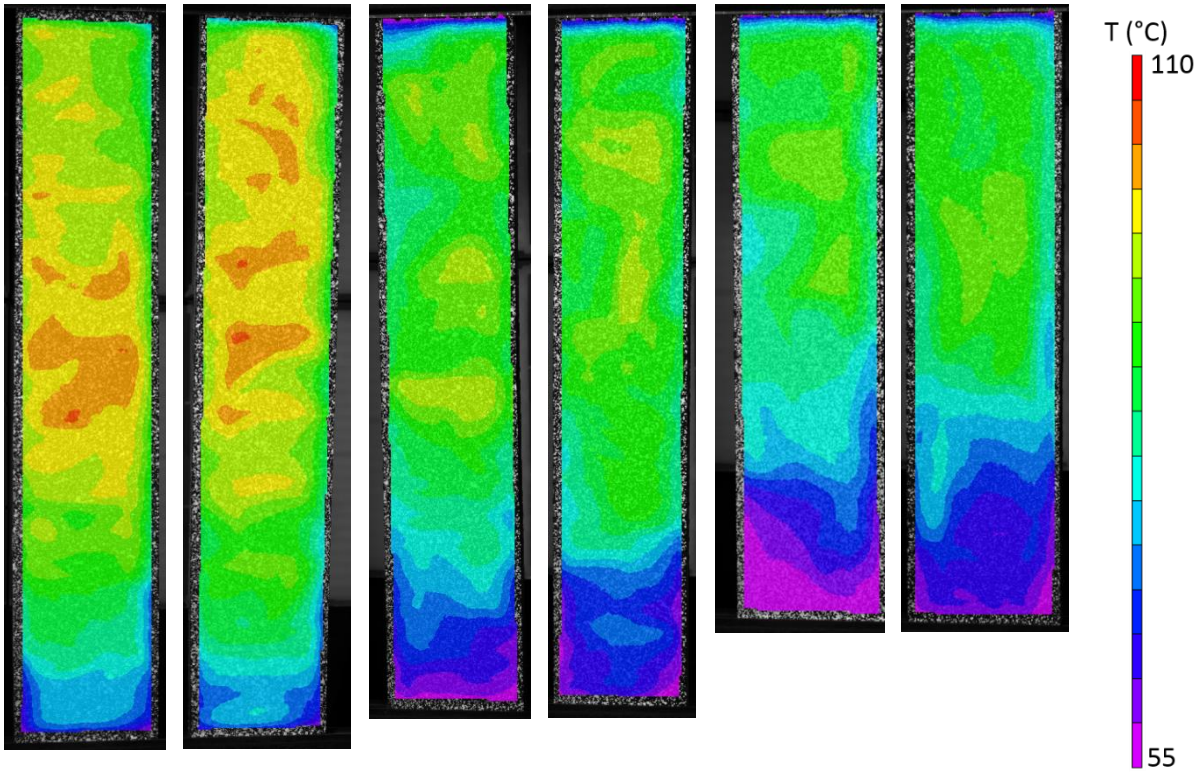

(a) (b) (c) (d) (e) (f)

Fig. 60. Temperature (°C) of unexposed side from high incident heat flux exposure. (a) ND2-3 (L = 738 mm), (b) D2-4 (L = 733 mm), (c) ND7-5 (L = 701 mm), (d) D6-5 (L = 706 mm), (e) ND5-3 (L = 590 mm), (f) D3-2 (L = 582 mm).

By taking the vertical line profile of the temperatures similar to what was done for displacements (Figure 38) a measure of the change in temperature along the length of the sample can be shown in Figure 61. This shows the significant drop in temperatures towards the lower gripped region from the reduced incident flux in this location. Additionally, the variation in temperature due to the block-to-block variation of the balsa core thermal properties can be seen in the upper region of the following plots, where the local minimums are most likely due to the adhesive surfaces between blocks of balsa wood.

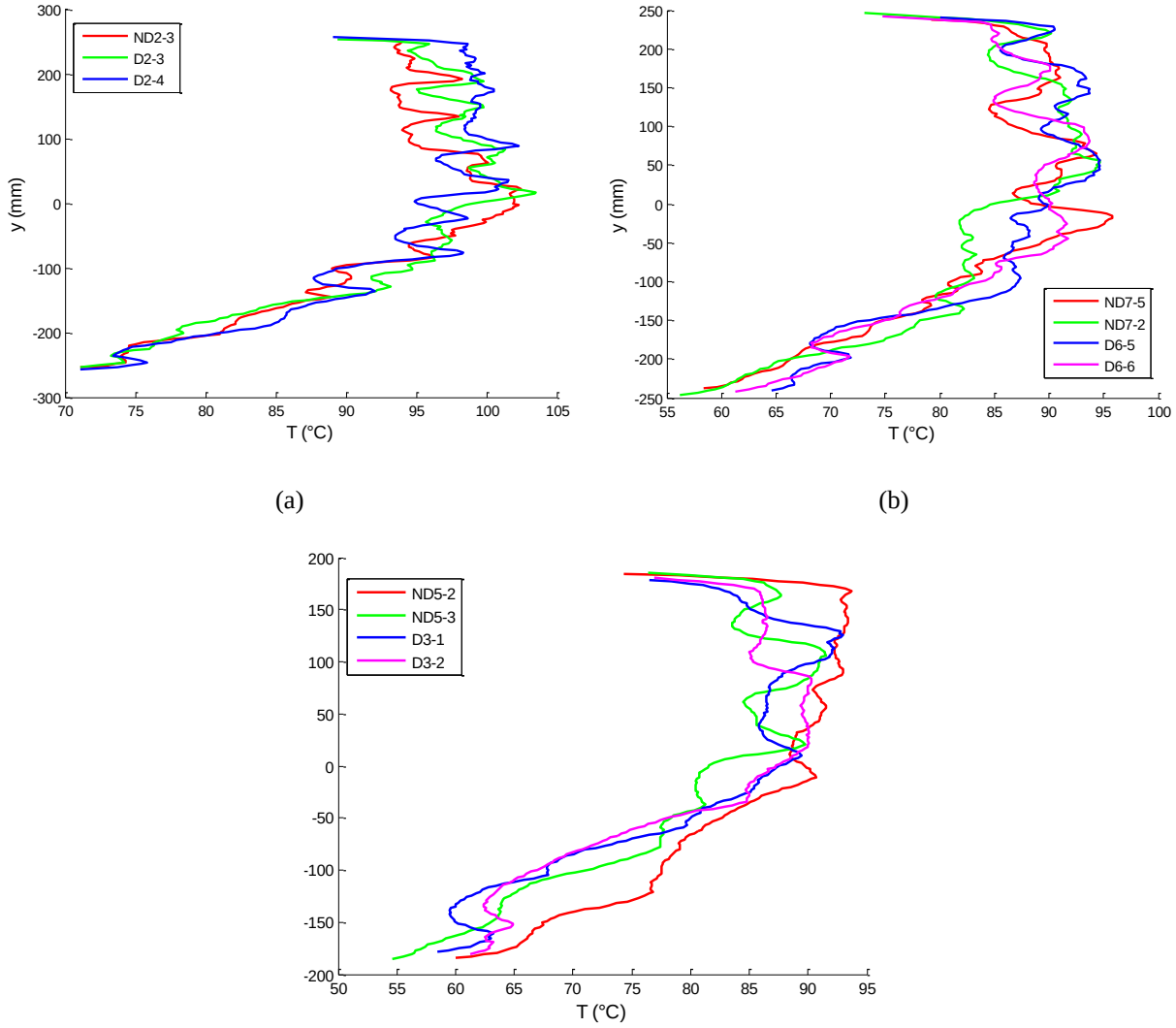

Fig. 61. Vertical temperature profile of high flux exposed test articles. (a) Core thickness of 6.35 mm, nominal length of 740 mm, (b) core thickness of 12.7 mm, nominal length of 705 mm, (c) core thickness of 12.7 mm, and nominal length of 585 mm.

4.4.3b Debond Buckling and Growth

Only one test article out of all tested regardless of core thickness exhibited a small amount of debond buckling and propagation. This sample (Figure 62b) had a core thickness of 12.7 mm with a total length of 583 mm. All other samples failed directly into an anti-symmetric shape previously observed to primarily occur with the thinner core test articles. Global failure was again triggered by a core failure at one of the crack-fronts for all samples and a widthwise wrinkle was observed

on the exposed facesheet. By taking a vertical line profile through the center of the sample, the progression to global failure is shown in Figure 62.

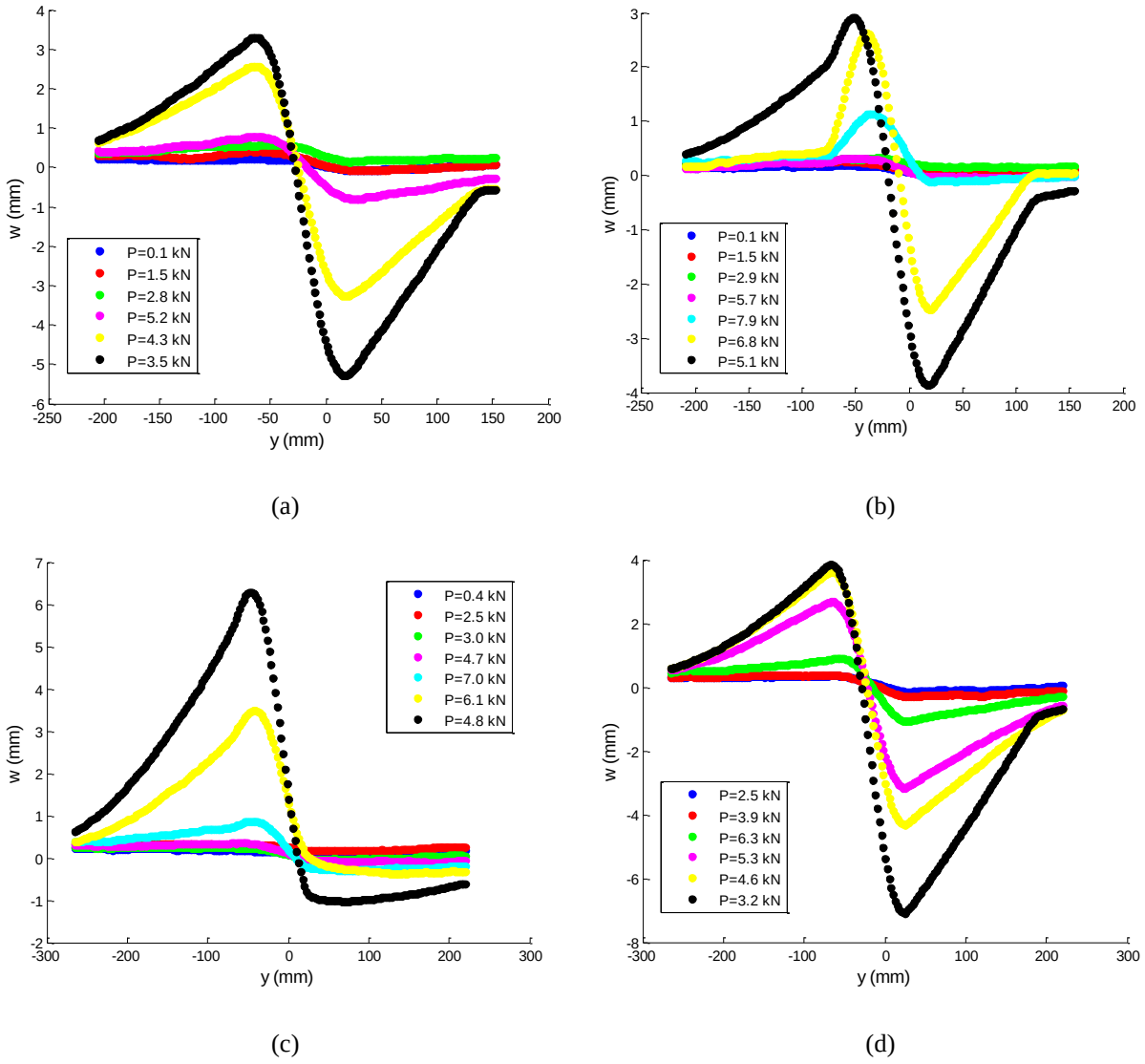

Fig. 62. Shape profiles of the 12.7 mm core samples throughout the high flux debond buckling test. (a) Test article D3-1 (L = 578 mm), (b) D3-2 (L = 582 mm), (c) D6-5 (L = 706 mm), (d) D6-6 (L = 705 mm). Note that +y is the upper part of the sample and +w is towards the DIC cameras (and thus away from the heater panels).

All post-buckling shape profiles exhibit a highly non-symmetrical shape about the center of the sample. One possible reason for this is similar to the low flux test explanation, where a significantly higher temperature on the upper half of the sample compared to the lower half creates large discrepancies between the material properties of both regions. This combined with the wrinkling that occurs on the exposed side allows one side of the test article to displace a greater amount than

the other. As was done with previous debonds observed, isolating the two instances in the test article allows the extent of propagation to be viewed more clearly (Figure 63). Each debond instance has again been shifted so that their peak displacement in the debond region lies along the same vertical line. This allows a direct comparison to be made of the magnitude of the debond buckling displacement while also observing the amount of rotation present.

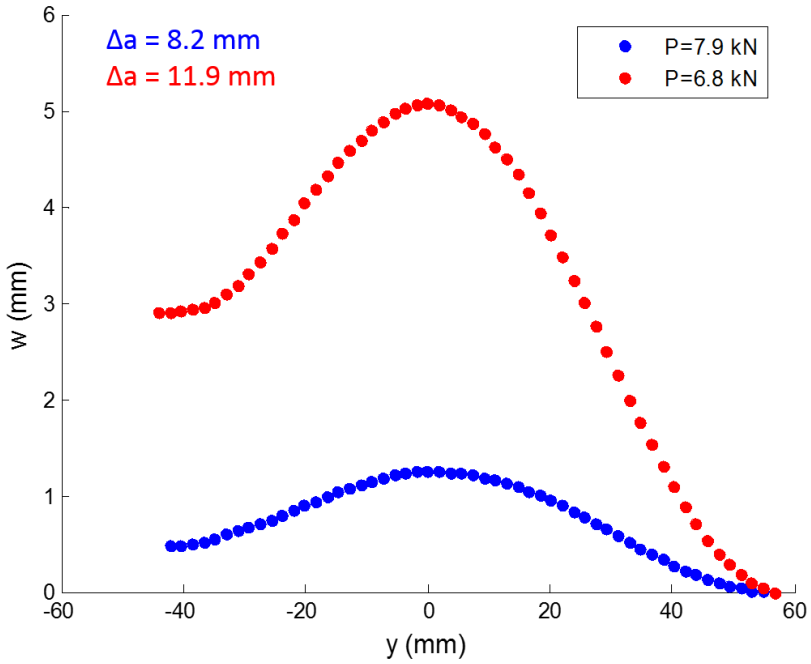

Fig. 63. Debond profiles showing propagation at two instances of the buckling test for sample D3-2 (L = 582 mm).

The possible reasons why only a single sample experienced debond buckling followed by propagation are varied. Firstly, the inhomogeneity of the balsa core properties, both thermal and mechanical, may have prevented an initial core failure at the crack-front while the increased interface temperatures reduced the interfacial toughness of the facesheet/core interface. This would allow the facesheet debond to grow a small amount until encountering a different region of the balsa core material section whose strength is further reduced when compared to the area where the crack-front initially resided leading to a core failure. Second, as with all large scale tests, small amounts of misalignment in the boundary conditions, combined with the distortions of the sample due to the spatially varying temperature could create enough of an eccentricity to bypass debond buckling and fail immediately in the non-symmetric shapes shown in Figure 62.

Core failure at one of the two crack-fronts occurred for all the previously discussed samples. In addition to this, facesheet wrinkling was observed post-test on the exposed facesheet opposite the location where the core failure occurred. This is shown in the following Figure 64 where additional wrinkling is observed near the upper gripped region.

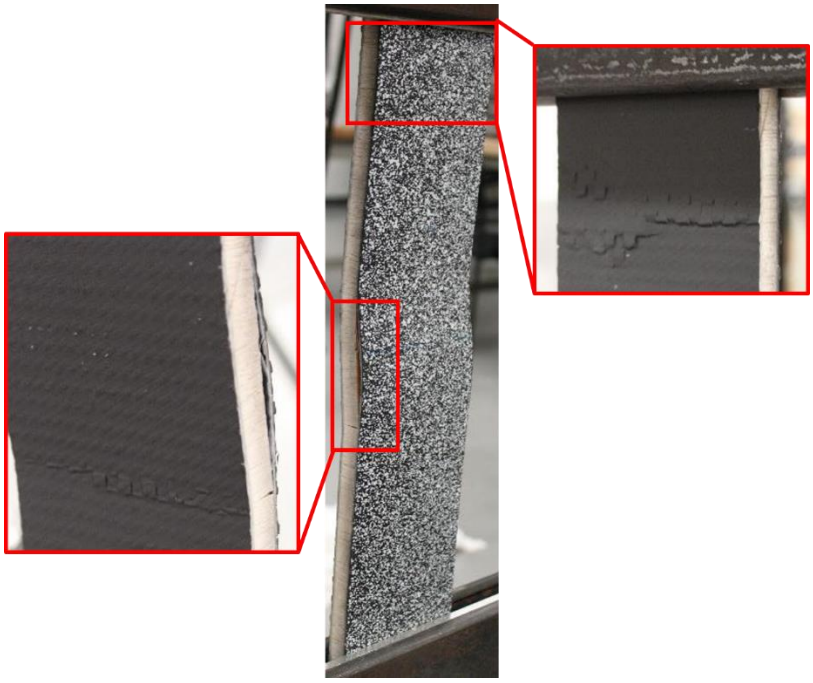

Fig. 64. Anti-symmetric post-buckling shape observed in failure of debond sample D3-2. Wrinkling observed on exposed facesheet opposite of core failure location and near upper gripped region.

All test articles with a 6.35 mm thick core had no signs of debond buckling or propagation prior to global failure. The post-failure shape was the same anti-symmetric profile as observed for all debond tests mentioned so far regardless of flux exposure. Pictures taken post-test show that while debond buckling was not observed, a debond was present and global failure was initiated by a core failure at the crack-front with a widthwise wrinkle on the exposed side opposite where core failure occurred as shown in Figure 65.

Fig. 65. Post-buckling failure of sample D2-4 with a 6.35 mm thick core.

A summary of the out-of-plane displacement profiles is shown below in Figure 66 where again the yellow and black profiles are just before and after global failure, respectively.

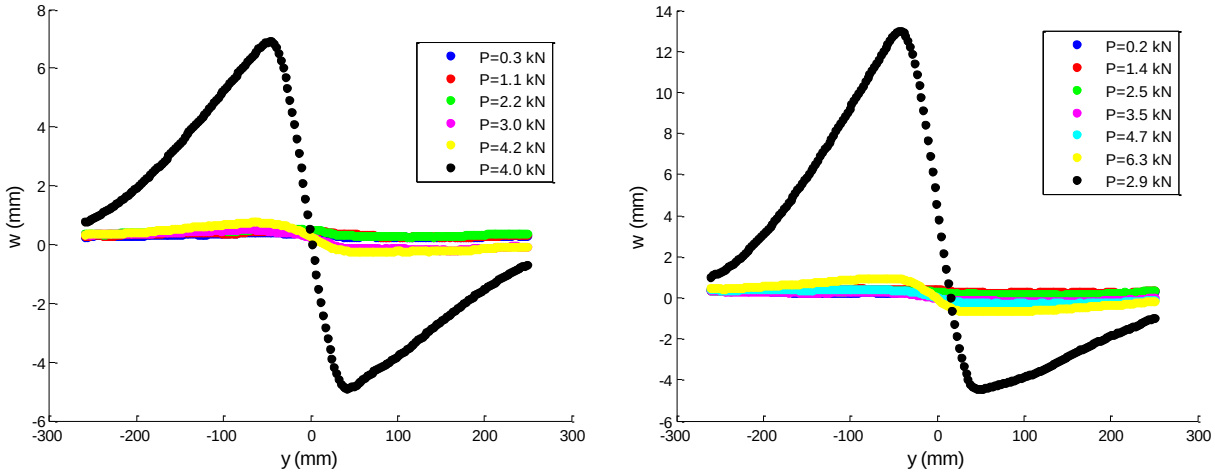

(a) (b)

Fig. 66. Shape profiles of the 6.35 mm core samples throughout the high flux debond buckling test. (a) Test article D2-3 (L = 735 mm), (b) D2-4 (L = 733 mm). Note that +y is the upper part of the sample and +w is towards the DIC cameras (and thus away from the heater panels).

4.4.3c No Debond Global Failure

Test articles with a 12.7 mm core thickness exposed to a nominal 2.5 kW/m^2 incident flux all had some form of wrinkling deformation observed post-test on the exposed facesheet. This widthwise wrinkling often occurred near the center location of the sample and acted as a pivot location for excessive out-of-plane deformations to occur. This can be attributed to the extremely high temperatures of the exposed facesheet (≅150°C) reducing the facesheet properties to such a degree that the loads on the sample created a localized wrinkling. After careful review of all analysis data, it was not determined whether wrinkling happened prior to the test article experiencing excessive out-of-plane displacement or as a result of it. One significant difference between the high flux test results when compared to the low flux is the lack of core damage occurring in the samples which had previously triggered a global failure. Instead, even though all samples experienced large out-of-plane deformations, no core damage occurred near the gripped region as had been seen in the room temperature and low flux results. The out-of-plane displacement shape profiles of the 12.7 mm core (Figure 67) are shown below where the influence of the exposed facesheet wrinkling can be observed by the sharp post-buckling profile shape.

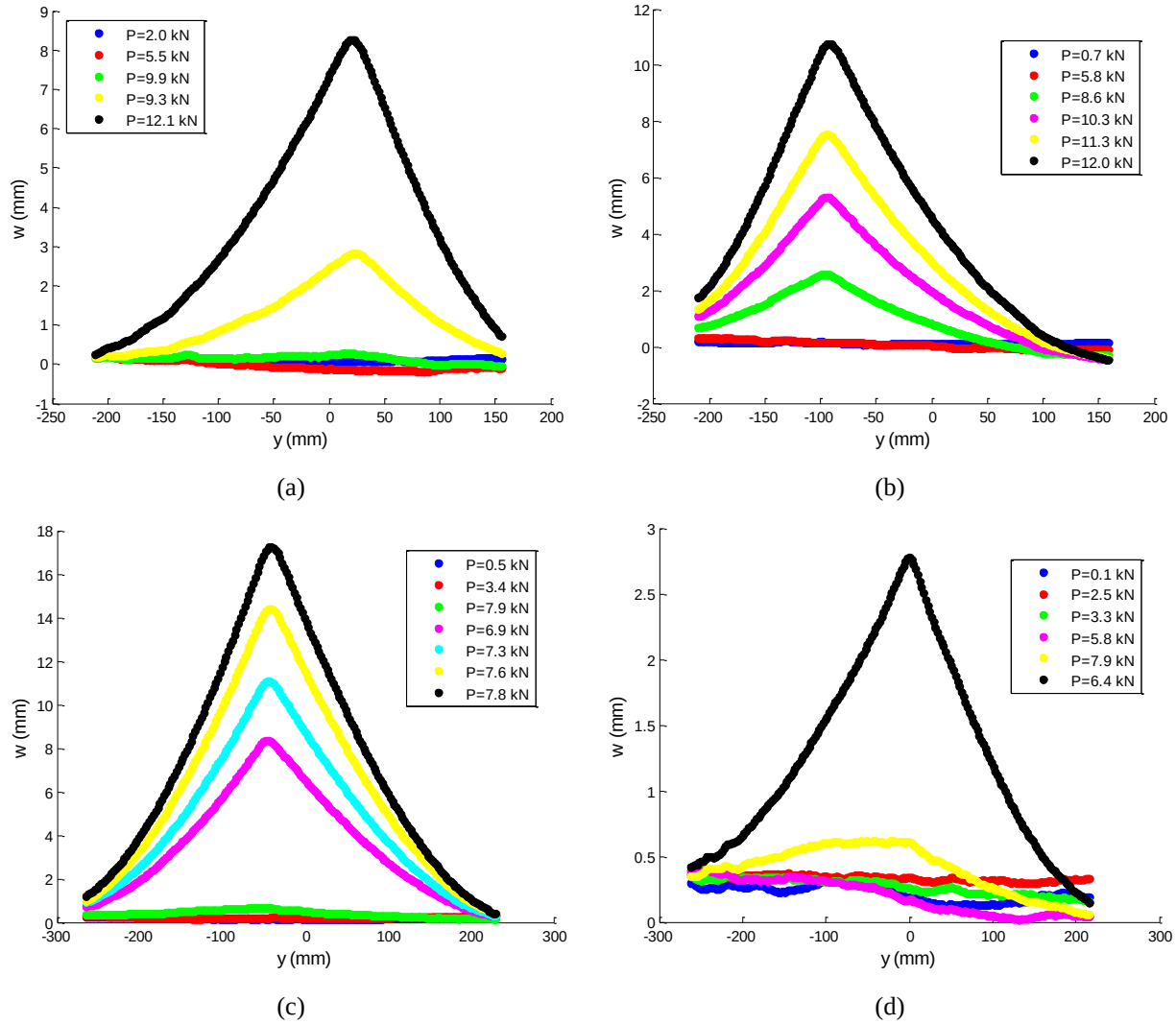

Fig. 67. Displacement profiles for 12.7 mm core thickness test articles. (a) Test article ND5-2 (L = 589 mm), (b) ND5-3 (L = 590 mm), (c) ND7-2 (L = 713 mm), (d) ND7-5 (L = 702 mm). Note that +y is the upper part of the sample and +w is towards the DIC cameras (and thus away from the heater panels).

Another difference is evident when comparing the shape profiles in the previous figure to their low flux counterparts (Figure 55). Even after wrinkling and excessive out-of-plane displacements have taken place, the load carrying capacity of the sample increases to well above the load where wrinkling was first observed. This could possibly be explained in two ways. First, as the sample deflects away from the heater panels the temperature on the unexposed side may decrease, slightly increasing the stiffness of that facesheet as the temperature lowers. While this may occur to some degree, the short time it takes the sample to deflect outwards, along with the small out-of-plane displacements would not allow the temperature to decrease enough to notice a sizeable stiffness

increase. Second, while a small localized wrinkling band is observed, the softening of the core due to the very high temperatures provides enough additional compliance so that the core does not have a sudden failure. Combined with the wrinkling damage lowering the overall energy of the structure, so that for any additional damage to occur in the wrinkled region, a significant increase in the load is required. Two examples of the wrinkling failure shapes of the 12.7 mm core samples is shown in Figure 68, where (b) is the only test to show a core damage occurring near the gripped region combined with a wrinkling deformation.

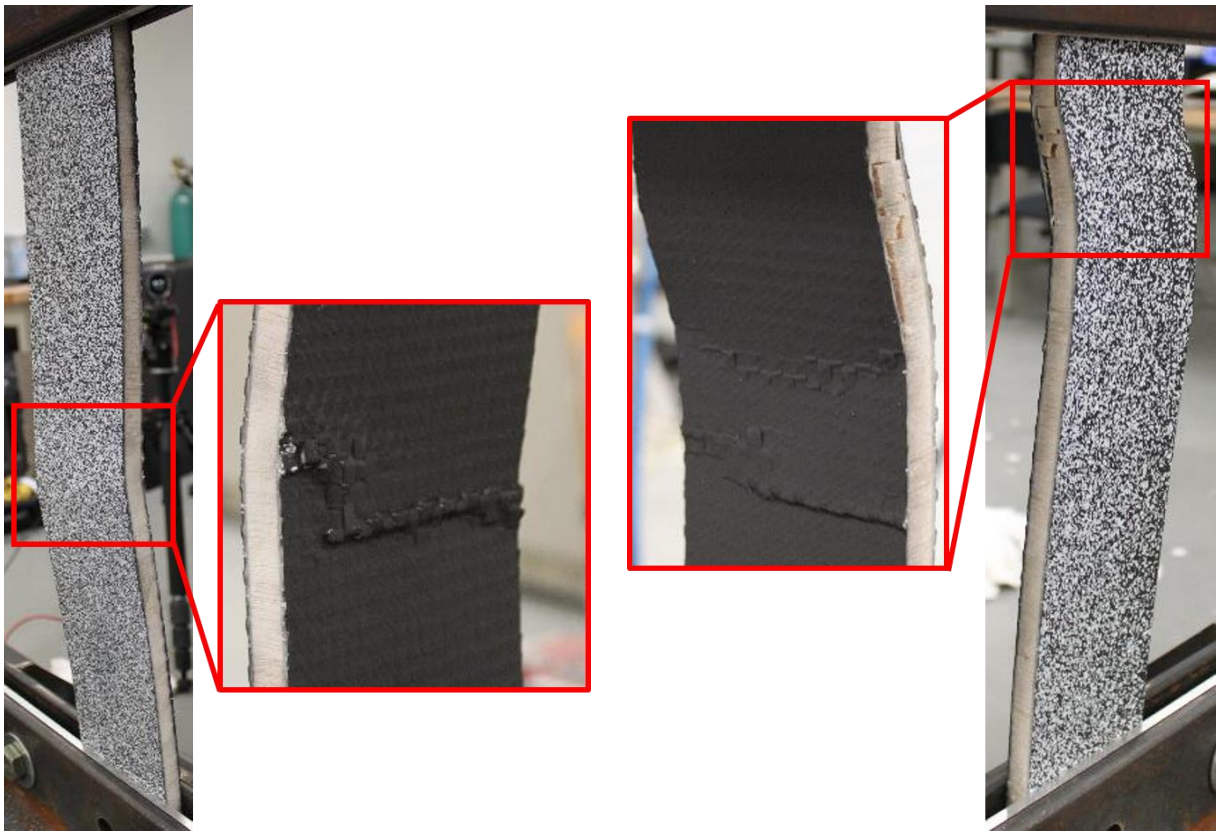

(a) (b)

Fig. 68. Facesheet damage observed for the high flux buckling tests on test articles with no debond. (a) ND7-5 (L = 702 mm), (b) ND5-2 (L = 589 mm).

Both test articles with the 6.35 mm thick core had the same facesheet damage occur as their thicker counterparts with only exposed facesheet wrinkling observed post-test and no noticeable core damage triggering a sudden global failure. The displacement shape profiles are shown in Figure 69.

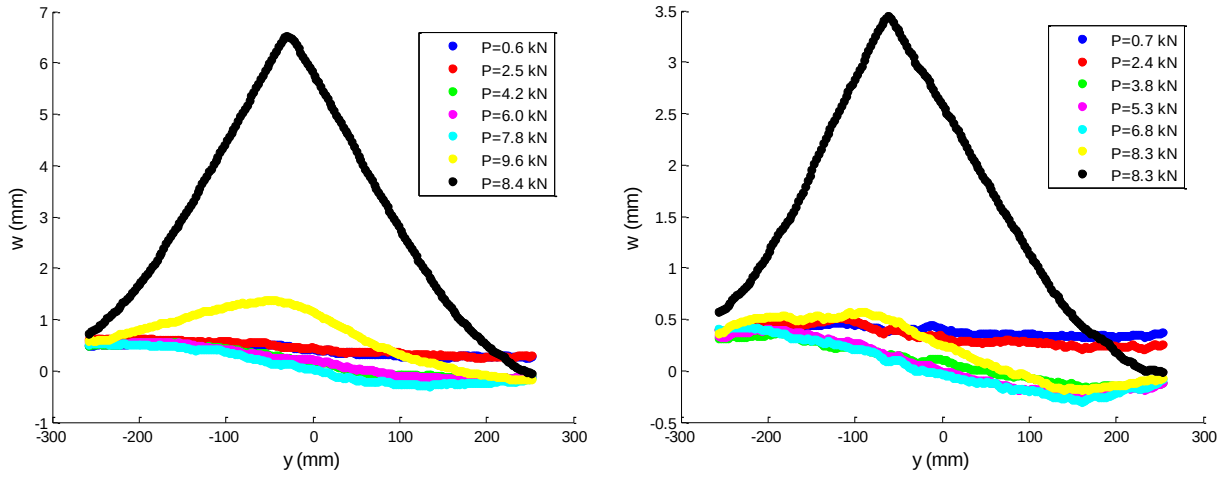

(a) (b)

Fig. 69. Displacement profiles for 6.35 mm core thickness test articles with nominal length of 740 mm. (a) Test article ND1-1, (b) ND2-3. Note that +y is the upper part of the sample and +w is towards the DIC cameras (and thus away from the heater panels).

4.4.4 Summary of One-Sided Heat Exposure Debond Buckling Results

Additional information on the influence of the debond and one-sided-heat exposure can be gleaned from the various single point measurements that can be taken using the DIC. The first is the load-displacement ($P - w$) curves with the out-of-plane displacement taken at the center of the sample for all test articles with no debond introduced between the facesheet and core. As expected, with an increase in the average incident flux the sample is exposed to, a significant reduction in the load carrying capacity prior to global buckling is observed. These *P-w* plots are shown below in Figure 70 through Figure 72. Note, in each, a positive out-of-plane displacement corresponds to a post-buckling shape deflecting away from the heater panels.

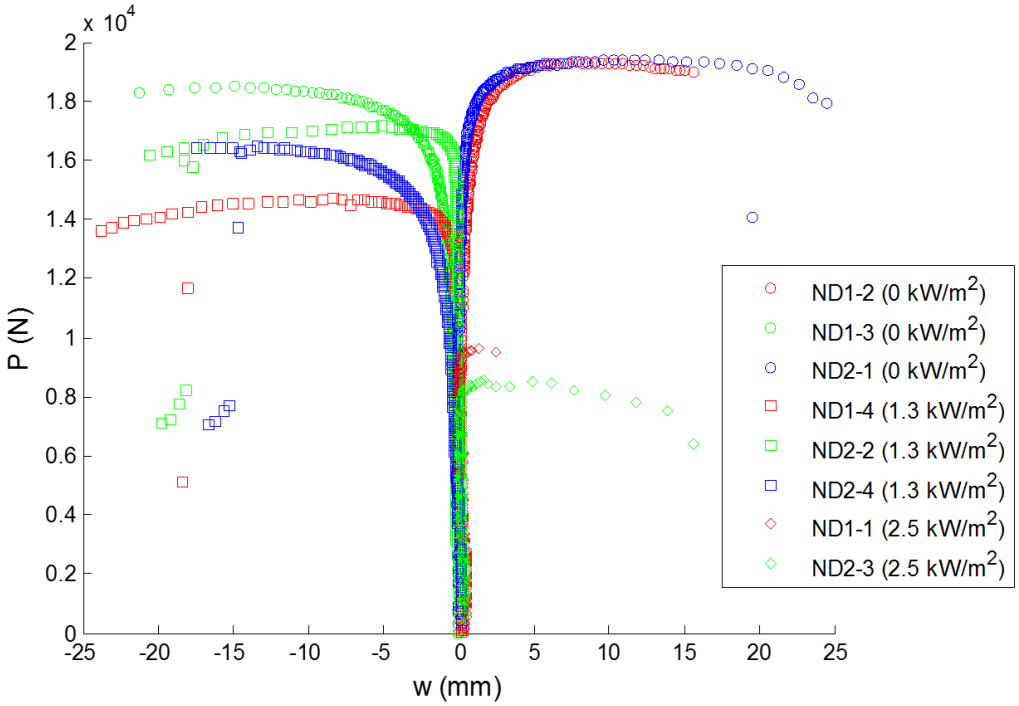

Fig. 70. Load-displacement curves for test articles with a 6.35 mm core thickness, nominal length of 740 mm, and no debond.

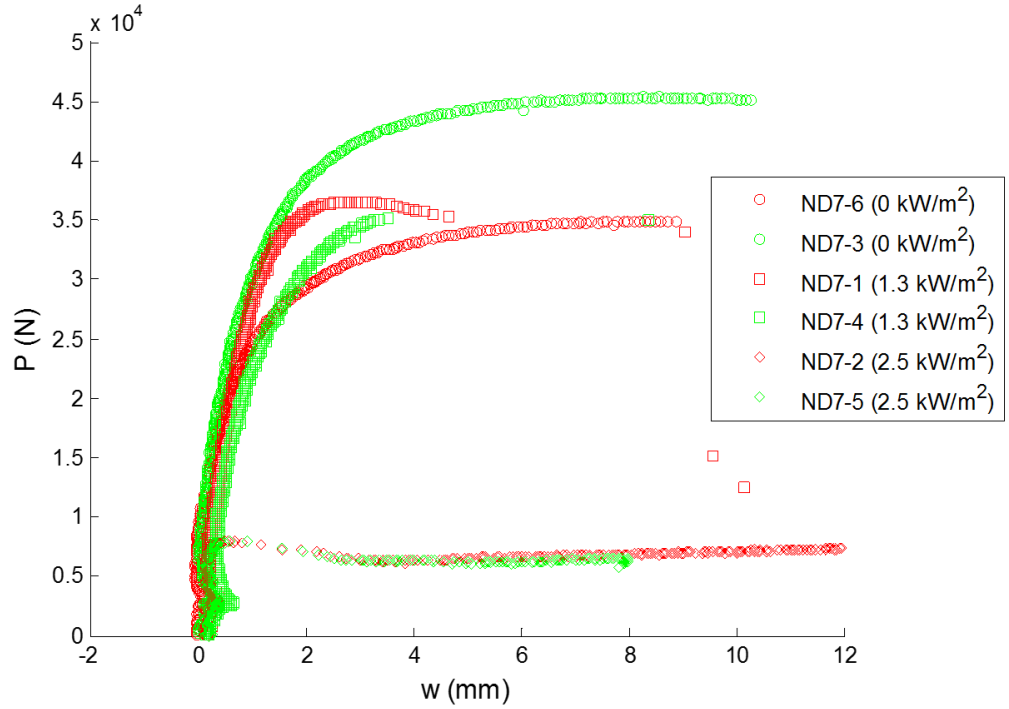

Fig. 71. Load-displacement curves for test articles with a 12.7 mm core thickness, nominal length of 705 mm, and no debond.

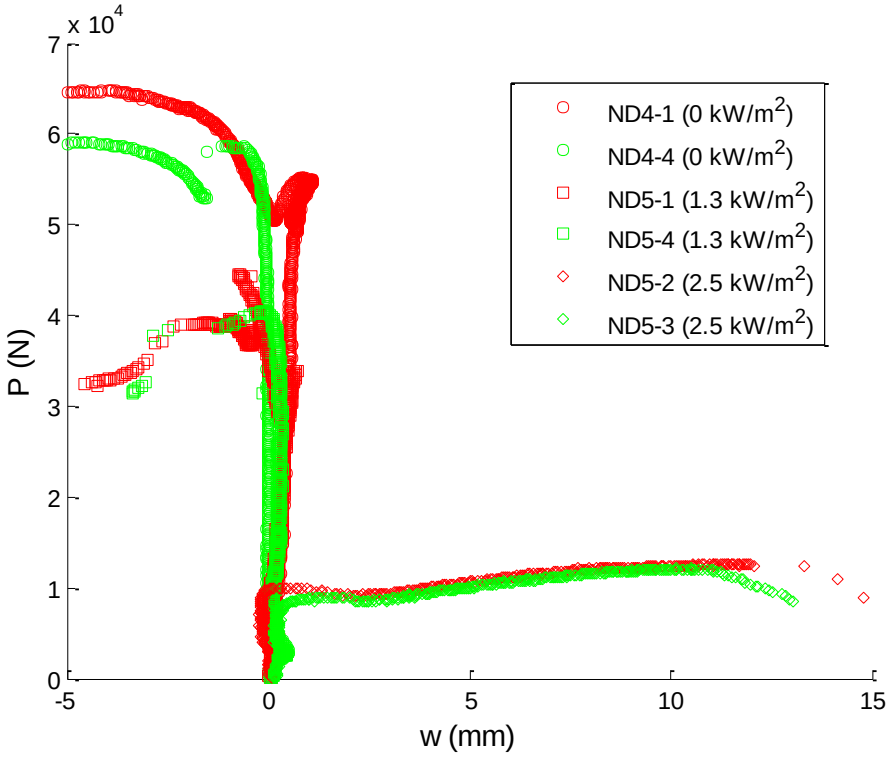

Fig. 72. Load-displacement curves for test articles with a 12.7 mm core thickness, nominal length of 585 mm, and no debond.

In the above short length buckling test series (Figure 72), the occurrence of damage discussed in previous sections is reflected by a sudden drop in loading at room-temperature. Both long length buckling test series curves, regardless of core thickness, show a neutral post-buckling response until core failure triggers a global buckling failure. These shorter length samples experienced additional damage mechanisms due to their reduced lengths increasing the critical buckling load of the samples.

For those samples with a debond between the unexposed facesheet and core where debond buckling and propagation occurred, plotting the load-displacement curve is misleading due to the displacement being made of two components. The first is the global out-of-plane displacement of the beam as would be seen from test articles with no debond. The second is the local out-of-plane displacement of the debond region after buckling has occurred. A more natural measure of the response of the structure can be shown by plotting the load as a function of the axial engineering

strain in a small location in the center of the debond region. These are shown below in Figure 73 and Figure 74 along with an additional plot of the linear region prior to debond buckling.

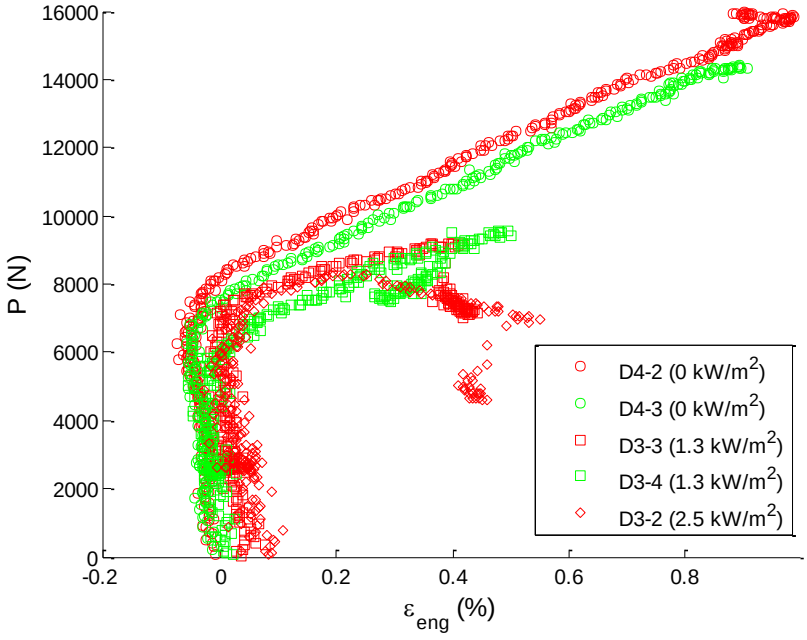

(a)

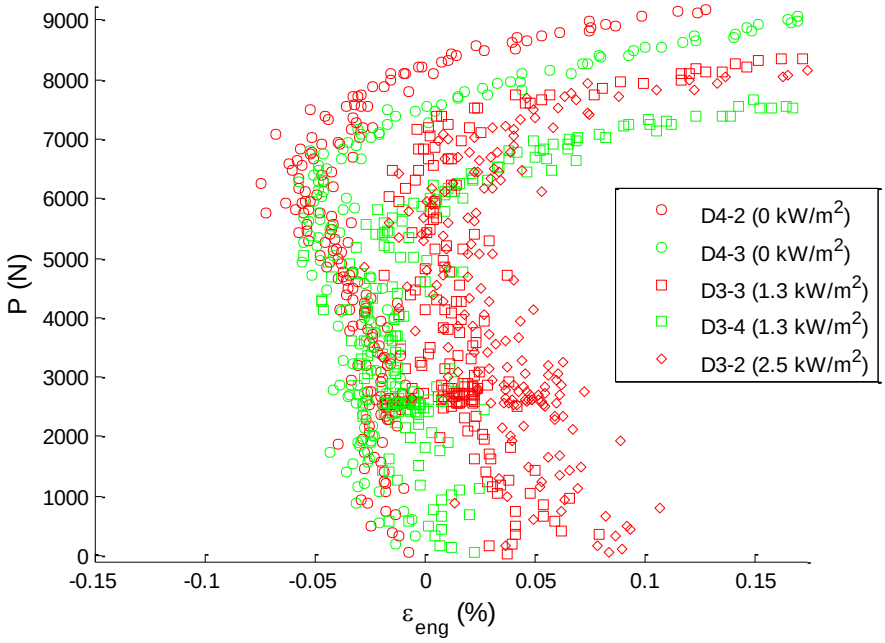

(b)

Fig. 73. A load-engineering strain curve for test articles with a 12.7 mm core thickness and a nominal length of 585 mm. (a) Overall curve, (b) focused about the linear load-strain region prior to debond buckling.

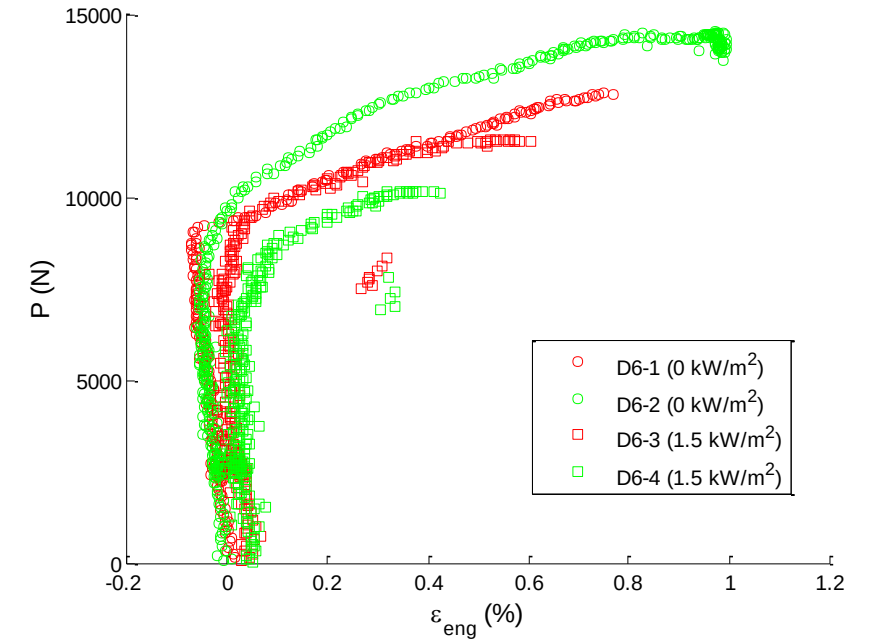

(a)

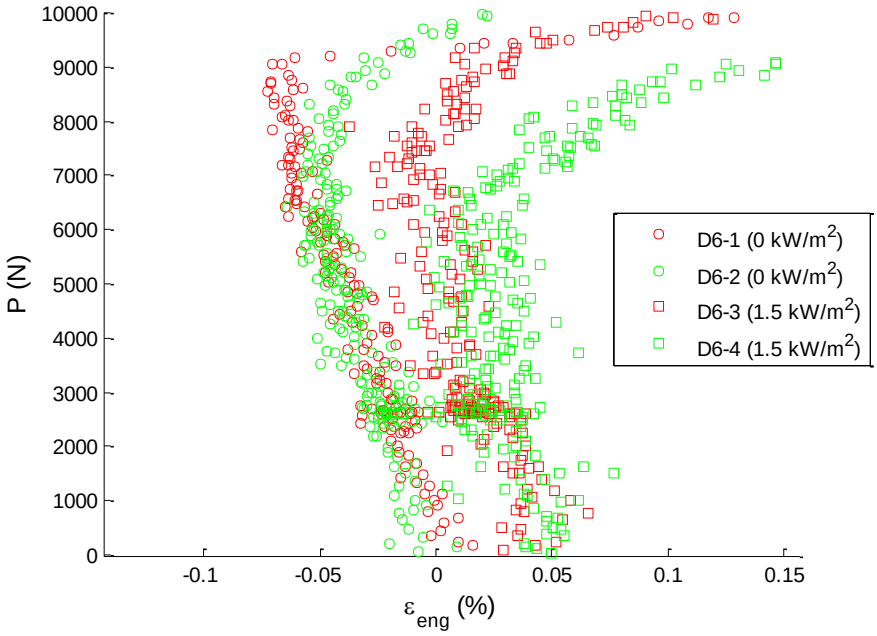

(b)

Fig. 74. A load-engineering strain curve for test articles with a 12.7 mm core thickness and a nominal length of 705 mm. (a) Overall curve, (b) focused about the linear load-strain region prior to debond buckling.

As the load is increased and prior to localized buckling of the debond region the entire unexposed facesheet is under a linearly increasing compressive stress reflected in the linear load-strain curve of Figure 73b and Figure 74b. After separating from the underlying core, the debond region begins

to buckle inducing a curvature that creates tensile stresses (and positive strains) on the outer most ply of the facesheet. Continued buckling and propagation occurs, increasing the strain, until total failure occurs at one of the two crack-fronts. Another observation is the influence of the temperature change creating small thermal strains shown as a positive shift in the initial linear load-strain line.

An additional measure of the influence of the debond combined with one-sided heat exposure is in the load-end shortening curves (Figure 75 to Figure 77). These show a significant decrease (≅50%) in peak loads sustained by debond specimens compared to those with no debond and damage such as core failure and wrinkling correspond with sudden drops in the curves.

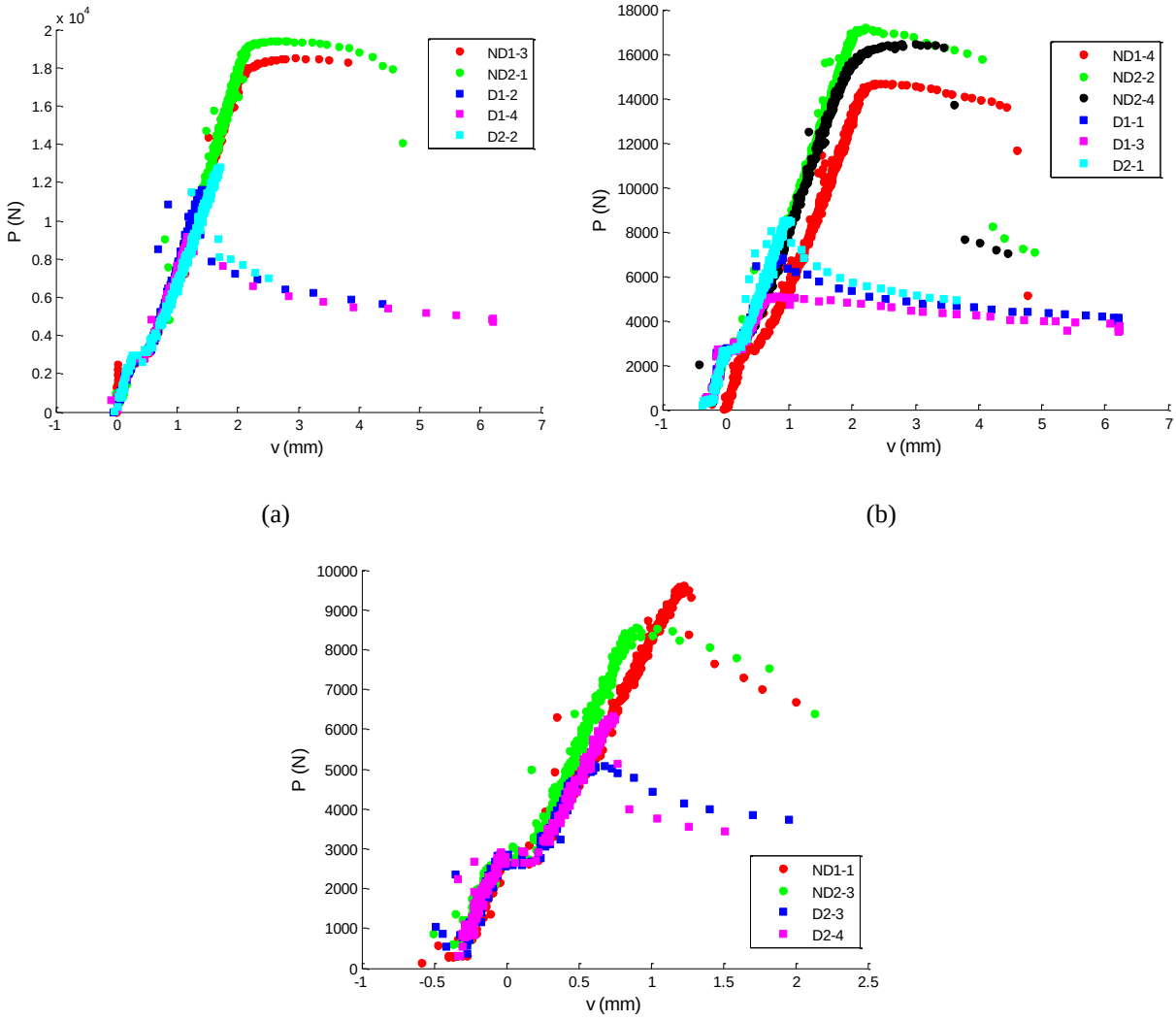

Fig. 75. Load-end shortening curves for test articles with a 6.35 mm core and a nominal length of 740 mm. (a) Room temperature, (b) low flux of 1.3 kW/m^2, (c) high flux of 2.5 kW/m^2.

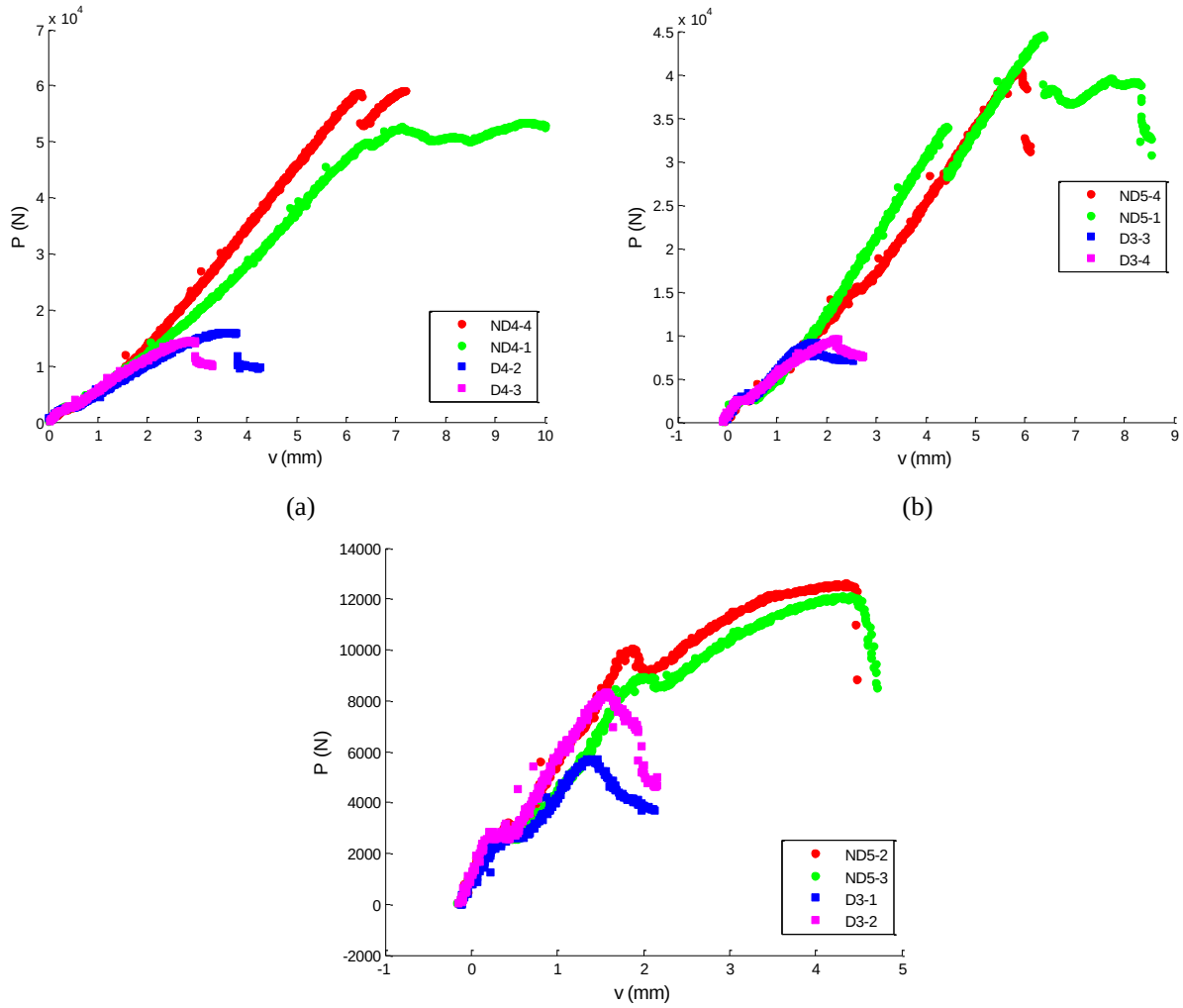

Fig. 76. Load-end shortening curves for test articles with a 12.7 mm core and a nominal length of 585 mm. (a) Room temperature, (b) low flux of 1.3 kW/m2, (c) high flux of 2.5 kW/m2.

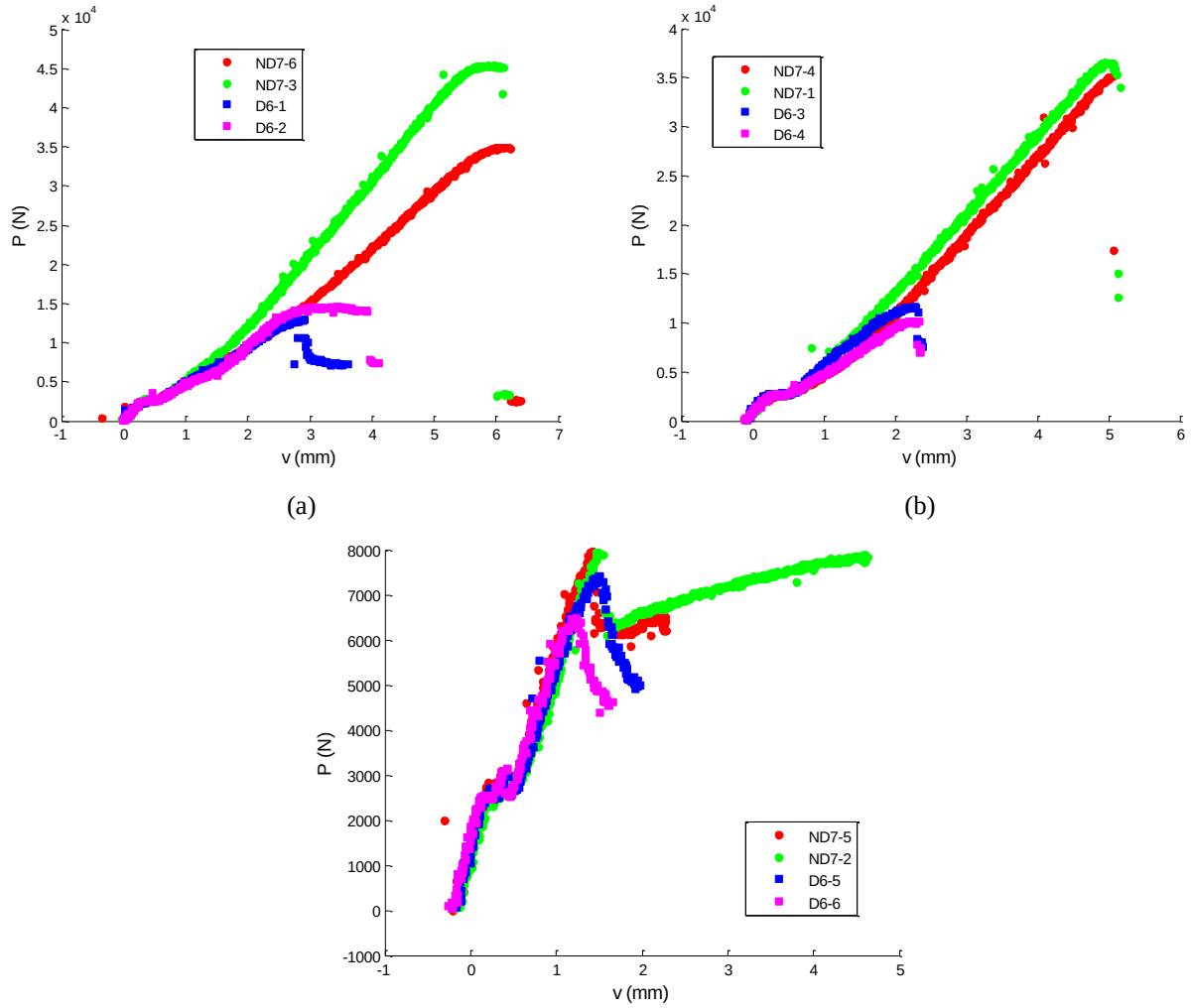

Fig. 77. Load-end shortening curves for test articles with a 12.7 mm core and a nominal length of 705 mm. (a) Room temperature, (b) low flux of 1.3 kW/m2, (c) high flux of 2.5 kW/m2.

Lastly, a direct comparison of how the debond affects the critical buckling load, P_{cr}, of a column under compressive loading when exposed to one-sided heating will be made. First, a consistent method must be used to quantify what the experimental buckling load is since the formation of the facesheet/core debond and other damage occurring throughout the test make this difficult. In this work, buckling is said to occur when there is a global failure of the test article resulting in both a rapid change of shape and out-of-plane displacements. This prevents artificially high values from being used due to the post-buckling behavior of test articles exposed to the high flux exposure where the load significantly increases after a global failure has occurred. Figure 78 shows the critical buckling load results from all tests taken for the various core thicknesses, h_c. Results have

been normalized using the Engesser buckling load in Equation (21) with a Huang and Kardomateas shear correction formula. A thorough derivation of each is given in Carlsson and Kardomateas [3] along with comparisons to other commonly used sandwich composite buckling formulas.

$$P_{cr} = \frac{P_E}{1 + \frac{\beta P_E}{AG_{eq}}} \tag{21}$$

Where P_E is the Euler buckling load for a fixed-fixed column and β / AG_{eq} is the shear correction factor used to take into account the additional deformation from the shear strains of the compliant core.

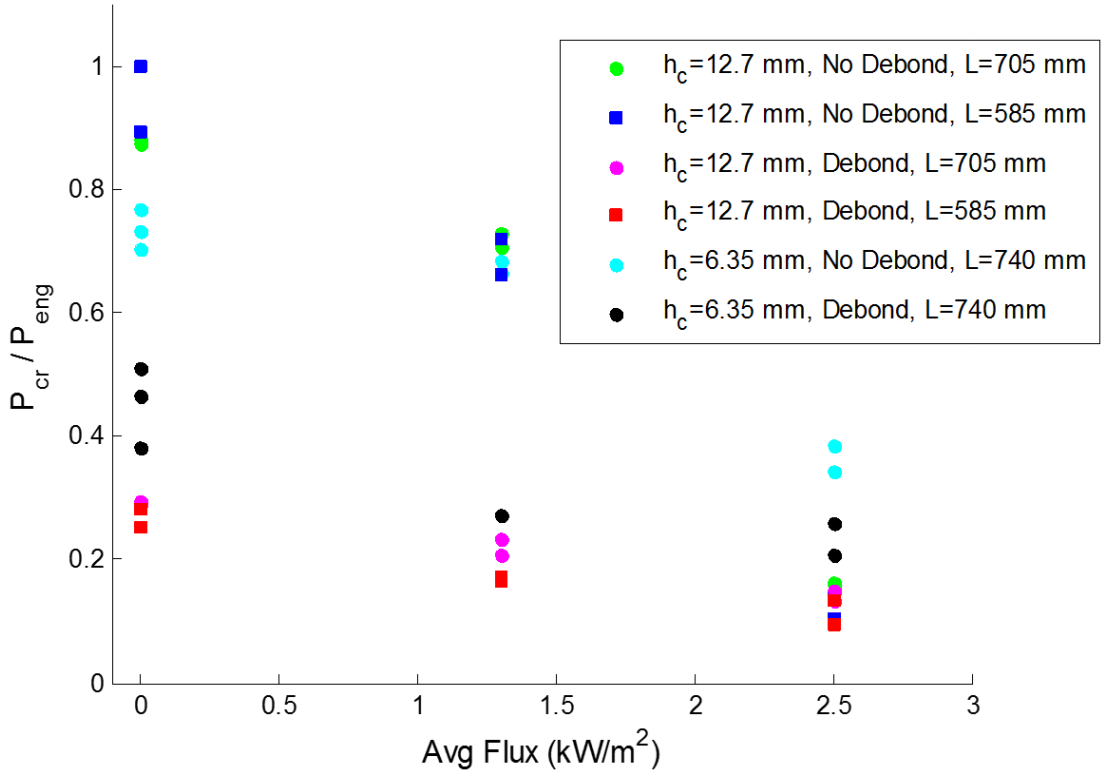

Fig. 78. Normalized critical buckling loads as a function of the one-sided average incident flux.

Chapter 5: Summary and Conclusions

5.1 Summary

Investigation of sandwich composite columns with facesheet/core debonds exposed to one-sided heating was undertaken to understand the failure processes and influence of the interfacial fracture toughness and core. Sandwich composites consisting of E-glass/epoxy facesheets with end-grain balsa wood cores were the only materials tested. These were chosen due to their current and increasing use in naval ships due to their exceptional fire resistance and mechanical properties. With this increasing use of these material types in scenarios where impact and fire could be expected, the buckling of columns under similar high-temperature compressive loading was undertaken.

Prior to large scale testing, Mode I and II fracture tests were used to elucidate the interfacial properties. A Double Cantilever Beam (DCB) test configuration was used in combination with an oven to observe how the Mode I 3D-DIC system was used to track crack-growth along with a FLIR SC655 thermographic camera to verify that set point temperatures were maintained. In addition to this, a Cracked Split Beam (CSB) test configuration was used to investigate the room temperature Mode II interfacial toughness. To ensure as high as a sought after mode-mixity as possible, the facesheet layup was chosen to match as closely as possible the bending stiffness of the upper and lower beams of the DCB/CSB specimen. By doing this the neutral axis of the composite beam is shifted to lie in parallel with the interfacial plane where crack-growth is occurring. Since the layup of the facesheet could only be chosen to minimize the difference of the two beam bending stiffnesses, not make them equal, along with the complicated bimaterial interface, mode-mixity was verified using the Virtual Crack Closure Technique (VCCT).

A custom intermediate-scale load frame was constructed for compressive testing of large scale test articles. In addition to the load frame, a sliding 3 x 2 heater panel assembly is used to provide the incident one-sided flux exposure of 1.3 kW/m^2 and 2.5 kW/m^2 to the sample surfaces. This radiative flux was characterized by recording the temperature profile on a thin sheet of steel painted so that the surface emissivity is known. Numerous test articles were manufactured using the

VARTM method along with two thicknesses of balsa core, 6.35 mm and 12.7 mm. Samples were manufactured both debond free and with a 88.9 mm wide debond located widthwise in the center of the sample. This debond was created using either two 0.3 mil sheets of a Kapton® HN film for the 6.35 mm core thickness samples, or two sheets of 1 mil skived PTFE film for all 12.7 mm debond test articles. Tests were performed in both load control (6.35 mm core) at 50 N/s and displacement control (12.7 mm core) at 1.25 mm/min so that the debond buckling and propagation could be observed in greater detail. Boundary conditions were fixed-fixed using 4" x 4" x 0.5" steel angles bolted together. Measurements were taken on the unexposed facesheet using a 3D-DIC system spatially combined with a FLIR SC655 thermographic camera. This allowed temperatures to be mapped to the displacement/strain data points measured by the DIC and tracked as the sample underwent excessive deformations. In addition to this, a single FLIR SC655 thermographic camera was used to observe the temperatures on the exposed facesheet.

5.2 Conclusions

Mode I room temperature DCB tests exhibited stable crack-growth without significant damage to the core. This allowed a value of 858 ± 134 J/m^2 to be calculated using the modified beam theory method and comparisons were made to similar works showing a reasonable Mode I interfacial fracture toughness value was obtained. As the test temperature was increased, so to was the amount of damage in the form of small segments of the core separating from the surrounding material, crack-kinking, and facesheet wrinkling that occurred. These increased the elastic strain energy of the system and thus, resulted in artificially high Mode I fracture toughness values. While realistic temperature dependent Mode I fracture toughness values were not obtained, additional insight was gained into the competing behavior of the interfacial fracture toughness and reduction of balsa core properties. This study showed that while a reduced fracture toughness could be expected as interface temperatures increase, the reduction of the balsa core strength has a more dominant effect in initiating failure prior to a crack-increment forming.

Mode II room temperature CSB tests did not exhibit stable crack-growth at any point of the test. Small segments of the balsa core separated from the surrounding core material early in the loading of the sample. While for the Mode I DCB test where this was not a problem as long as the damage was small, due to the sliding motion of the CSB test these small balsa segment slid into the core

material they were once joined to. As the sliding increased so too did the contact force between the separated balsa core and the surrounding material. This resulted in a very high, and continually increasing, Mode II fracture toughness. Again though, the susceptibility of the balsa core to damage once again prevented stable crack-growth from occurring.

Large scale testing showed a similar mode of failure for the debond samples as could be expected after performing the Mode I and II fracture tests. At room temperature, debond buckling and propagation could be observed until a core failure occurred at one of the two crack-fronts of the debond. This core failure triggers a rapid global failure to occur where a drop in the load capacity and an increase in the out-of-plane displacement occur. As the sample temperature is increased due to the one-sided exposure, the amount of debond buckling and propagation decreases as well with core damage still occurring at the crack-front and leading to a global failure. At the highest flux level of 2.5 kW/m^2 debond buckling and propagation were almost nonexistent, only occurring in one of four samples and to a very small degree before the balsa core failed. This debond buckling and propagation was only observed to occur for samples whose core thickness was 12.7 mm. All test articles using the thinner 6.35 mm core failed in an anti-symmetric post-buckling shape with the debond remaining partially bonded until the excessive post-buckling deformations separated the facesheet from the core. This could be explained by the Kapton® allowing a slight amount of adhesion of the epoxy, thus creating a weakened interface but not a true debond. A second explanation is that a small misalignment existed in either the loading or boundary conditions and failed the sample prior to the debond buckling being allowed to occur.

All no debond test articles exposed to either no incident or a 1.3 kW/m^2 flux level exhibited the typical out-of-plane deformation shape expected from a fixed-fixed column. What varied was as the out-of-plane displacement increased, a sudden failure of the core occurred near the gripped region where the sample tried to maintain the zero-slope boundary condition. This core failure again triggered a sudden global failure of the column which resulted in a loss of load carrying capacity and large out-of-plane displacements. For the high flux (2.5 kW/m^2) exposed test articles, failure appeared to be triggered by an exposed facesheet wrinkling deformation. This wrinkling

caused a pivot point to form allowing the entire sample to kink at this location and a global failure to occur. This differed from the low flux and room temperature tests though in that as the sample continued to displace outwards, the load carrying capacity continued to increase. Overall the influence on the reduced strength and mechanical properties of the balsa wood core are the dominant factor in buckling of samples containing a debond by arresting crack-growth and triggering a sudden global failure.

5.3 Recommendations

Recommendations for the fracture testing and large scale testing will be listed separately but one is common to both. Due to the inhomogeneous nature of the balsa wood core material, where properties can change within a segment and between the segments that make up a whole panel, it is recommended to select an alternate high density/stiffness core material. By doing so, the variability in mechanical and thermal properties can be eliminated.

5.3.1 Fracture Recommendations

- Attach a stiffening plate to the upper and lower facesheets to prevent excessive rotations at high temperatures.
- The optical DIC system was not needed for crack-growth measurement, simpler methods would limit test setup time.
- While Mode I DCB sample dimensions are constrained to allow the sample to fit within the oven, no such constraint exists for the Mode II CSB specimens. Increase the length of Mode II sample and start with a greater initial crack length to lessen to Mode I component.

5.3.2 Large Scale Test Recommendations

- Use a thicker core that will still allow intermediate-scale load frame to buckle column.
- PTFE film appeared to create a better initial debond than the Kapton® film.
- Adjust heater panels to permit a more uniform heating of the exposed surface. .

References

[1] Vinson, J.R., *The Behavior of Sandwich Structures of Isotropic and Composite Materials.pdf*. Technomic Publishing Company, 1999, p. 363.

[2] LeGault, M., "DDG-1000 Zumwalt: stealth warship," *Compos. Technol.*, 2010.

[3] Carlsson, L.A., Kardomateas, G.A., *Structural and Failure Mechanics of Sandwich Composites*. Springer, 2011.

[4] Shivakumar, K.N., Smith, S.A., "In Situ Fracture Toughness Testing of Core Materials in Sandwich Panels," *J. Compos. Mater.*, vol. 38, no. 8, pp. 655–668, Apr. 2004.

[5] Shivakumar, K.N., "An Evaluation of Data Reduction Methods for Opening Mode Fracture Toughness of Sandwich Panels," *J. Sandw. Struct. Mater.*, vol. 7, no. 1, pp. 77–90, Jan. 2005.

[6] Girolamo, D., Davila, C., Leone, F., Lin, S., "Adhesive Characterization and Progressive Damage Analysis of Bonded Composite Joints," in *Pegasus-AIAA Student Conference*, 2014, pp. 1–11.

[7] Ramantani, D.A., de Moura, M.F.S.F., Campilho, R.D.S.G., Marques, A.T., "Fracture Characterization of Sandwich Structures Interfaces Under Mode I Loading," *Compos. Sci. Technol.*, vol. 70, no. 9, pp. 1386–1394, Sep. 2010.

[8] Davidson, P., Waas, A.M., Yerramalli, C.S., "Experimental Determination of Validated, Critical Interfacial Modes I and II Energy Release Rates in a Composite Sandwich Panel," *Compos. Struct.*, vol. 94, no. 2, pp. 477–483, Jan. 2012.

[9] Liechti, K.M., Marton, B., "Delamination of a High-Temperature Sandwich Plate," *Exp. Mech.*, vol. 42, no. 2, pp. 206–213, Jun. 2002.

[10] Cantwell, W.J., Davies, P., "A Test Technique for Assessing Core-Skin Adhesion in Composite Sandwich Structures," *J. Mater. Sci. Lett.*, vol. 13, pp. 203–205, 1994.

[11] Cantwell, W.J., Davies, P., "A Study of Skin-Core Adhesion in Glass Fibre Reinforced Sandwich Materials," *Appl. Compos. Mater.*, pp. 407–420, 1996.

[12] Adams, D., Kessler, J., "Development and Evaluation of Fracture Mechanics Test Methods For Sandwich Composites," 2010.

[13] Weaver, C.A., "Evaluation of Mode I Fracture Mechanics Test Methods for Sandwich Composites," M.S. thesis, University of Utah, 2010.

[14] Li, X., Carlsson, L.A., "The Tilted Sandwich Debond (TSD) Specimen for Face/Core Interface Fracture Characterization," *J. Sandw. Struct. Mater.*, vol. 1, no. 1, pp. 60–75, Jan. 1999.

[15] Viana, G.M., Carlsson, L.A., "Influences of Foam Density and Core Thickness on Debond Toughness of Sandwich Specimens with PVC Foam Core," *J. Sandw. Struct. Mater.*, vol. 5, no. 2, pp. 103–118, Apr. 2003.

[16] Lundsgaard-Larsen, C., Sørensen, B.F., Berggreen, C., Østergaard, R.C., "A Modified DCB Sandwich Specimen for Measuring Mixed-Mode Cohesive Laws," *Eng. Fract. Mech.*, vol. 75, no. 8, pp. 2514–2530, May 2008.

[17] Cantwell, W.J., Scudamore, R., Ratcliffe, J., Davies, P., "Interfacial Fracture in Sandwich Laminates," *Compos. Sci.*, vol. 59, pp. 2079–2085, 1999.

[18] Quispitupa, A., Berggreen, C., Carlsson, L.A., "On the Analysis of a Mixed Mode Bending Sandwich Specimen for Debond Fracture Characterization," *Eng. Fract. Mech.*, vol. 76, no. 4, pp. 594–613, 2009.

[19] Carlsson, L.A., "On the Design of the Cracked Sandwich Beam (CSB) Specimen," *J. Reinf. Plast. Compos.*, 1991.

[20] Shipsha, A., Burman, M., Zenkert, D., "Interfacial Fatigue Crack Growth in Foam Core Sandwich Structures," *Fatigue Fract.*, no. September 1998, pp. 123–131, 1999.

[21] Avery, J.L., Sankar, B.V., "Compressive Failure of Sandwich Beams with Debonded Face-Sheets," *J. Compos. Mater.*, vol. 34, no. 14, pp. 1176–1199, Jul. 2000.

[22] Kardomateas, G.A., La Saponara, V., "Tests on the Compression Behavior of Debonds in Sandwich Beams" in *ASME International Conference*, 2001.

[23] Vadakke, V., Carlsson, L.A., "Experimental Investigation of Compression Failure of Sandwich Specimens with Face/Core Debond," *Compos. Part B Eng.*, vol. 35, no. 6–8, pp. 583–590, Sep. 2004.

[24] Mouritz, A.P., Gardiner, C., "Compression Properties of Fire-Damaged Polymer Sandwich Composites," *Compos. Part A Appl. Sci.*, vol. 33, 2002.

[25] Feih, S., Mathys, Z., Gibson, A.G., Mouritz, A.P., "Modeling Compressive Skin Failure of Sandwich Composites in Fire," *J. Sandw. Struct. Mater.*, vol. 10, no. 3, pp. 217–245, May 2008.

[26] Asaro, R.J., Lattimer, B.Y., Ramroth, W., "Structural Response of FRP Composites during Fire," *Composite Structures*, Vol. 87, Issue 4, pp. 382-393, 2008.

[27] Lattimer, B.Y., Asaro, R.J., Ouellette, J., and Mealy, C., "Structural Response of Fiber Reinforced Plastic Composites during Fires," *Proceedings of Interflam 2007*, London, England, pp. 653-664, 2007.

[28] Omega QC and QH Series Datasheet.

[29] Rippe, C., Lattimer, B.Y., "Full-Field Surface Heat Flux Measurement Using Non-Intrusive Infrared Thermography," *Fire Saf. J (submitted).*

[30] Boyd, S.E., "Compression Creep Rupture of an E-glass / Vinyl Ester Composite Subjected to Combined Mechanical and Fire Loading Conditions," Ph.D dissertation, Virginia Polytechnic Institute and State University, 2006.

[31] Gibson, A.G., Wu, Y.S., Evans, J.T., Mouritz, A.P., "Laminate Theory Analysis of Composites under Load in Fire," *J. Compos. Mater.*, vol. 40, no. 7, pp. 639–658, Jul. 2005.

[32] Feih, S., Mathys, Z., Gibson, A.G., Mouritz, A.P., "Modelling the Compression Strength of Polymer Laminates in Fire," *Compos. Part A Appl.*, 2007.

[33] Feih, S., Mathys, Z., Gibson, A.G., Mouritz, A.P., "Modelling the Tension and Compression Strengths of Polymer Laminates in Fire," *Compos. Sci. Technol.*, vol. 67, no. 3–4, pp. 551–564, Mar. 2007.

[34] Hopkins, D., Chamis, C., "A Unique Set of Micromechanics Equations for High-Temperature Metal Matrix Composites," *ASTM STP*, 1988.

[35] Case, S.W., *Class Notes.*, Biomedical and Engineering Mechanics (BEAM), Virginia Polytechnic Institute and State University Blacksburg, VA.

[36] Pagano, N.J., Tandon, G.P., "Elastic Response of Multi-Directional Coated-Fiber Composites," *Compos. Sci. Technol.*, vol. 31, no. 4, pp. 273–293, Jan. 1988.

[37] Smith, S.A., Emmanwori, L.L., Sadler, R.L., Shivakumar, K.N., "Evaluation of Composite Sandwich Panels Fabricated Using Vacuum Assisted Resin Transfer Molding" in *45th International SAMPE Symposium*.

[38] Lattimer, B.Y., Ouellette, J., "Properties of Composite Materials for Thermal Analysis Involving Fires," *Compos. Part A Appl. Sci. Manuf.*, vol. 37, no. 7, pp. 1068–1081, Jul. 2006.

[39] BALTEK, SB Datasheet 10.2014.

[40] Tagarielli, V.L., Deshpande, V.S., Fleck, N.A., Chen, C., "A Constitutive Model for Transversely Isotropic Foams, and its Application to the Indentation of Balsa Wood," *Int. J. Mech. Sci.*, vol. 47, no. 4–5, pp. 666–686, Apr. 2005.

[41] Goodrich, T., Nawaz, N., Feih, S., Lattimer, B.Y., Mouritz, A.P., "High-Temperature Mechanical Properties and Thermal Recovery of Balsa Wood," *J. Wood Sci.*, vol. 56, no. 6, pp. 437–443, Jun. 2010.

[42] Feih, S., Mathys, Z., Gibson, A.G., Mouritz, A.P., "Modeling Compressive Skin Failure of Sandwich Composites in Fire," *J. Sandw. Struct. Mater.*, vol. 10, no. 3, pp. 217–245, May 2008.

[43] Wang, J., Qiao, P., "Fracture Analysis of Shear Deformable Bi-Material Interface," *J. Eng. Mech.*, no. March, pp. 306–316, 2006.

[44] Liu, S., Mei, Yuhai., Wu, T.Y., "Bimaterial Interfacial Crack Growth as a Function of Mode-Mixity," *IEEE Trans. Components, Packag. Manuf. Technol. Part A*, vol. 18, no. 3, pp. 618–626, 1995.

[45] ASTM D5528-94a: Standard Test Method for Mode I Interlaminar Fracture Toughness of Unidirectional Fiber-Reinforced Polymer Matrix Composites.

[46] Kanninen, M., Popelar, C., *Advanced fracture mechanics*. Oxford University Press, 1985.

[47] Cholewa, N.M., Summers, P.T., Feih, S., Lattimer, B.Y., Case, S.W., "A Technique for Coupled Thermo-Mechanical Response Measurement using 3-D Infrared Thermography Digital Image Correlation (TDIC)," *Exp. Mech.*(submitted), 2014.

[48] Chu, T.C., Ranson, W.F., Sutton, M.A., Peters, W.H., "Applications of Digital Image Correlation Techniques to Experimental Mechanics," *Exp. Mech*. Sep. 1985.

[49] Bruck, H.A., Mcneill, S.R., Sutton, M.A., Iii, W.H.P., "Digital Image Correlation Using Newton-Raphson Method of Partial Differential Correction," *Exp. Mech*., 1989.

[50] Sutton, M.A., Yan, J.H., Tiwari, V., Schreier, H.W., Orteu, J.J., "The Effect of Out-of-Plane Motion on 2D and 3D Digital Image Correlation Measurements," *Opt. Lasers Eng.*, vol. 46, no. 10, pp. 746–757, Oct. 2008.

[51] Luo, P.F., Chao, Y.J., Sutton, M.A., Peters, W.H., "Accurate Measurement of Three-Dimensional Deformations in Deformable and Rigid Bodies Using Computer Vision," *Exp. Mech.*, vol. 33, no. 2, pp. 123–132, Jun. 1993.

[52] Krueger, R., "The Virtual Crack Closure Technique : History , Approach and Applications," 2002.

[53] Agrawal, A., Karlsson, A.M., "Obtaining Mode Mixity for a Bimaterial Interface Crack Using the Virtual Crack Closure Technique," *Int. J. Fract.*, vol. 141, no. 1–2, pp. 75–98, Sep. 2006.

Appendix

Appendix A: Fracture Test Article Geometry

Table A1: Double Cantilever Beam (DCB) Test Article Geometry

Sample ID	Test	Temp (°C)	$a_0^{(1)}$ (mm)	t(2) / STD (mm)	b(2) / STD (mm)	L (mm)
DCB1-1	Mode I	25	9.2	13.4 / 0.14	23.9 / 0.56	209.5
DCB1-3			5.5	13.5 / 0.23	24.5 / 0.10	209.5
DCB2-7			17.5	13.7 / 0.12	26.7 / 0.34	210.0
DCB1-5			19.3	13.4 / 0.17	25.9 / 0.36	208.0
DCB1-6			17.5	13.4 / 0.17	23.2 / 0.34	209.5
DCB2-9			6.9	13.7 / 0.07	26.7 / 0.59	210.0
DCB2-15			21.2	13.7 / 0.13	25.9 / 0.17	211.0
DCB2-17		60	17.8	13.9 / 0.10	26.4 / 0.44	207.0
DCB2-24		80	27.7	14.0 / 0.11	26.4 / 0.26	208.0
DCB2-26		100	29.8	13.8 / 0.14	26.9 / 0.20	208.0
CSB1-1	Mode II	25	29.2	13.4 / 0.08	35.6 / 4.10	210
CSB1-2		25	33.1	13.7 / 0.11	35.6 / 0.20	208

(1) Initial crack length
(2) Average dimension shown from five measurements taken along length of sample

Appendix B: Beam Buckling Test Article Geometry

Table B1: Beam Buckling Test Article Geometry

Core Thickness (mm)	Sample ID	Debond[1] (Y/N)	Incident Flux[2] (kW/m^2)	t[3] / STD (mm)	b[3] / STD (mm)	L (mm)	P_{cr}[4] (kN)
6.35	ND1-2	No	0	9.8 / 0.13	106.5 / 1.23	737	26.35
	ND1-3			9.8 / 0.14	112.3 / 0.91	738	26.26
	ND2-1			10.0 / 0.16	107.8 / 0.60	738	25.21
	D1-2	Yes (Kapton®)		9.8 / 0.26	107.3 / 1.38	740	24.92
	D1-4			9.8 / 0.17	103.8 / 0.35	741	24.05
	D2-2			9.8 / 0.17	106.8 / 2.26	736	25.10
12.7	ND4-1	No		16.1 / 0.18	91.7 / 0.62	584	58.45
	ND4-4			15.9 / 0.12	91.7 / 0.55	583	58.64
	ND7-3			15.8 / 0.17	99.1 / 0.48	708	49.59
	ND7-6			16.1 / 0.12	79.5 / 0.64	709	39.68
	D4-2	Yes (PTFE)		15.8 / 0.11	89.0 / 0.57	587	56.42
	D4-3			16.0 / 0.14	89.5 / 0.41	586	56.87
	D6-1			16.0 / 0.22	87.7 / 0.35	705	44.21
	D6-2			16.1 / 0.12	98.6 / 0.44	705	49.71
6.35	ND1-4	No	1.3	9.8 / 0.13	94.1 / 1.61	736	22.12
	ND2-2			9.8 / 0.18	107.3 / 0.35	738	25.16
	ND2-4			10.2 / 0.09	105.4 / 0.71	737	24.71
	D1-1	Yes (Kapton®)		9.8 / 0.26	107.5 / 1.55	740	25.03
	D1-3			9.8 / 0.16	104.6 / 0.34	741	24.23
	D2-1			9.8 / 0.19	108.8 / 2.04	737	25.57
12.7	ND7-1	No		15.8 / 0.05	99.2 / 0.48	705	50.00
	ND7-4			15.8 / 0.06	98.3 / 1.34	703	49.73
	ND5-1			16.0 / 0.08	95.9 / 0.48	586	60.96
	ND5-4			15.9 / 0.12	96.3 / 0.23	587	61.00
	D3-3	Yes (PTFE)		16.2 / 0.17	87.1 / 0.56	584	55.48

Table B1 cont: Beam Buckling Test Article Geometry

Core Thickness (mm)	Sample ID	Debond[1] (Y/N)	Incident Flux[2] (kW/m^2)	t[3] / STD (mm)	b[3] / STD (mm)	L (mm)	P_{cr}[4] (kN)
12.7	D3-4	Yes (PTFE)	1.3	16.2 / 0.13	87.6 / 0.41	584	55.84
	D6-3			16.2 / 0.32	98.8 / 0.25	706	49.64
	D6-4			16.1 / 0.35	98.5 / 0.22	711	49.02
6.35	ND1-1	No	2.5	10.2 / 0.33	106.6 / 1.23	736	25.09
	ND2-3			9.9 / 0.16	106.3 / 2.43	738	24.84
	D2-3	Yes (Kapton®)		9.8 / 0.15	104.5 / 1.74	735	24.68
	D2-4			9.7 / 0.12	102.7 / 1.82	733	24.38
12.7	ND5-2	No		16.1 / 0.23	95.9 / 0.22	589	60.60
	ND5-3			15.9 / 0.12	95.8 / 0.25	590	60.36
	ND7-2			15.9 / 0.14	99.2 / 0.39	713	49.19
	ND7-5			16.2 / 0.09	98.9 / 0.28	701	50.18
	D3-1	Yes (PTFE)		15.9 / 0.21	92.9 / 2.63	577	59.94
	D3-2			16.1 / 0.16	95.7 / 0.21	582	61.19
	D6-5			16.3 / 0.24	98.5 / 0.41	706	49.51
	D6-6			16.3 / 0.12	97.5 / 1.21	705	49.15

(1) Debond width of 88.9 mm located in center of test article. Kapton® film thickness of 0.3 mil, PTFE thickness of 1 mil.
(2) Average heat flux on exposed surface.
(3) Average dimension shown from five measurements taken along length of sample.
(4) Engesser critical buckling load formula using a Huang and Kardomateas shear correction formula.

Appendix C: Exposed/Unexposed Facesheet Temperatures (Low Flux-1.3 kW/m^2)

Exposed Facesheet Temperatures

ND1-4	ND2-2	ND2-4	D1-1	D1-3
No Debond	No Debond	No Debond	Debond	Debond
$h_c = 6.35\ mm$	$h_c = 6.35\ mm$	$h_c = 6.35\ mm$	$h_c = 6.35\ mm$	$h_c = 6.35\ mm$
L = 736 mm	L = 738 mm	L = 737 mm	L = 740 mm	L = 741 mm

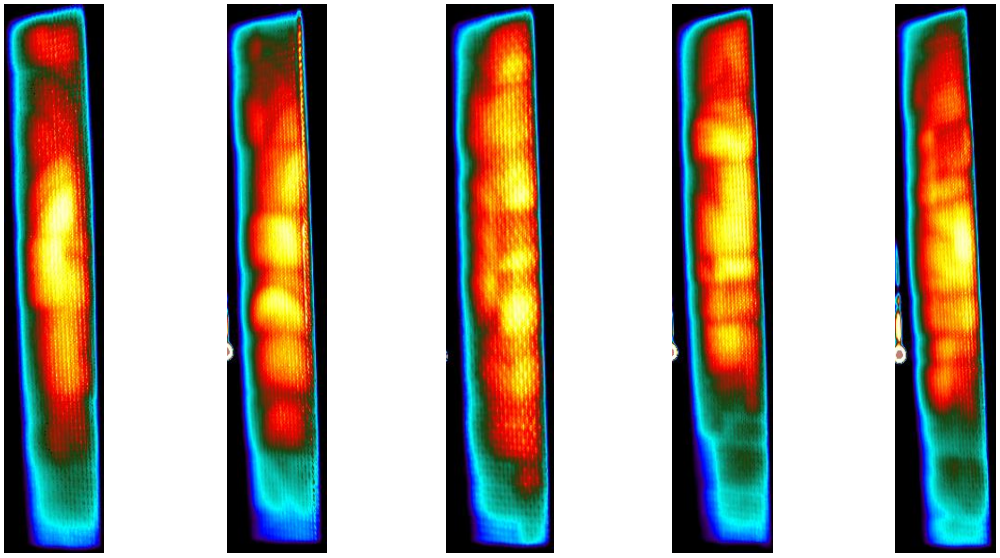

D2-1	ND7-1	ND7-4	ND5-1	ND5-4
Debond	No Debond	No Debond	No Debond	No Debond
$h_c = 6.35\ mm$	$h_c = 12.7\ mm$	$h_c = 12.7\ mm$	$h_c = 12.7\ mm$	$h_c = 12.7\ mm$
L = 737 mm	L = 705 mm	L = 703 mm	L = 586 mm	L = 587 mm

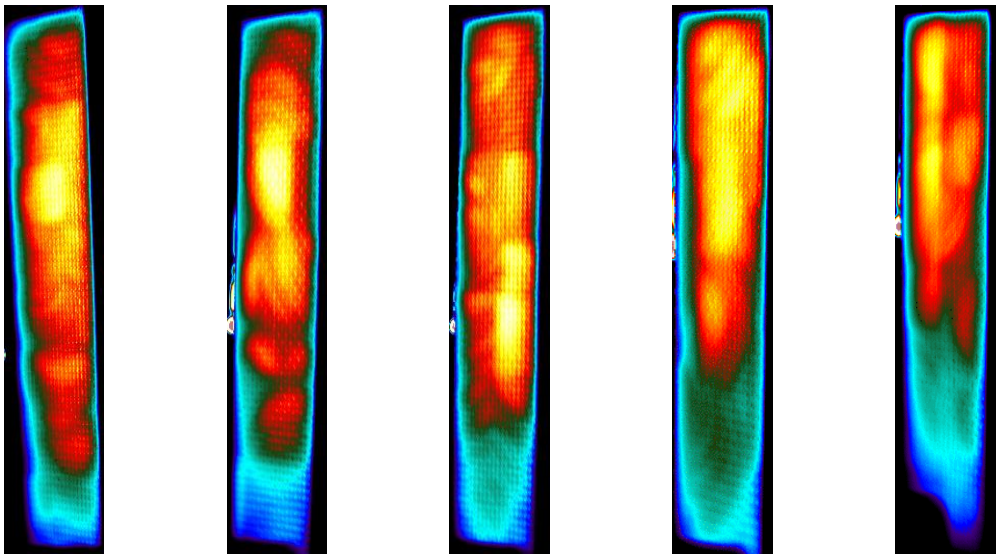

D3-3
Debond
$h_c = 12.7\ mm$
L = 584 mm

D3-4
Debond
$h_c = 12.7\ mm$
L = 584 mm

D6-3
Debond
$h_c = 12.7\ mm$
L = 706 mm

D6-4
Debond
$h_c = 12.7\ mm$
L = 711 mm

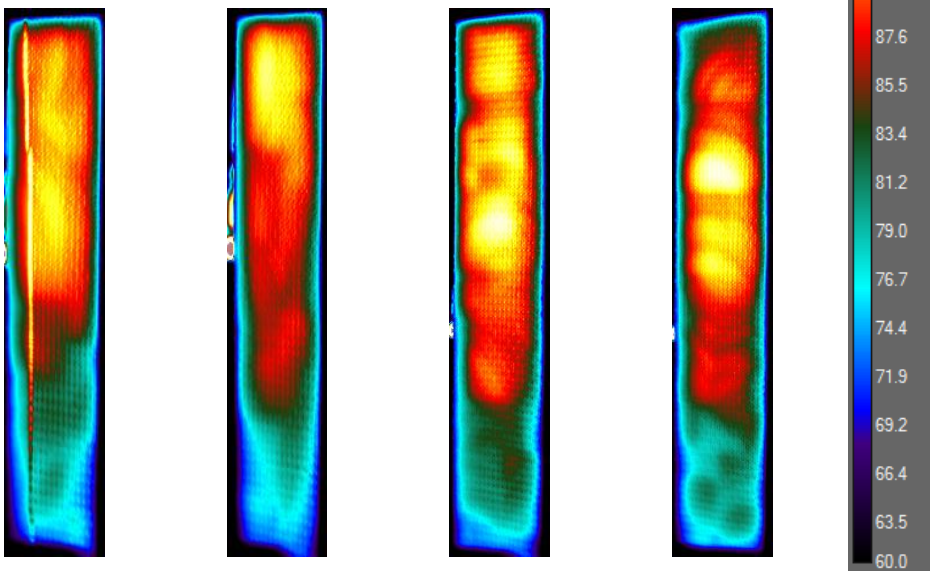

Unexposed Facesheet Temperatures

ND1-4
No Debond
$h_c = 6.35\ mm$
L = 736 mm

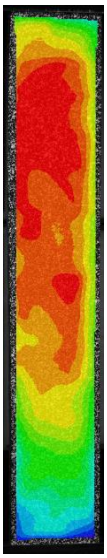

ND2-2
No Debond
$h_c = 6.35\ mm$
L = 738 mm

ND2-4
No Debond
$h_c = 6.35\ mm$
L = 737 mm

D1-1
Debond
$h_c = 6.35\ mm$
L = 740 mm

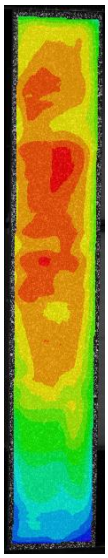

D1-3
Debond
$h_c = 6.35\ mm$
L = 741 mm

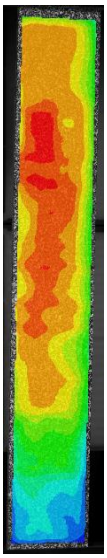

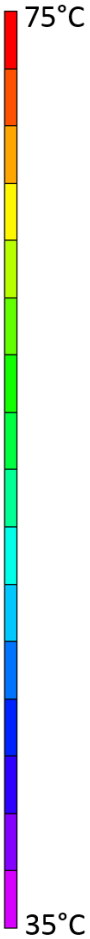

D2-1
Debond
$h_c = 6.35\ mm$
L = 737 mm

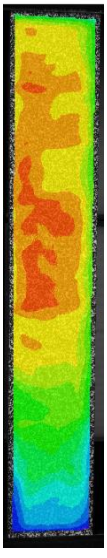

ND7-1
No Debond
$h_c = 12.7\ mm$
L = 705 mm

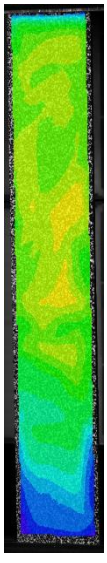

ND7-4
No Debond
$h_c = 12.7\ mm$
L = 703 mm

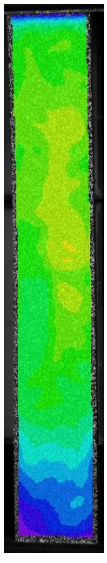

ND5-1
No Debond
$h_c = 12.7\ mm$
L = 586 mm

ND5-4
No Debond
$h_c = 12.7\ mm$
L = 587 mm

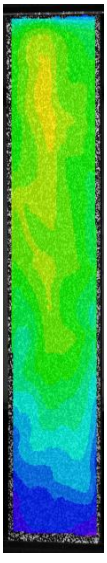

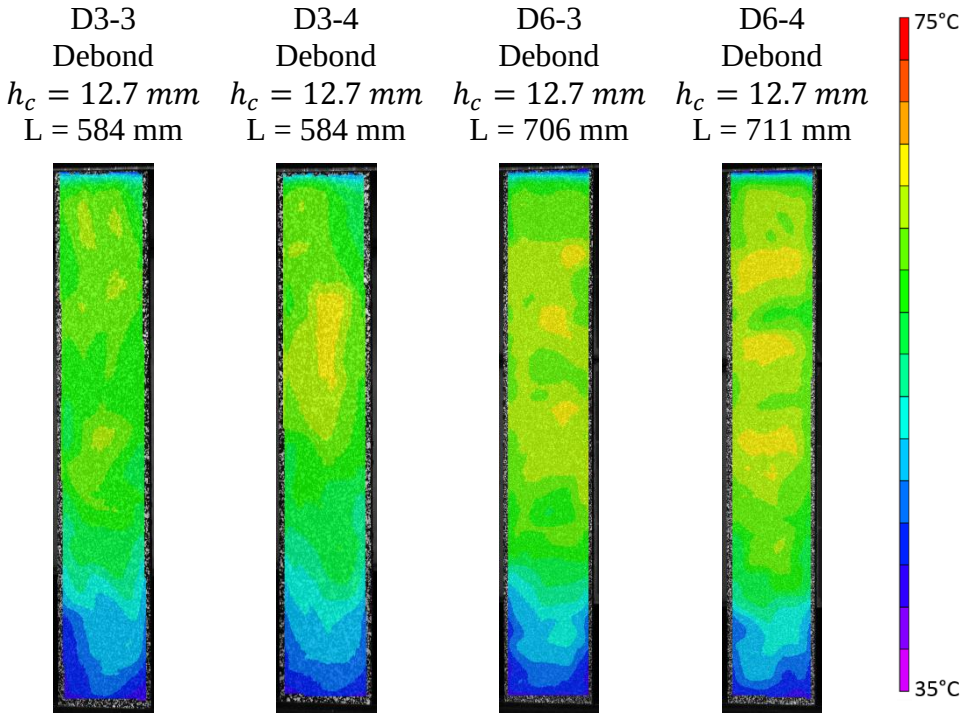
D3-3
Debond
$h_c = 12.7\ mm$
L = 584 mm
D3-4
Debond
$h_c = 12.7\ mm$
L = 584 mm
D6-3
Debond
$h_c = 12.7\ mm$
L = 706 mm
D6-4
Debond
$h_c = 12.7\ mm$
L = 711 mm
75°C
35°C

Appendix D: Exposed/Unexposed Facesheet Temperatures (High Flux-2.5 kW/m^2)

Exposed Facesheet Temperatures

ND2-3
No Debond
$h_c = 6.35\ mm$
L = 738 mm

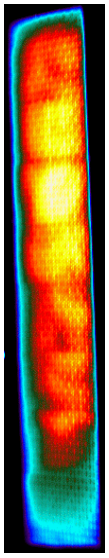

D2-3
Debond
$h_c = 6.35\ mm$
L = 735 mm

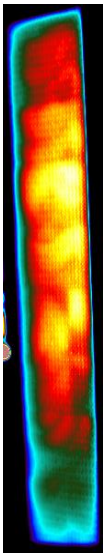

D2-4
Debond
$h_c = 6.35\ mm$
L = 733 mm

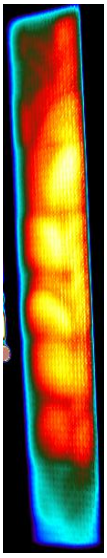

ND5-2
No Debond
$h_c = 12.7\ mm$
L = 589 mm

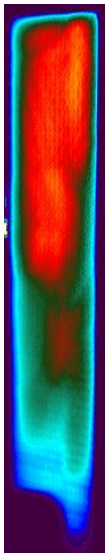

ND5-3
No Debond
$h_c = 12.7\ mm$
L = 590 mm

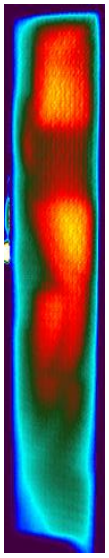

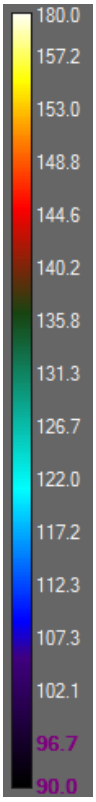

ND7-2
No Debond
$h_c = 12.7\ mm$
L = 713 mm

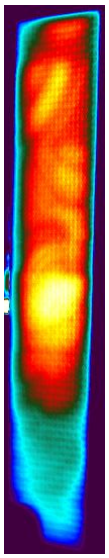

ND7-5
No Debond
$h_c = 12.7\ mm$
L = 701 mm

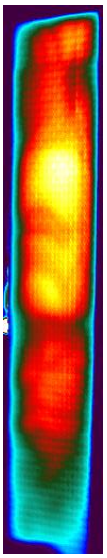

D3-1
Debond
$h_c = 12.7\ mm$
L = 577 mm

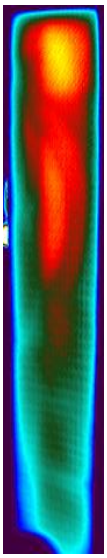

D3-2
Debond
$h_c = 12.7\ mm$
L = 582 mm

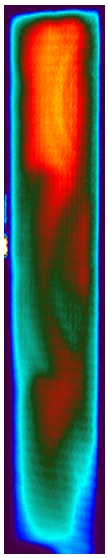

D6-5
Debond
$h_c = 12.7\ mm$
L = 582 mm

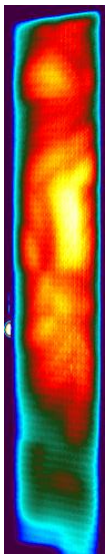

D6-6
Debond
$h_c = 12.7\ mm$
L = 705 mm

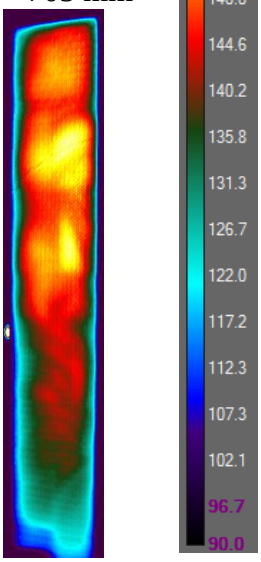

Unexposed Facesheet Temperatures

ND2-3
No Debond
$h_c = 6.35\ mm$
L = 738 mm

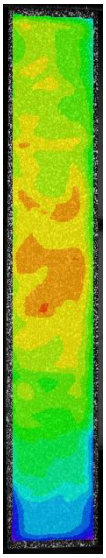

D2-3
Debond
$h_c = 6.35\ mm$
L = 735 mm

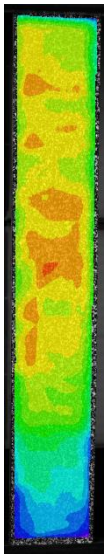

D2-4
Debond
$h_c = 6.35\ mm$
L = 733 mm

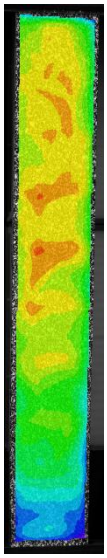

ND5-2
No Debond
$h_c = 12.7\ mm$
L = 589 mm

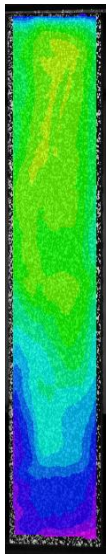

ND5-3
No Debond
$h_c = 12.7\ mm$
L = 590 mm

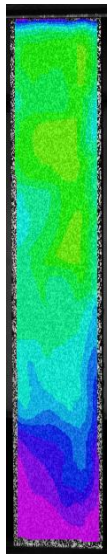

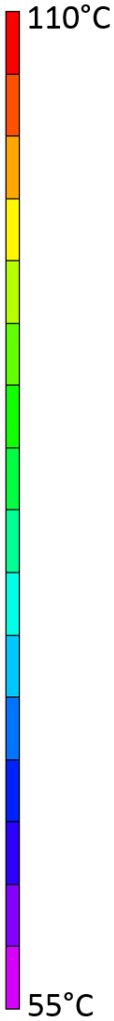

ND7-2
No Debond
$h_c = 12.7\ mm$
L = 713 mm

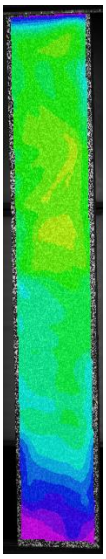

ND7-5
No Debond
$h_c = 12.7\ mm$
L = 701 mm

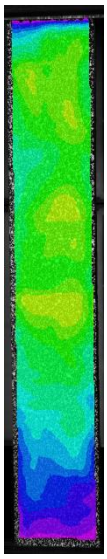

D3-1
Debond
$h_c = 12.7\ mm$
L = 577 mm

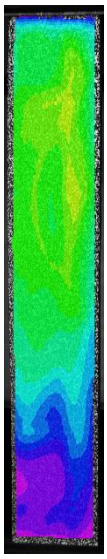

D3-2
Debond
$h_c = 12.7\ mm$
L = 582 mm

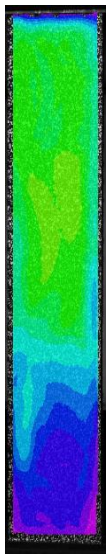

D6-5
Debond
$h_c = 12.7\ mm$
L = 582 mm

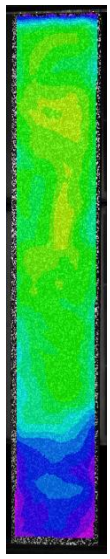

D6-6
Debond
$h_c = 12.7\ mm$
L = 705 mm